Downloaded from orbit.dtu.dk on: Dec 20, 2017

Technical University of Denmark

Fundamental properties of devices for quantum information technology

Nielsen, Per Kær; Mørk, Jesper; Lodahl, Peter; Nielsen, Torben Roland; Jauho, Antti-Pekka

Publication date:
2012

Document Version
Publisher's PDF, also known as Version of record

Link back to DTU Orbit

Citation (APA):
Nielsen, P. K., Mørk, J., Lodahl, P., Nielsen, T. R., & Jauho, A-P. (2012). Fundamental properties of devices for quantum information technology. Kgs. Lyngby: Technical University of Denmark (DTU).

DTU Library
Technical Information Center of Denmark

General rights
Copyright and moral rights for the publications made accessible in the public portal are retained by the authors and/or other copyright owners and it is a condition of accessing publications that users recognise and abide by the legal requirements associated with these rights.

- Users may download and print one copy of any publication from the public portal for the purpose of private study or research.
- You may not further distribute the material or use it for any profit-making activity or commercial gain
- You may freely distribute the URL identifying the publication in the public portal

If you believe that this document breaches copyright please contact us providing details, and we will remove access to the work immediately and investigate your claim.

Fundamental properties of devices for quantum information technology

A dissertation
submitted to the Department of Photonics Engineering
at the Technical University of Denmark
in partial fulfillment of the requirements
for the degree of
philosophiae doctor

Per Kær Nielsen
April 27, 2012

DTU Fotonik
Department of Photonics Engineering
Technical University of Denmark

Fundamental properties of devices for quantum information technology

Abstract

This thesis reports a theoretical investigation of the influence of the electron-phonon interaction on semiconductor cavity quantum electrodynamical systems, specifically a quantum dot coupled to an optical microcavity.

We develop a theoretical description of the decay dynamics of the quantum dot interacting with the cavity and the phonons. It is shown that the presence of the phonon interaction, fundamentally changes the spontaneous emission decay behavior of the quantum dot. Especially in the regime where the quantum dot-cavity spectral detuning is significantly larger than any linewidth of the system, the effect of the phonon interaction is very pronounced. A simple approximate analytical expression for the quantum dot decay rate is derived, which predicts a strong asymmetry with respect to the quantum dot-cavity detuning at low temperatures, and allows for a clear interpretation of the physics.

Furthermore, a study of the indistinguishability of single photons emitted from the coupled quantum dot-cavity system is performed, with special emphasis on non-Markovian decoherence due to the phonon interaction. We show that common theoretical approaches fail to predict the degree of indistinguishability, on both a qualitative and quantitative level, for experimentally relevant parameters regimes. The important role of non-Markovian effects in the short-time regime, where virtual processes dominate the decoherence of the quantum dot-cavity system, is emphasized. Importantly, our investigations lead to a maximum achievable degree of indistinguishability, a prediction which eludes common approaches.

Resumé

Denne afhandling rapporterer en teoretisk undersøgelse af indflydelsen af elektron-fonon vekselvirkningen på halvleder kavitet kvanteelektrodynamiske systemer, specifikt en kvanteprik koblet til en optisk mikrokavitet.

Vi udvikler en teoretisk beskrivelse af henfaldsdynamikken af kvanteprikken der vekselvirker med kaviteten og med fononerne. Det bliver vist at tilstedeværelsen af fononvekselvirkningen, fundamentalt ændrer opførslen af spontan henfald af kvanteprikken. Specielt i regimet hvor kvanteprik og kavitet er ude af resonans, med en værdi væsentligt større end nogen linjebredde i systemet, er effekten af fononvekselvirkningen meget udtalt. Et simpelt approksimativt analytisk udtryk for kvanteprikkens henfaldsrate bliver udledt, som ved lave temperaturer forudsiger en stærk asymmetri afhængig af om kvanteprikken og kaviteten er ude af resonans, og som tillader en klar fortolkning af fysikken.

Et studie af uskelneligheden af enkelt fotoner udsendt fra det koblede kvanteprik-kavitet system bliver endvidere udført, med specielt fokus på ikke-Markovisk dekohærens på grund af vekselvirkningen med fononer. Vi viser at standard teoretiske tilgange fejler i at forudsige graden af uskelnelighed, på både et kvalitativt og kvantitativt niveau, for eksperimentelt relevante parameter regimer. Den vigtige rolle af ikke-Markoviske effekter i kort-tids regimet, hvor virtuelle processer dominerer tabet af kohærens i kvanteprik-kavitets systemet, bliver fremhævet. Et vigtigt resultat af vores undersøgelser er fremkomsten af en maksimum værdi af uskelneligheden, en forudsigelse som undviger standard teoretiske tilgange.

Acknowledgements

First and foremost I would like to thank my supervisors: Torben Roland Nielsen, Peter Lodahl, Antti-Pekka Jauho, and Jesper Mørk. I have been so fortunat to have as many as four experienced researchers, helping and guiding me through my Ph.D. project. Torben was always ready to share the tricks of the trade and assisted me in many technical issues. Peter was ever enthusiastic and helped keep the project on an experimentally relevant track. The willingness of Antti to share his vast knowledge of theoretical physics and guidance in general has been very valuable. Jesper has throughout the project been the main support in all manner of issues and I feel fortunate to have been allowed a very high degree of freedom during the project, while still being kept in the correct course.

I would like to thank the entire Nanophotonics Theory and Signal Processing Group at DTU Fotonik for cake and many interesting presentations at group meetings. Especially, I would like to thank Philip Trøst Kristensen, Niels Gregersen, and Michael Lorke for many scientific and technical discussions. Also, the many discussions with Anders Mølbjerg Lund, Anders Nysteen, and Mikkel Settnes have made my time during project much more interesting.

The guys at the experimental Quantum Photonics Group at NBI have been a continuous reminder of why we do physics. I have had many enlightening discussions on the experimental and general aspects of physics, especially Henri Thyrrestrup Nielsen, Kristian Høeg Madsen, and Søren Stobbe have been exposed to my company during these sessions.

My project would have been a whole deal more tedious if not for the countless cake events in office 166, in which I was gratefully allowed to participate despite my status as an office-outsider. So thank you Andrei Andryieuski, Thor Ansbæk, Sara Ek, Roza Shirazi, and Troels Suhr Skovgaard.

My thanks also goes to Jakob Houmark-Nielsen with whom I discussed many intricate details of semiconductors and the life of a Ph.D. student in general.

Last but not least, I would to thank my girlfriend, Solveig, for supporting me during my project, especially through periods of heavy workload.

Publications

Journal publications

1. P. Kaer, T. R. Nielsen, P. Lodahl, A.-P. Jauho, J. Mørk. *Microscopic theory of phonon-induced effects on semiconductor quantum dot decay dynamics in cavity QED.* Phys. Rev. B **86**, 085302 (2012).
   URL: http://link.aps.org/doi/10.1103/PhysRevB.86.085302

2. A. Moelbjerg, P. Kaer, M. Lorke, and J. Mørk. *Resonance Fluorescence from Semiconductor Quantum Dots: Beyond the Mollow Triplet.* Phys. Rev. Lett. **108**, 017401 (2012).
   URL: http://link.aps.org/doi/10.1103/PhysRevLett.108.017401

3. P. Kaer, T. R. Nielsen, P. Lodahl, A.-P. Jauho, J. Mørk. *Non-Markovian Model of Photon-Assisted Dephasing by Electron-Phonon Interactions in a Coupled Quantum-Dot-Cavity System.* Phys. Rev. Lett. **104**, 157401 (2010).
   URL: http://link.aps.org/doi/10.1103/PhysRevLett.104.157401

4. J. Mørk, P. Lunnemann, W. Xue, Y. Chen, P. Kaer, and T. R. Nielsen. *Slow and fast light in semiconductor waveguides.* Semiconductor Science and Technology **25**, 083002 (2010).
   URL: http://stacks.iop.org/0268-1242/25/i=8/a=083002

5. P. Kaer Nielsen, H. Thyrrestrup, J. Mørk, and B. Tromborg. *Numerical investigation of electromagnetically induced transparency in a quantum dot structure.* Opt. Express **15**, 6396 (2007).
   URL: http://www.opticsexpress.org/abstract.cfm?URI=oe-15-10-6396

Submitted publications

1. P. Kaer, P. Lodahl, A.-P. Jauho, and J. Mørk. *Microscopic theory of indistinguishable single-photon emission from a quantum dot coupled to a cavity: The role of non-Markovian phonon-induced decoherence.* arXiv:1203.6268v1. URL: http://arxiv.org/abs/1203.6268. Submitted for publication in Physical Review Letters.

2. A. Nysteen, P. Kaer, and J. Mørk. *Quenching of phonon-induced processes in quantum dots due to electron-hole asymmetries.* arXiv:1207:6878v1 URL: http://arxiv.org/abs/1207.6878v1. Submitted for publication in Physical Review Letters.

Publications in preparation

1. M. Settnes, P. Kaer, and J. Mørk. *Coulomb mediated correlations between wetting layer and quantum dot: Effect in cavity QED.* In preparation.

Invited conference contributions

1. P. Kaer, T.R. Nielsen, P. Lodahl, J. Mork, and A.-P. Jauho. *Break-down of the self-consistent Born approximation for LA+LO phonon interactions in quantum dots - an absorption spectra study.* Solving the Two-time Kadanoff-Baym Equations: Status and Open Problems, March 2010.

Conference contributions

1. A. Moelbjerg, P. Kaer, M. Lorke, and J. Mork. *Resonance fluorescence from quantum dots: Beyond the mollow triplet.* Conference on Lasers and Electro-Optics (CLEO) 2011, May 2011
2. P. Kaer, T.R. Nielsen, P. Lodahl, A. Jauho, and J. Mork. *Role of the lightmatter coupling strength on non-markovian phonon effects in semiconductor cavity qed.* Conference on Lasers and Electro-Optics Europe (CLEO EUROPE/EQEC) 2011, May 2011
3. P. Kaer, T.R. Nielsen, P. Lodahl, A. Jauho, and J. Mork. *Non-markovian effects in semiconductor cavity qed: Role of phonon-mediated processes.* The International Workshop on Nonlinear Optics and Excitation Kinetics in Semiconductors (NOEKS 10), August 2010
4. P. Kaer, T.R. Nielsen, P. Lodahl, and J. Mork. *Effect of temperature and phonons on the spectral properties of a multi-level semiconductor quantum dot single-photon source.* Conference on Lasers and Electro-Optics Europe (CLEO Europe - EQEC) 2009, June 2009
5. J. Mork, F. Ohman, M. van der Poel, P.L. Hansen, T.R. Nielsen, P.K. Nielsen, H. Thyrrestrup Nielsen, and K. Yvind. *Slow light in semiconductor waveguides: Theory and experiment.* Conference on Lasers and Electro-Optics Europe (CLEOE-IQEC 2007) 2007, June 2007
6. Per Nielsen, Henri Nielsen, Jesper Mork, and Bjarne Tromborg. *Pulse interactions in a quantum dot waveguide in the regime of electromagnetically induced transparency.* Conference on Lasers and Electro-Optics (CLEO/QELS 2006) 2006, May 2006

Contents

Chapter 1

Introduction

The quantum mechanical interaction between light and matter has been a central subject in modern physics ever since the advent of quantum theory in the 1920's. On the fundamental side, the extremely accurate measurements of the energetic Lamb shift, induced by the fluctuating vacuum field of photons, and the insistence of the theoretical community to understand it, lead to the production of the most precise scientific theory to date, namely quantum electrodynamics (QED). On the practical side, the ubiquity and importance of the modern semiconductor laser could not have reached the present day level, without a thorough understanding of the interaction between light and matter on the fundamental level.

Within the last few decades, research in quantum computing, and more generally quantum information technologies, has literally exploded. The central entity in a quantum computer is the qubit, which is a quantum mechanical generalization of the classical binary bit, that can be either in a “0” or “1” state. Being a quantum object, the qubit can exist in a general coherent superposition of “0” and “1”, formally represented as

$$|\mathrm{qubit}\rangle = \alpha\,|0\rangle + \beta\,|1\rangle\,, \tag{1.1}$$

where α and β are complex number satisfying $|\alpha|^2 + |\beta|^2 = 1$. The utility of a quantum computer arises from special quantum algorithms, employing qubits instead of classical bits. These can perform certain computational tasks which would not be feasible on any conceivable classical computer. The quest for suitable physical realizations of qubits and other components in a quantum computer, is a key element in many research proposals being submitted all over the world. This immense interest can partly be justified by the prospect of possible applications, however, this can only be part of story. To build a working quantum computer with dozens of qubits, requires deep insight into fundamental physics. This endeavor may even, through the study of decoherence, lead to a better understanding of the emergence of the macroscopic classical world in which we live. This multifaceted nature is certainly a great motivator for many researchers in this field.

Performing quantum computations with single photons as qubits would entail many advantages, due to the typical weak interaction of single photons with the environment. This was long thought to require strong optical non-linearities, which are inherently difficult to achieve at the single-photon level. However, the scheme proposed by Knill *et al.* [1] changed this perception and devised a way to perform efficient quantum computations employing only single-photon sources and detectors and standard linear optics component, such as phase shifters and beam-splitters. The greatest challenge of this scheme is to provide single-photon sources and detectors of sufficiently high quality, being able to emit and detect coherent and indistinguishable single photons. By their very nature, atoms are almost ideal single-photon sources (SPSs), having extremely well defined discrete energy levels and they can be efficiently isolated from the environment. These properties of atoms have long been exploited in the field of atomic cavity quantum electrodynamics (cQED) to perform extremely pure experiments, which are well-known to agree with theory to a very high degree. For performing proof-of-concept experiments atomic cQED is ideal, however they will probably never form the basis of an actual device, for which a more practical platform is imperative. Especially goals such as scalability, spatial control, and the ability to engineer properties to meet specific needs are hard to achieve in an atomic setting.

Enter the solid state. The progress in micro- and nanofabrication that ushered the microelectronics revolution, has produced amazing tools and techniques for structuring matter accurately on very small lengthscales. This has given birth to the field of solid-state quantum optics, where the confinement of both the electronic and electromagnetic degrees of freedom can be controlled and engineered to a high degree. Especially the invention of quantum dots in various forms, often referred to as artificial atoms due to their ability to confine electrons in three dimensions, was essential for providing an all-solid-state toolbox for performing quantum optics.

In the context of linear optical quantum computing, heterogeneous semiconductor structures have shown great promise as a mature practical platform. Placing a quantum dot (QD) inside an optical microcavity has long been considered as a strong candidate for a semiconductor SPS, which is essential for the scheme proposed in [1]. The processes involved in light emission from a QD embedded in an optical cavity are similar to those in a typical photoluminescence experiment, which we have illustrated schematically in fig. 1.1 using a semiconductor energy band diagram. The system is initially excited by means of, e.g., an optical pulse which creates an electron-hole pair in either the bulk or wetting layer continuum of surrounding the QD, see section 2.4.1. The carrier then relaxes down in energy by scattering off phonons and other carriers and eventually becomes captured by the QD. Once in the lowest excited state of the QD, the carrier will start interacting efficiently with the photons in the resonant cavity mode. The QD will either decay monotonous to its ground state under emission of a single-photon wavepacket or will re-absorb the emitted photon a number of times before being fully decayed. Which of these scenarios will be displayed, depends on the magnitude of the light-matter coupling strength compared to the loss rates and will place the system in either the weak or strong coupling regime.

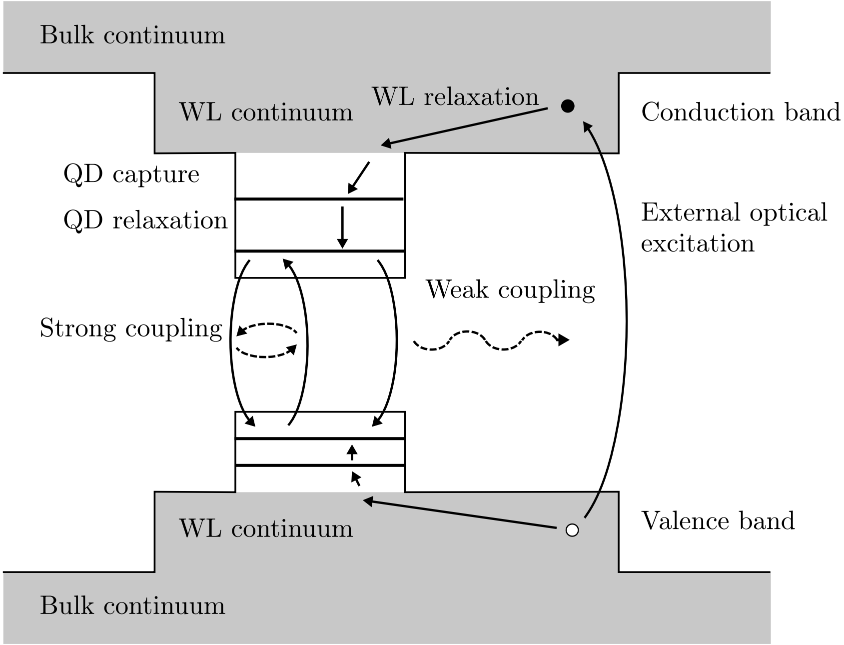

Figure 1.1: Energy band diagram illustrating the processes involved in light emission from a semiconductor SPS.

The nature of the different scattering mechanisms will all affect the quality and coherence of the single photons produced by the source. Also, it is clear that the environment experienced by the QD and cavity is significantly more complicated and rich compared to a corresponding experiment performed in atomic cQED. Despite of this realization, much physical insight and many physical pictures used to understand atomic cQED, have relatively uncritically been employed in semiconductor cQED. While the atomic ideas have proven useful on an overall qualitatively level, it has been unambiguously demonstrated experimentally [2, 3] that this is not generally the case. Especially the effect of Coulomb correlations amongst many carriers and the interaction with phonons, which have no atomic analogs, make it imperative to depart from many of the ideas developed in atomic cQED.

The theoretical description of atomic cQED systems has been highly successful and has recorded some of the best quantitative agreement between theory and experiment in the history of science. Part of this success is because of the ability to efficiently isolate a few levels in which the important physics takes place and due to a, in general, weak coupling to the environment. Both of these properties bode for an effective theoretical description, where a high degree of agreement with experiment can be expected. More often than not, none of these properties can be taken for granted in a theoretical description of a semiconductor cQED system. Especially the assumption of a weak coupling to the environment has to be challenged, and further the spectrum of the environment may be highly structured leading to inherent non-Markovian effects.

The main purpose of the present thesis is to theoretically investigate the effect of highly structured phonon reservoirs in semiconductor cQED and the ensuing non-Markovian effects that arise as an inevitable consequence. We will demonstrate that for a large class of experimentally relevant systems, standard approaches adopted from atomic cQED, will break down on both a quantitative and qualitative level. Specifically, we will focus on QD decay dynamics and the indistinguishability of single photons emitted from semiconductor cQED systems, both of which are important aspects of a SPS and we will show that a thorough understanding of phonon-induced effects is needed to design an efficient device.

The outline of the thesis is as follows:

In chapter 2 we present the theoretical framework and effective models employed in this thesis. The main approach is provided by the reduced density matrix (RDM) formalism, which has enjoyed enormous success in describing atomic cQED experiments. We will derive the Markovian limit if the theory, known as the Lindblad formalism, and also derive a non-Markovian generalization in the so-called time-convolutionless (TCL) form. Also the celebrated Quantum Regression Theorem (QRT) is derived and discussed, as well as its non-Markovian generalization. Finally, we briefly describe the effective models we employ to describe the semiconductor system.

Chapter 3 presents an investigation of QD decay dynamics in the presence of the electron-phonon interaction. This chapter was motivated by a series of experiment which could not be explained using traditional Markovian approaches. Indeed, we show that the effect of phonons can not in general be modeled using simple exponential decay rates and require a treatment that takes the quasi-particle nature of the cQED system into account in the reservoir interaction. We derive an analytical expression which clearly illustrates the physics and provide a simple explanation to why phonon effects appear to be more prominent in some samples compared to other seemingly similar. Also, we present a comparison with experiment showing excellent agreement.

The effect of the phonon interaction on single-photon indistinguishability is treated in chapter 4. Despite the importance of single-photon indistinguishability, only relatively simple theoretical studies have been performed, describing the effects of phonons in a simple rate treatment. In this chapter we rectify this situation and provide a full non-Markovian microscopic study and compare to standard approaches. We find that to cover the experimentally relevant parameter regime a full non-Markovian model is needed.

Finally, we present some highlights and an outlook in chapter 5.

Chapter 2

Modeling quantum dynamics in semiconductors

In this chapter we present the theoretical framework employed in this thesis. Our offset is the reduced density matrix (RDM) formalism which has been successfully used for decades in atomic cQED. The main advantage of this technique is the ability to treat part of a large system exactly, while treating other parts in an approximate fashion. In the context of semiconductor cQED this enables us to treat, e.g., the bound states of a QD, the cavity photon field and their interactions exactly, whereas typically more weakly coupled reservoirs can be included to some finite order. Relevant reservoirs might consist of phonons in the bulk or carriers in the wetting layer. This feature is relatively unique in many-body theory for semiconductors, as the two main toolboxes, namely the cluster expansion [4] and Green's function techniques [5], do not focus on this aspect.

We will derive the Lindblad formalism for including Markovian decay mechanisms, which works well for weakly coupled and weakly structured reservoirs. However, in the solid-state not all reservoirs are of this type and hence we also present a non-Markovian theory, known as the time-convolutionless (TCL) formalism, where the memory of the reservoir is included through time-dependent scattering rates.

For many experiments, knowledge of the one-time RDM is not sufficient and multi-time correlation functions are needed. For Markovian reservoirs these are routinely obtained using the Quantum Regression Theorem (QRT), where the equation(s) of motions (EOMs) for the RDM are the main ingredients. For a non-Markovian reservoir the QRT does however not hold and we follow a recent series of papers by Goan *et al.* [6, 7] and derive correctional terms to the QRT. Most of the theory presented can be found in textbooks on the subject [8, 9].

2.1 Closed systems

The dynamics of a closed quantum system is governed by the Schrödinger equation

$$i\hbar\partial_t \left|\psi(t)\right\rangle = H(t) \left|\psi(t)\right\rangle, \tag{2.1}$$

where $|\psi(t)\rangle$ is the wavefunction and $H(t)$ is the Hamiltonian operator. We use the term closed to signify that the quantum system is not embedded into a larger system with which it interacts. We will however allow for external, i.e. classical, sources to drive the system for which reason the Hamiltonian operator acquires a time-dependence

$$H(t) = H_\mathrm{s} + V(t), \tag{2.2}$$

where $V(t)$ describes the external source and H_s the internal quantum system. While the Schrödinger equation may be solved in the form presented in eq. (2.1) it is advantageous for many purposes to the introduce a time evolution operator $U(t, t_0)$, which propagates the wavefunction in time as

$$\left|\psi(t)\right\rangle = U(t, t_0) \left|\psi(t_0)\right\rangle, \tag{2.3}$$

from which it follows that $U(t_0, t_0) = I$. If we insert eq. (2.3) into eq. (2.1) we obtain the EOM for the time-evolution operator (TEO)

$$i\hbar\partial_t U(t, t_0) = H(t)U(t, t_0). \tag{2.4}$$

This equation may formally be solved using a time-ordered exponential

$$U(t, t_0) = T\left\{\exp\left(-i\hbar^{-1}\int_{t_0}^{t} dt' H(t')\right)\right\}, \tag{2.5}$$

with T being the forward time ordering operator [10]. In the case of time-independent Hamiltonian we simply get

$$U(t, t_0) = \exp\left(-i\hbar^{-1} H \times (t - t_0)\right). \tag{2.6}$$

The Schrödinger equation describes the evolution of so-called pure states, i.e., states described by a single wavefunction $|\psi(t)\rangle$. However, in many cases we deal with a statistical mixture of pure states described by a density matrix

$$\rho = \sum_n p_n \left|\psi_n\right\rangle \left\langle\psi_n\right|, \tag{2.7}$$

where the weights p_n can be obtained from, e.g., thermodynamical principles. The time-evolution of the density matrix is straight-forwardly obtained from eqs. (2.1) and (2.3) and we arrive at the Master equation

$$i\hbar\partial_t \rho(t) = \left[H(t), \rho(t)\right]. \tag{2.8}$$

So far we been working in the Schrödinger picture of quantum mechanics where states are time-dependent. In the so-called Heisenberg picture the operators, not the states, are time-dependent. It can be introduced as follows: Consider an expectation value of an operator A

$$\begin{aligned}\langle A(t)\rangle &= \mathrm{Tr}\left[\rho(t)A\right] && (2.9)\\ &= \mathrm{Tr}\left[U(t,t_0)\rho(0)U^\dagger(t,t_0)A\right] && (2.10)\\ &= \mathrm{Tr}\left[\rho(0)U^\dagger(t,t_0)AU(t,t_0)\right] && (2.11)\\ &= \mathrm{Tr}\left[\rho(0)A(t)\right], && (2.12)\end{aligned}$$

where the operators on the last line are in the Heisenberg picture, leading to the following definition of the Heisenberg picure

$$A(t) = U^\dagger(t,t_0)AU(t,t_0), \tag{2.13}$$

and with the following EOM

$$i\hbar\partial_t A(t) = \left[A(t), H(t)\right]. \tag{2.14}$$

Often it is advantageous to only treat part of the time-evolution explicitly, while accounting for the rest implicitly. This option is provided by the interaction picture or more generally by moving to an appropriate rotating frame. We treat the general case first and then specialize to the more common interaction picture. If we define the general rotating frame according to

$$\tilde{\rho}(t) = Q^\dagger(t,t_\mathrm{r})\rho(t)Q(t,t_\mathrm{r}), \tag{2.15}$$

where $Q(t,t_\mathrm{r})$ is an unitary operator, $Q^\dagger(t,t_\mathrm{r}) = Q^{-1}(t,t_\mathrm{r})$, and t_r is an arbitrary reference time for which $Q(t_\mathrm{r},t_\mathrm{r}) = I$, then the EOM for the density matrix transforms into

$$i\hbar\partial_t\tilde{\rho}(t) = \left[\tilde{H}(t) + \left[i\hbar\partial_t Q^\dagger(t,t_\mathrm{r})\right]Q(t,t_\mathrm{r}), \tilde{\rho}(t)\right]. \tag{2.16}$$

The TEO transforms a bit differently due to its special role and ends up as

$$\tilde{U}(t,t_0) = Q^\dagger(t,t_\mathrm{r})U(t,t_0)Q(t_0,t_\mathrm{r}) \tag{2.17}$$

In the more common case the unitary operator is given as the solution to a Schrödinger-like equation

$$i\hbar\partial_t Q(t,t_\mathrm{r}) = B(t)Q(t,t_\mathrm{r}) \tag{2.18}$$

where the unitarity of $Q(t,t_\mathrm{r})$ demands that $B(t)$ is hermitian, $B^\dagger(t) = B(t)$. The above equation is identical to eq. (2.4), hence the explicit forms given in eqs. (2.5) and (2.6) also holds. Here the Master equation reduces to

$$i\hbar\partial_t\tilde{\rho}(t) = \left[\tilde{H}(t) - B(t), \tilde{\rho}(t)\right]. \tag{2.19}$$

The interaction picture merely consists of a special choice of $B(t)$. In a typical application of the interaction picture, the internal part H_s of the total Hamiltonian in eq. (2.2) might be easy to diagonalize and the external part $V(t)$

might be complicated, thus we can maybe simplify the problem by choosing $B(t) = H_\mathrm{s}$. For this choice the explicit dependence on H_s drops out and the Master equation becomes

$$i\hbar\partial_t\tilde{\rho}(t) = \left[\tilde{V}(t), \tilde{\rho}(t)\right]. \tag{2.20}$$

The material presented above is basic textbook material and will mostly serve as a reference for remaining part of the thesis.

2.2 Open systems

Quantum systems are notoriously difficult to isolate from the surrounding environment, hence most theoretical models must include some kind of loss mechanism arising due to the coupling to the environment. The environment can in principle be thought of as just another system interacting with the system of main interest and which therefore is subject to a closed system description as presented in section 2.1. However, the large dimensionality of typical environments makes this line of thought impractical, and often impossible, to pursue in practice.

In this section we give an introduction to the theoretical formalism employed in this thesis, namely the RDM formalism. Its main virtues are a long and successful history in atomic quantum optics and the ability to treat parts of a large system exactly, while describing others at various levels of approximation.

2.2.1 The Reduced Density Matrix

In this section we give a basic derivation of the standard equation in RDM theory, namely the EOM to second order in the reservoir interaction Hamiltonian in a time-local or TCL form [9, 8].

We start by defining the total Hamiltonian

$$H(t) = H_\mathrm{S}(t) + H_\mathrm{R} + H_\mathrm{SR} = H_0(t) + H_\mathrm{SR}, \tag{2.21}$$

where $H_\mathrm{S}(t)$ is the, possibly time-dependent, Hamiltonian for the system of interest, H_R is the Hamiltonian for the reservoir, and H_SR is the interaction between the two subsystems. For notational simplicity we have introduced $H_0(t)$, being the sum of the free contributions.

The time evolution of the total density matrix, $\chi(t)$, is governed by the Master equation, eq. (2.8), in the Schrödinger picture

$$i\hbar\partial_t\chi(t) = [H(t), \chi(t)]. \tag{2.22}$$

Next we transform into the interaction picture with respect to $H_0(t) = H_\mathrm{S}(t) + H_\mathrm{R}$, to enable perturbation theory with respect to H_SR. The transformation operator $U_{H_0(t)}(t, t_0)$ satisfies the Schrödinger equation, eq. (2.18),

$$\begin{aligned} i\hbar\partial_t U_{H_0(t)}(t, t_0) &= \{H_\mathrm{S}(t) + H_\mathrm{R}\}\, U_{H_0(t)}(t, t_0) \\ &= H_0(t) U_{H_0(t)}(t, t_0), \end{aligned} \tag{2.23}$$

where t_0 is the initial time. Using eq. (2.5) we get

$$U_{H_0(t)}(t,t_0) = T\left\{\exp\left(-i\hbar^{-1}\int_{t_0}^{t} dt' H_0(t')\right)\right\}, \tag{2.24}$$

The interaction picture representation of the total density matrix is defined as

$$\tilde{\chi}(t) = U^{\dagger}_{H_0(t)}(t,t_0)\chi(t)U_{H_0(t)}(t,t_0), \tag{2.25}$$

which leads to the following equation of motion for $\tilde{\chi}(t)$

$$i\hbar\partial_t\tilde{\chi}(t) = \left[\tilde{H}_{\mathrm{SR}}(t),\tilde{\chi}(t)\right]. \tag{2.26}$$

This equation can be formally integrated

$$\tilde{\chi}(t) = \tilde{\chi}(t_0) - i\hbar^{-1}\int_{t_0}^{t} dt' \left[\tilde{H}_{\mathrm{SR}}(t'),\tilde{\chi}(t')\right]. \tag{2.27}$$

By inserting this expression into the right hand side of eq. (2.26) and tracing over the reservoir degrees of freedom, we obtain a formally exact equation for the RDM of the system

$$\begin{aligned} i\hbar\partial_t\tilde{\rho}(t) = {}& \mathrm{Tr}_{\mathrm{R}}\left\{\left[\tilde{H}_{\mathrm{SR}}(t),\tilde{\chi}(t_0)\right]\right\} \\ & - i\hbar^{-1}\int_{t_0}^{t} dt'\mathrm{Tr}_{\mathrm{R}}\left\{\left[\tilde{H}_{\mathrm{SR}}(t),\left[\tilde{H}_{\mathrm{SR}}(t'),\tilde{\chi}(t')\right]\right]\right\}, \end{aligned} \tag{2.28}$$

where $\rho(t) = \mathrm{Tr}_{\mathrm{R}}\{\chi(t)\}$ and $\mathrm{Tr}_{\mathrm{R}}\{\cdots\}$ denotes the trace operation with respect to the reservoir degrees of freedom. To proceed further we need to start invoking approximations. The first approximation, known as the Born approximation, states that the total density matrix on the right hand side of eq. (2.28) factorizes at all times, particularly at the initial time, hence

$$\chi(t) = \rho(t)R_0 \Leftrightarrow \tilde{\chi}(t) = \tilde{\rho}(t)\tilde{R}_0 = \tilde{\rho}(t)R_0, \tag{2.29}$$

where $R_0 = \tilde{R}_0$ is the density matrix for the reservoir, assumed to remain in this state at all times and hence being time-independent. This approximation is assumed to be valid for weak interaction between the system and reservoir. We shall assume that H_{SR} is written on the following form

$$H_{\mathrm{SR}} = \sum_{\nu\nu'} P_{\nu\nu'}B_{\nu\nu'}, \tag{2.30}$$

where $P_{\nu\nu'}$ is a pure system operator and $B_{\nu\nu'}$ is a pure reservoir operator. We assume that the reservoir has the following property

$$\mathrm{Tr}_{\mathrm{R}}\{R_0B_{\nu\nu'}\} = \langle B_{\nu\nu'}\rangle_0 = 0. \tag{2.31}$$

If we now use eqs. (2.29) and (2.31) in eq. (2.28) we get the following

$$\partial_t\tilde{\rho}(t) = -\hbar^{-2}\int_{t_0}^{t} dt'\mathrm{Tr}_{\mathrm{R}}\left\{\left[\tilde{H}_{\mathrm{SR}}(t),\left[\tilde{H}_{\mathrm{SR}}(t'),\tilde{\rho}(t')R_0\right]\right]\right\}, \tag{2.32}$$

which completes the formal derivation of equation of motion for the RDM.

To arrive at a more practical form of the EOM we expand the commutators, and rearrange the position of the $B_{\nu\nu'}$'s with respect to R_0 to obtain expectation values over the reservoir operators. Performing these steps yields

$$\begin{aligned}\partial_t\tilde{\rho}(t) = -\hbar^{-2}\int_{t_0}^{t} dt' \sum_{\nu_1\nu_2\nu_1'\nu_2'} \Big\{ \\ \left\{\tilde{P}_{\nu_1\nu_2}(t)\tilde{P}_{\nu_1'\nu_2'}(t')\tilde{\rho}(t') - \tilde{P}_{\nu_1'\nu_2'}(t')\tilde{\rho}(t')\tilde{P}_{\nu_1\nu_2}(t)\right\} \left\langle\tilde{B}_{\nu_1\nu_2}(t)\tilde{B}_{\nu_1'\nu_2'}(t')\right\rangle_0 \\ + \left\{\tilde{\rho}(t')\tilde{P}_{\nu_1'\nu_2'}(t')\tilde{P}_{\nu_1\nu_2}(t) - \tilde{P}_{\nu_1\nu_2}(t)\tilde{\rho}(t')\tilde{P}_{\nu_1'\nu_2'}(t')\right\} \left\langle\tilde{B}_{\nu_1'\nu_2'}(t')\tilde{B}_{\nu_1\nu_2}(t)\right\rangle_0 \Big\}.\end{aligned} \tag{2.33}$$

In its present form eq. (2.33) contains a memory integral with $\tilde{\rho}(t')$ as an integrand, therefore the time evolution depends on the past state of the system and is therefore non-Markovian. However, it is well-known that a non-Markovian description may also be obtained in a fully time-local theory, where the time evolution only depends on the present state of the system, but with time-dependent coefficients arising from the reservoir interaction. One example of such a theory is the TCL approach [9, 11, 12, 13]. In fact, if one makes the replacement $\tilde{\rho}(t') \to \tilde{\rho}(t)$ in eq. (2.33) the formal second order result in the TCL is recovered, which still describes a non-Markovian time-evolution. However, it is essential that this replacement is made within the interaction picture, where the only relevant time scale is the assumed slow time scale induced by the interaction with the reservoir [14]. In the present framework the replacement $t' \to t$ does not seem justified and could indicate an additional approximation. Surprisingly, this is often not the case [11] and the TCL tends to give more accurate results than its counterpart with memory integrals. To understand why the $t' \to t$ replacement does not introduce further approximations the full formal derivation of the TCL should be performed. We will not repeat the derivation here, but simply refer the reader to the literature, e.g. [9].

To complete the derivation of the second order RDM theory, we transform back to the Schrödinger picture and for completeness present both the TCL and memory integral results, even though only the TCL will used henceforth. In eq. (2.33) the interaction picture time-evolution is only governed by the free Hamiltonian of the respective subsystem, thus only the TEO for the system, namely

$$U(t,t_0) = T\left\{\exp\left(-i\hbar^{-1}\int_{t_0}^{t} dt' H_{\mathrm{S}}(t')\right)\right\}, \tag{2.34}$$

should be used when transforming eq. (2.33) back to the Schrödinger picture. We obtain

$$\partial_t\rho(t) = -i\hbar^{-1}\left[H_{\mathrm{S}}(t), \rho(t)\right] + S(t)\rho(t), \tag{2.35}$$

where we introduced the reservoir induced scattering term as

$$S(t)\rho(t) = U(t,t_0)[\partial_t\tilde{\rho}(t)]U^{\dagger}(t,t_0). \tag{2.36}$$

By employing relations such as

$$U(t,t_0)\tilde{\rho}(t')U^\dagger(t,t_0) = U(t,t')\rho(t')U^\dagger(t,t'), \tag{2.37}$$

and

$$U(t,t_0)\tilde{P}_{\nu_1\nu_2}(t')U^\dagger(t,t_0) = U(t,t')P_{\nu_1\nu_2}U^\dagger(t,t'), \tag{2.38}$$

we may derive the final form of the reservoir induced scattering $S(t)$ term for both the TCL and memory versions described above. The scattering term with memory becomes

$$\begin{aligned} S_{\text{MEM}}(t)\rho(t) = -\hbar^{-2}\int_{t_0}^{t} dt' \sum_{\nu_1\nu_2\nu_1'\nu_2'} \Big\{ \\ \big\{P_{\nu_1\nu_2}U(t,t')P_{\nu_1'\nu_2'}\rho(t')U^\dagger(t,t') - U(t,t')P_{\nu_1'\nu_2'}\rho(t')U^\dagger(t,t')P_{\nu_1\nu_2}\big\} \\ \times \langle\tilde{B}_{\nu_1\nu_2}(t)\tilde{B}_{\nu_1'\nu_2'}(t')\rangle \\ + \big\{U(t,t')\rho(t')P_{\nu_1'\nu_2'}U^\dagger(t,t')P_{\nu_1\nu_2} - P_{\nu_1\nu_2}U(t,t')\rho(t')P_{\nu_1'\nu_2'}U^\dagger(t,t')\big\} \\ \times \langle\tilde{B}_{\nu_1'\nu_2'}(t')\tilde{B}_{\nu_1\nu_2}(t)\rangle \Big\}, \end{aligned} \tag{2.39}$$

and the TCL one becomes

$$\begin{aligned} S_{\text{TCL}}(t)\rho(t) = -\hbar^{-2}\int_{t_0}^{t} dt' \sum_{\nu_1\nu_2\nu_1'\nu_2'} \Big\{ \\ \big\{P_{\nu_1\nu_2}U(t,t')P_{\nu_1'\nu_2'}U^\dagger(t,t')\rho(t) - U(t,t')P_{\nu_1'\nu_2'}U^\dagger(t,t')\rho(t)P_{\nu_1\nu_2}\big\} \\ \times \langle\tilde{B}_{\nu_1\nu_2}(t)\tilde{B}_{\nu_1'\nu_2'}(t')\rangle \\ + \big\{\rho(t)U(t,t')P_{\nu_1'\nu_2'}U^\dagger(t,t')P_{\nu_1\nu_2} - P_{\nu_1\nu_2}\rho(t)U(t,t')P_{\nu_1'\nu_2'}U^\dagger(t,t')\big\} \\ \times \langle\tilde{B}_{\nu_1'\nu_2'}(t')\tilde{B}_{\nu_1\nu_2}(t)\rangle \Big\}. \end{aligned} \tag{2.40}$$

It should be noted that the scattering terms presented in eqs. (2.39) and (2.40) have a mathematical structure, which does not guarantees the positivity of the RDM, i.e. diagonal elements of the RDM are not guaranteed to be positive, corresponding to negative populations. Positivity can be enforced by performing the secular approximation, consisting of employing a rotating wave approximation on certain terms in eqs. (2.39) and (2.40), see the discussion on pp. 127-131 in [9]. However, several of the physical effects we will be discussing later will be neglected in the secular approximation, hence we do not employ it. We note that the break-down of positivity has not been explicitly observed for the parameter regimes investigated in this thesis.

2.2.2 Lindblad formalism

In the situation where the reservoir correlation function decays much faster than any non-trivial timescale in the system, the scattering term in eq. (2.40) reduce to the well-known Lindblad form [15, 8]. We will derive two commonly used forms of the Lindblad theory using the more general theory presented in the previous section, namely one describing population decay and pure dephasing processes.

Phenomenological population decay terms can be derived using the following Hamiltonian, which would typically arise under the rotating-wave approximation,

$$H_{\text{pop}} = \hbar(aB^\dagger + a^\dagger B), \tag{2.41}$$

where $a \neq a^\dagger$ is a system operator and B is an effective reservoir operator, containing the matrix elements describing the interaction between the system and reservoir. Using eq. (2.40) we obtain

$$\begin{aligned} S_{\text{pop}}(t)\rho(t) = -\int_0^t d\tau \Big\{ &\left[a^\dagger \tilde{a}(-\tau)\rho(t) - \tilde{a}(-\tau)\rho(t)a^\dagger\right] \langle \tilde{B}(\tau)B^\dagger\rangle \\ &+ \left[\rho(t)\tilde{a}(-\tau)a^\dagger - a^\dagger\rho(t)\tilde{a}(-\tau)\right] \langle B^\dagger \tilde{B}(\tau)\rangle + \text{h.c.}\Big\}, \end{aligned} \tag{2.42}$$

where we have assumed $\langle BB\rangle = \langle B^\dagger B^\dagger\rangle = 0$ and used

$$\langle \tilde{B}(\tau)B^\dagger\rangle = \langle \tilde{B}(t-t')B^\dagger\rangle = \langle \tilde{B}(t)\tilde{B}^\dagger(t')\rangle\,. \tag{2.43}$$

We also assume that any external time-dependence in the system Hamiltonian is slow enough compared the decay of the reservoir correlation functions that it can be neglected, hence the TEO of the system, eq. (2.34), becomes a function of one time $U(\tau) = U(t-t')$. To arrive at the simple Lindblad result, we further have to assume that the time-evolution arising due to off-diagonal terms in the system Hamiltonian H_{S} is slow compared to that induced by free or diagonal terms. If this is the case then

$$\tilde{a}(-\tau) \approx a e^{i\omega_a \tau}, \tag{2.44}$$

where ω_a is the transition frequency corresponding to the transition induced by a. Using this results in

$$S_{\text{pop}}(t)\rho(t) = -\frac{\Gamma_{\text{I}}(t)}{2}\left[a^\dagger a\rho(t) - a\rho(t)a^\dagger\right] - \frac{\Gamma_{\text{II}}(t)}{2}\left[\rho(t)aa^\dagger - a^\dagger\rho(t)a\right] + \text{h.c.} \tag{2.45}$$

where we have defined the time-dependent rates

$$\begin{aligned} \Gamma_{\text{I}}(t) &= 2\int_0^t d\tau e^{i\omega_a\tau}\langle \tilde{B}(\tau)B^\dagger\rangle\,, \\ \Gamma_{\text{II}}(t) &= 2\int_0^t d\tau e^{i\omega_a\tau}\langle B^\dagger\tilde{B}(\tau)\rangle\,. \end{aligned} \tag{2.46}$$

As an example let us consider the case where the reservoir consists of a continuum of bosons, which is very often the case, so we write

$$B = \sum_k g_k b_k, \tag{2.47}$$

where b_k is the bosonic operator for boson mode k and g_k is the interaction matrix element. Assuming the free Hamiltonian of the bosons to be of the form

$$H_{\mathrm{B}} = \sum_k \hbar\omega_k b_k^\dagger b_k, \tag{2.48}$$

the reservoir correlation function $\langle \tilde{B}(\tau) B^\dagger \rangle$ can be written as

$$\langle \tilde{B}(\tau) B^\dagger \rangle = \sum_k |g_k|^2 (1 + n_k) e^{-i\omega_k \tau}, \tag{2.49}$$

where n_k is the thermal occupation of mode k. Inserting this into eq. (2.46) yields

$$\Gamma_{\mathrm{I}}(t) = 2 \int_0^t d\tau \sum_k |g_k|^2 (1 + n_k) e^{i(\omega_a - \omega_k)\tau}. \tag{2.50}$$

Now, if n_k and g_k vary slowly compared to ω_k in the vicinity of $\omega_k \approx \omega_a$ then the integrand will be strongly peaked near $\tau \approx 0$ and the upper integration limit may be set to infinity. We may then perform the time integral to arrive at

$$\Gamma_{\mathrm{I}}(\infty) = 2 \sum_k |g_k|^2 (1 + n_k) \left\{ i\mathcal{P}\frac{1}{\omega_a - \omega_k} + \pi\delta(\omega_a - \omega_k) \right\}, \tag{2.51}$$

where $\mathcal{P}$ refers to the principal value of the integral. The imaginary part of $\Gamma_{\mathrm{I}}(\infty)$ gives rise to an energy shift, usually referred to as the Lamb shift, however for phenomenological treatments it can safely be absorbed into the system Hamiltonian. This leaves us with the real part which enters as a decay rate in the EOM

$$\begin{aligned} \Gamma_{\mathrm{I}} &= 2\pi \int d\omega d(\omega) |g(\omega)|^2 [1 + n(\omega)] \delta(\omega_a - \omega) && (2.52) \\ &= 2\pi d(\omega_a) |g(\omega_a)|^2 [1 + n(\omega_a)], && (2.53) \end{aligned}$$

where we have transitioned to an integral form, introduced the density of states function $d(\omega)$, and evaluated the integral. The decay rate is seen to sample the physical quantities exactly at the transition energy of a. Similarly for Γ_{II} we obtain

$$\Gamma_{\mathrm{II}} = 2\pi d(\omega_a) |g(\omega_a)|^2 n(\omega_a). \tag{2.54}$$

If we introduce the notation $\Gamma = 2\pi d(\omega_a)|g(\omega_a)|^2$ and $n = n(\omega_a)$ we finally obtain the usual expression for Lindblad decay

$$\begin{aligned} L_{\Gamma,n}\{a\}\rho(t) = &-\frac{\Gamma}{2}(1 + n) \left[a^\dagger a \rho(t) + \rho(t) a^\dagger a - 2a\rho(t)a^\dagger \right] \\ &- \frac{\Gamma}{2} n \left[\rho(t) a a^\dagger + a a^\dagger \rho(t) - 2a^\dagger \rho(t) a \right] \qquad (2.55) \end{aligned}$$

We note that usually the effective temperature is assumed to be zero, compared to typical reservoir energyscales, hence $n = 0$ is almost exclusively employed.

To model pure dephasing processes we can employ the same Hamiltonian as for population decay if we choose $a = a^\dagger$, hence

$$H_{\mathrm{pd}} = \hbar a(B^\dagger + B). \tag{2.56}$$

One may now go through the same procedure as described above leading to the following scattering term

$$L_{\gamma,n}\{a\}\rho(t) = -\gamma(1+2n)\left[aa\rho(t) + \rho(t)aa - 2a\rho(t)a\right], \tag{2.57}$$

where $\gamma = 2\pi d(0)|g(0)|^2$ and $n = n(0)$. It is interesting note that as the system operator a for pure dephasing does not correspond to an actual transition, but rather a virtual transition, the reservoir is sampled at zero frequency. Whether or not this gives rise to a non-zero pure dephasing rate depends on the reservoir, but the structure of the scattering term gives rise to decay of off-diagonal elements of the RDM, with no associated population decay.

2.2.3 A discussion of timescales

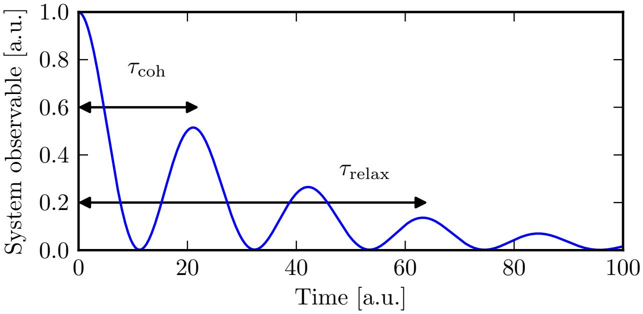

Figure 2.1: Illustration of the coherent timescale τ_{coh} *and relaxation timescale* τ_{relax}*, for a typical system observable.*

In the previous sections we have discussed the relevant regimes of open system dynamics, namely the non-Markovian regime embodied in the TCL scattering terms, eq. (2.40), and the Markovian regime described by the Lindblad theory, eqs. (2.55) and (2.57). Much of this thesis will deal with detailed discussions of these two regimes and hence it is useful with more clear definitions of the regimes in terms of the involved timescales.

For a typical open quantum system we have three important timescales, whose mutual values will determine whether we are in the non-Markovian or Markovian regime. The first is the coherent timescale, τ_{coh}, which is determined by the coherent or unitary part of the time-evolution given by the system Hamiltonian, and enters in the TEO, $U(t,t')$, in eq. (2.40). The order of magnitude of this timescale is given by the inverse of the difference between two typical eigenenergies of the system, $\tau_{\mathrm{coh}} \approx |\omega_i - \omega_j|^{-1}$. The second is the typical relaxation timescale of the system, τ_{relax}. The relaxation timescale emerges from the overall dynamics of the system and can not be as clearly defined as τ_{coh}. The coherent and relaxation timescales are illustrated in fig. 2.1 for the time-evolution of a typical system observable. The last timescale is that introduced by the decay of the reservoir correlation function, τ_{corr}, that enters in the TCL scattering term, eq. (2.40). This timescale depends both on the properties of the undisturbed reservoir, i.e. dispersion, mode density, temperature, etc., and on the details of how it interacts with the system in question, for a few examples in the case of a typical phonon reservoir see section 3.2.6.

The simplest regime is the Markovian one, in which the following relationship holds

$$\tau_{\mathrm{corr}} \ll \tau_{\mathrm{coh}},\ \tau_{\mathrm{relax}}, \tag{2.58}$$

hence the correlations with reservoir decay much faster than any other timescale in the system. This allows us to make the approximation in eq. (2.44), which is the formal difference between the Lindblad and TCL formalisms, where only the free time-evolution is taking into account in the reservoir scattering terms. Physically this approximation means that the reservoir will only interact with bare particles in the system and not the quasi-particles that might arise due to internal coupling mechanisms. In the frequency domain this corresponds to the reservoir spectrum being approximately constants over the spectral bandwidth of the quasi-particle.

In the non-Markovian regime we have the situation

$$\tau_{\mathrm{corr}} \approx \tau_{\mathrm{coh}},\ \tau_{\mathrm{relax}}, \tag{2.59}$$

hence correlations with the reservoir exists on timescales where the system undergoes coherent evolution. In this regime memory-effects are essential to include and the possible quasi-particle nature of the system constituents can not be ignored. Spectrally, this situation corresponds to the reservoir spectrum having considerable variations over the bandwidth of the system quasi-particles.

Depending on the value of τ_{relax} compared to the other timescales, it may be an excellent approximation to extend the upper limit in the time-integral in eq. (2.40) to infinity, hence only considering the long-time, and time-independent, limit of the TCL rates. In the long-time limit the processes contained in the TCL rates all conserve energy, in the sense that they only sample the reservoir spectrum at specific energies. For this reason the long-time limit is often referred to as the Markovian limit. However, in the Lindblad theory the long-time limit is exact due to the assumption of a delta-correlated reservoir, hence the Markovian limit applies at all times. As we shall investigate in much greater detail, specifically in section 3.2.4, the Lindblad formalism and the long-time limit of the TCL are not equivalent. The essential difference arises due to the memory effects allowed by the TCL theory, which gives rise to a different mathematical structure of the long-time TCL scattering terms, compared to the Lindblad regime. For this reason we will not refer to the long-time limit of the TCL as the Markovian regime, but rather as the long-time non-Markovian regime. When $t \lesssim \tau_{\mathrm{corr}}$ the TCL rates are explicitly time-dependent and the scattering processes need not conserve energy and non-Markovian effects may dominate the dynamics. We will call this the short-time non-Markovian regime.

The above discussion has been summarized in table 2.1.

timescales	upper integration limit	regime
$\tau_{\mathrm{corr}} \ll \tau_{\mathrm{coh}},\ \tau_{\mathrm{relax}}$	$t_{\mathrm{upper}} \to \infty$	Markovian
$\tau_{\mathrm{corr}} \approx \tau_{\mathrm{coh}},\ \tau_{\mathrm{relax}}$	$t_{\mathrm{upper}} \lesssim \tau_{\mathrm{corr}}$	short-time non-Markovian
$\tau_{\mathrm{corr}} \approx \tau_{\mathrm{coh}},\ \tau_{\mathrm{relax}}$	$t_{\mathrm{upper}} \gg \tau_{\mathrm{corr}}$	long-time non-Markovian

Table 2.1: Summary of relevant timescales and corresponding regimes.

2.3 Multi-time correlation functions

In the previous section we derived EOM for the RDM in the presence of both Markovian and non-Markovian reservoirs. Knowledge of the RDM allows one to calculate the expectation value of any system operator at a single time through the formula

$$\langle A(t)\rangle = \mathrm{Tr}_{\mathrm{S}}\left[A\rho(t)\right]. \tag{2.60}$$

Using this one may investigate, e.g., population dynamics, input-output curves for lasers, and linear response quantities. However, for a large class of quantum optical experiments, knowledge of the RDM is not sufficient to predict the outcome. These include measuring the emission spectra of light, coherence properties of lasers, indistinguishability of single photons, and bunching experiments in general, here multi-time correlation functions are needed.

In the following sections we describe how to calculate two-time correlation functions. First, we derive the celebrated QRT which applies for systems in contact with Markovian reservoirs. Next, we consider the corrections needed in order to calculate two-time correlation functions for non-Markovian reservoirs.

2.3.1 The Markovian Quantum Regression Theorem

To derive the Markovian QRT we consider first a one-time expectation value, eq. (2.9), for a system operator A

$$\langle A(t)\rangle = \mathrm{Tr}_{\mathrm{SR}}\left[A\chi(t)\right] \tag{2.61}$$

$$= \mathrm{Tr}_{\mathrm{S}}\left[A\mathrm{Tr}_{\mathrm{R}}\left[U(t)\chi(0)U^{\dagger}(t)\right]\right] \tag{2.62}$$

where for simplicity we assume $t_0 = 0$ and a time-independent Hamiltonian for both the system and reservoir, hence $U(t,t_0) = U(t-t_0) = U(t) = \exp(-iHt/\hbar)$. The RDM

$$\rho(t) = \mathrm{Tr}_{\mathrm{R}}\left[U(t)\chi(0)U^{\dagger}(t)\right], \tag{2.63}$$

enters in this expression as the central quantity, for which we derived an EOM for in section 2.2.1. Generalizing to a two-time expectation value we get

$$\langle A(t+\tau)B(t)\rangle = \mathrm{Tr}_{\mathrm{SR}}\left[U^\dagger(t+\tau)AU(t+\tau)U^\dagger(t)BU(t)\chi(0)\right] \tag{2.64}$$

$$= \mathrm{Tr}_{\mathrm{S}}\left[A\mathrm{Tr}_{\mathrm{R}}\left[U(\tau)BU(t)\chi(0)U^\dagger(t)U^\dagger(\tau)\right]\right] \tag{2.65}$$

$$= \mathrm{Tr}_{\mathrm{S}}\left[A\mathrm{Tr}_{\mathrm{R}}\left[U(\tau)B\chi(t)U^\dagger(\tau)\right]\right], \tag{2.66}$$

where $\tau \geq 0$. If we compare eqs. (2.62) and (2.66) they seem rather similar, where eq. (2.62) has the RDM, $\rho(t)$, and its time-evolution in t, eq. (2.66) contains a modified RDM

$$\rho_{B;t}(\tau) = \mathrm{Tr}_{\mathrm{R}}\left[U(\tau)B\chi(t)U^\dagger(\tau)\right], \tag{2.67}$$

which is evolved in the difference time τ. Naively, this comparison might lead to the conclusion that two-time averages can be calculated similarly to one-time averages, i.e., using the EOM for the RDM. However, the simple form of the scattering terms for the RDM was obtained assuming an initially uncorrelated state between the system and reservoir, formally expressed as

$$\chi(0) = \rho(0) \otimes R_0. \tag{2.68}$$

Translating this assumption to the two-time expectation value in eq. (2.66) leads to

$$\chi(t) = \rho(t) \otimes R_0, \tag{2.69}$$

for all times t. The factorization at all times is a much more severe approximation, compared to only demanding a factorized initial state. In fact, the factorization expressed in eq. (2.69) corresponds to assuming a memory-less reservoir and hence non-Markovian effects can not be treated. This might not be immediately clear, but can loosely be understood through the following argument: Memory effects arise when a reservoir is integrated out and correlations existed between the reservoir and the remaining part of the system. Hence, if the reservoir and system are not correlated, no memory effects are present and the interaction between the two is by definition Markovian. The factorization at all times should not be confused with the Born approximation expressed in eq. (2.29), as the factorization contained in the Born approximation was only applied in terms which were to second order in the interaction Hamiltonian between the system and reservoir. Thus, the Born approximation allows correlations to build up to and including second order in the interaction Hamiltonian, whereas eq. (2.69) does not allow any correlations. This point is discussed in [16, 17] and in the context of the Langevin formalism in [18].

Enforcing the factorization in eq. (2.69) we arrive at the famous QRT stating that two-time averages can be calculated knowing only how one-time averages evolve in time. To arrive at a more practical formulation let us consider the EOM, eq. (2.35), for the RDM

$$\partial_t\rho(t) = -i\hbar^{-1}\left[H_{\mathrm{S}}, \rho(t)\right] + S(t\to\infty)\rho(t) \equiv \mathcal{L}\rho(t). \tag{2.70}$$

The notation $S(t \rightarrow \infty)$ indicates that the long-time must be taken in any kind of scattering term, to stay consistent with the factorization assumption in eq. (2.69). Also we introduced the super-operator $\mathcal{L}$, often denoted the Liouvillian, to represent the time-evolution of the RDM. In practice, this formulation may be obtained by remapping the matrix representing RDM to a vector form in which $\mathcal{L}$ becomes a matrix, instead of a tensor which is the case in the above. The QRT now states that the modified RDM, eq. (2.67), is governed by the same EOM as $\rho(t)$, hence

$$\partial_\tau \rho_{B;t}(\tau) = \mathcal{L}\rho_{B;t}(\tau), \tag{2.71}$$

with the initial condition $\rho_{B;t}(\tau = 0) = B\rho(t)$. Any two-time average of system operators can now simply be calculated as

$$\langle A(t+\tau)B(t)\rangle = \mathrm{Tr}_\mathrm{S}\left[A\rho_{B;t}(\tau)\right]. \tag{2.72}$$

An even more explicit form may be obtained by noting that the solution of linear equations of the form $\partial_t x(t) = Mx(t)$ can be written as

$$x(t) = e^{Mt}x(0), \tag{2.73}$$

where the matrix exponential may be evaluated using a variety of methods [19]. Using this the two-time expectation value can be written compactly as

$$\langle A(t+\tau)B(t)\rangle = \mathrm{Tr}_\mathrm{S}\left[Ae^{\mathcal{L}\tau}Be^{\mathcal{L}t}\rho(0)\right]. \tag{2.74}$$

The extension of the QRT to more than two times is rather trivial and is described in most textbooks on quantum optics, e.g. [8].

2.3.2 Non-Markovian corrections

As discussed in the previous section the essential assumption leading to the QRT was the factorization of the total density matrix at all times, into a system and reservoir part. The factorization implied a delta-correlated or memory-less reservoir and hence the QRT is inherently unable to describe non-Markovian reservoirs. In this section we will derive correctional terms to the QRT enabling the consistent treatment of non-Markovian reservoirs. We follow the recently published approach of Goan *et al.* [6, 7], providing the correctional terms within a general RDM framework. We note that other authors have discussed similar extensions to the QRT [20, 21, 22], however within a less general context.

We start by assuming a time-independent system Hamiltonian and for simplicity set $t_0 = 0$, as was done in the previous section, and combine eqs. (2.26) and (2.27) to obtain a EOM to second order in the interaction Hamiltonian for the total density matrix

$$\begin{aligned}\partial_t \chi(t) = \frac{1}{i\hbar}\left[H_0, \chi(t)\right] + \frac{1}{i\hbar}U_{H_0}(t)\left[\tilde{H}_\mathrm{SR}(t), \chi(0)\right]U^\dagger_{H_0}(t) \\ - \frac{1}{\hbar^2}\int_0^t dt'\left[H_\mathrm{SR}, \left[\tilde{H}_\mathrm{SR}(t'-t), \chi(t)\right]\right].\end{aligned} \tag{2.75}$$

This EOM is in the Schrödinger picture and we have anticipated the TCL and made the replacement $\chi(t') \to \chi(t)$ under the time integral, while still in the interaction picture. For reasons that will later become clear, we formulate the equations in the Heisenberg picture, rather than in a Schrödinger-like picture as was done for the QRT. To this end it is useful to first consider the equation for a one-time average. Using eq. (2.75) we immediately get

$$\begin{aligned}\partial_t \langle A(t)\rangle &= \mathrm{Tr}_{\mathrm{SR}}\{A\partial_t\chi(t)\} && (2.76)\\ &= -i\hbar^{-1}\mathrm{Tr}_{\mathrm{SR}}(A\,[H_0,\chi(t)]) && (2.77)\\ &\quad - \hbar^{-2}\int_0^t dt'\mathrm{Tr}_{\mathrm{SR}}\Big(A\left[H_{\mathrm{SR}},\left[\tilde{H}_{\mathrm{SR}}(t'-t),\chi(t)\right]\right]\Big), && (2.78)\end{aligned}$$

where the second term in eq. (2.75) involving the initial total density matrix is zero due to eq. (2.31). This may be reformulated as

$$\begin{aligned}\partial_t \langle A(t)\rangle = i\hbar^{-1}&\mathrm{Tr}_{\mathrm{SR}}[\{[H_{\mathrm{S}},A]\}(t)\chi(0)]\\ &+\hbar^{-2}\int_0^t dt'\mathrm{Tr}_{\mathrm{SR}}\Big(\Big\{\tilde{H}_{\mathrm{SR}}(t'-t)\,[A,H_{\mathrm{SR}}]\Big\}(t)\chi(0)\\ &\qquad+\Big\{[H_{\mathrm{SR}},A]\,\tilde{H}_{\mathrm{SR}}(t'-t)\Big\}(t)\chi(0)\Big), \qquad (2.79)\end{aligned}$$

where we have reorganized the commutators by cycling different operators under the trace operation moving $\chi(0)$ to the right and switched to the Heisenberg picture, where

$$\{AB\}(t) = U_H^\dagger(t)ABU_H(t) \qquad (2.80)$$

signifies Heisenberg time-evolution. We note that we have not yet made the second order Born approximation on the right hand side (RHS) of eq. (2.79), which is slightly more difficult to apply in the Heisenberg picture than in the Schrödinger picture.

We now proceed to the two-time averages. Similarly to eq. (2.66) we write a general two-time average of system operators as

$$\langle A(t+\tau)B(t)\rangle = \mathrm{Tr}_{\mathrm{SR}}\left[AU(\tau)B\chi(t)U^\dagger(\tau)\right] = \mathrm{Tr}_{\mathrm{SR}}[A\,\{B\chi(t)\}\,(\tau)]\,. \qquad (2.81)$$

The time-evolution with respect to τ is given as

$$\partial_\tau \langle A(t+\tau)B(t)\rangle = \mathrm{Tr}_{\mathrm{SR}}[A\partial_\tau\,\{B\chi(t)\}(\tau)]\,, \qquad (2.82)$$

where the EOM governing the evolution is of the form eq. (2.75). We now proceed analogously to the one-time average, achieved with the simple replacement $\chi(0) \to B\chi(t)$ yielding

$$\begin{aligned}\partial_\tau \langle A(t+\tau)B(t)\rangle = i\hbar^{-1}&\mathrm{Tr}_{\mathrm{SR}}(\{[H_{\mathrm{S}},A]\}(t+\tau)B(t)\chi(0))\\ +\hbar^{-2}&\int_0^\tau dt'\mathrm{Tr}_{\mathrm{SR}}\Big(\Big\{\tilde{H}_{\mathrm{SR}}(t'-\tau)\,[A,H_{\mathrm{SR}}]\Big\}(t+\tau)B(t)\chi(0)\\ &+\Big\{[H_{\mathrm{SR}},A]\,\tilde{H}_{\mathrm{SR}}(t'-\tau)\Big\}(t+\tau)B(t)\chi(0)\Big) + C(t+\tau,t). \qquad (2.83)\end{aligned}$$

Comparing the two first terms with eq. (2.79) we find an identical structure, which are the QRT contributions. However, a third term is found in the two-time average which is not present in the one-time average, namely

$$C(t+\tau,t) = -i\hbar^{-1}\mathrm{Tr}_{\mathrm{SR}}\Big\{AU_{H_0}(\tau)\left[\tilde{H}_{\mathrm{SR}}(\tau), B\chi(t)\right]U^{\dagger}_{H_0}(\tau)\Big\} \tag{2.84}$$

$$= -i\hbar^{-1}\mathrm{Tr}_{\mathrm{SR}}\Big\{\tilde{A}(\tau)\left[\tilde{H}_{\mathrm{SR}}(\tau), B\chi(t)\right]\Big\}. \tag{2.85}$$

This term is related to initial correlations, at $\tau = 0$, for the modified RDM eq. (2.67), $\rho_{B;t}(\tau) = \mathrm{Tr}_{\mathrm{R}}\left[U(\tau)B\chi(t)U^{\dagger}(\tau)\right]$. As discussed in the previous section a Markovian reservoir implies that $\chi(t) = \rho(t)\otimes R_0$, which through eq. (2.31) would lead to $C(t+\tau,t) = 0$ and hence the QRT is recovered. For a non-Markovian reservoir the factorization is not valid and therefore in general $C(t+\tau,t) \neq 0$. As it presently stands, the correctional term is explicitly first order in the interaction Hamiltonian. To obtain a second order result consistent with the second order Born approximation, we expand the total density matrix $\chi(t)$ to first order in the interaction Hamiltonian. From eq. (2.27) we get

$$\chi(t) = U_{H_0}(t)\chi(0)U^{\dagger}_{H_0}(t) - i\hbar^{-1}\int_0^t dt'\left[\tilde{H}_{\mathrm{SR}}(t'-t), \chi(t)\right], \tag{2.86}$$

where TLC replacement was employed under the memory integral as in eq. (2.75). Inserting this into the above expression for $C(t+\tau,t)$ and rearranging the commutators yields

$$C(t+\tau,t) = \hbar^{-2}\int_0^t dt'\mathrm{Tr}_{\mathrm{SR}}\Big(\left[\tilde{H}_{\mathrm{SR}}(\tau), \tilde{A}(\tau)\right]B\tilde{H}_{\mathrm{SR}}(t'-t)\chi(t) + \tilde{H}_{\mathrm{SR}}(t'-t)\left[\tilde{A}(\tau), \tilde{H}_{\mathrm{SR}}(\tau)\right]B\chi(t)\Big), \tag{2.87}$$

where the term including $\chi(0)$ evaluates to zero under eq. (2.31). The second order Born approximation could now be employed in $C(t+\tau,t)$ and the two-time averages, eq. (2.83), could be propagated throughout the two-time plane. However, eq. (2.87) does not include any two-time averages, only one-time averages, making $C(t+\tau,t)$ an inhomogeneous term in eq. (2.83). To restore the EOM for $\langle A(t+\tau)B(t)\rangle$ to a homogeneous form, Goan *et al.* [6, 7] replace the interaction picture time-evolution operator with respect to τ with the corresponding one in the Heisenberg picture. Formally, this is achieved by $\tilde{O}(\tau) \to O(\tau)$ and justified referring to the second order Born approximation, where $U_H(\tau) \approx U_{H_0}(\tau) + \mathcal{O}(H_{\mathrm{SR}})$ can be employed. This introduces a new level of self-consistency in the EOM and the inhomogeneity is lifted. The argument for elevating time-evolution with respect to τ from the interaction picture to the Heisenberg picture could, however, equally well have been made for the time-evolution with respect to $t'-t$. The formal reason for preferring τ time-evolution is not completely clear to the present author, other than it yields the wanted result.

Performing this step and moving to the Heisenberg picture the final EOM for $\langle A(t+\tau)B(t)\rangle$ becomes

$$\begin{aligned}\partial_\tau \langle A(t+\tau)B(t)\rangle &= i\hbar^{-1}\mathrm{Tr}_{\mathrm{SR}}(\{[H_{\mathrm{S}},A]\}(t+\tau)B(t)\chi(0)) \\ &\quad + \hbar^{-2}\int_0^\tau dt'\mathrm{Tr}_{\mathrm{SR}}\Big(\Big\{\tilde{H}_{\mathrm{SR}}(t'-\tau)\,[A,H_{\mathrm{SR}}]\Big\}(t+\tau)B(t)\chi(0) \\ &\qquad + \Big\{[H_{\mathrm{SR}},A]\,\tilde{H}_{\mathrm{SR}}(t'-\tau)\Big\}(t+\tau)B(t)\chi(0)\Big) \\ &\quad + \hbar^{-2}\int_0^t dt'\mathrm{Tr}_{\mathrm{SR}}\Big(\{[H_{\mathrm{SR}},A]\}(t+\tau)\Big\{B\tilde{H}_{\mathrm{SR}}(t'-t)\Big\}(t)\chi(0) \\ &\qquad + \Big\{\tilde{H}_{\mathrm{SR}}(t'-[t+\tau])\,[A,H_{\mathrm{SR}}]\Big\}(t+\tau)B(t)\chi(0)\Big). \end{aligned} \tag{2.88}$$

The reason for formulating the equations in the Heisenberg picture, rather than in an effective Schrödinger picture using the modified RDM of eq. (2.67), can now be understood. If we consider all but the fourth line in the above equation, we notice that the two right-most operators in all cases are $B(t)\chi(0)$, corresponding to the modified RDM $\rho_{B;t}(\tau)$. However, the non-Markovian corrections on line four are seen to generally break this structure, introducing couplings to other modified RDMs $\rho_{D;t}(\tau)$, where $D \neq B$, hence removing the advantage of introducing the modified RDM.

While the derivation of the non-Markovian corrections to the QRT is complete in eq. (2.88), the form can be made more practical by assuming a specific form of the interaction Hamiltonian, allowing us to explicitly perform the second order Born approximation. We assume the following form of the interaction Hamiltonian, which does not limit the generality of the theory,

$$H_{\mathrm{SR}} = \sum_{\nu_1\nu_2} P_{\nu_1\nu_2}R_{\nu_1\nu_2}, \tag{2.89}$$

where $P_{\nu_1\nu_2}$ is a system operator and $R_{\nu_1\nu_2}$ is a reservoir operator. For a reservoir density matrix R_0 commuting with $U_{H_{\mathrm{R}}}(t)$, the two-time reservoir correlation functions depend only on time differences

$$D_{\nu_1\nu_2\nu_3\nu_4}(t-t') = \mathrm{Tr}_R\left[\tilde{R}_{\nu_1\nu_2}(t)\tilde{R}_{\nu_3\nu_4}(t')R_0\right] = \mathrm{Tr}_R\left[\tilde{R}_{\nu_1\nu_2}(t-t')R_{\nu_3\nu_4}R_0\right]. \tag{2.90}$$

If we assume the following property

$$R^\dagger_{\nu_1\nu_2} = R_{\nu_2\nu_1}, \tag{2.91}$$

a useful symmetry relation holds for the reservoir correlation functions given by

$$D^*_{\nu_1\nu_2\nu_3\nu_4}(t) = D_{\nu_2\nu_1\nu_4\nu_3}(-t). \tag{2.92}$$

Using these relations eq. (2.88) can be brought into the following more practical form

$$\begin{aligned}
\partial_\tau \langle A(t+\tau)B(t)\rangle &= i\hbar^{-1}\langle\{[H_\mathrm{S},A]\}(t+\tau)B(t)\rangle \\
&+ \sum_{\nu_1\nu_2\nu_3\nu_4} \hbar^{-2}\int_0^\tau dt' \Big[D^*_{\nu_4\nu_3\nu_2\nu_1}(t')\,\langle\{\tilde{P}_{\nu_1\nu_2}(-t')[A,P_{\nu_3\nu_4}]\}(t+\tau)B(t)\rangle \\
&\qquad + D_{\nu_3\nu_4\nu_1\nu_2}(t')\,\langle\{[P_{\nu_3\nu_4},A]\tilde{P}_{\nu_1\nu_2}(-t')\}(t+\tau)B(t)\rangle\Big] \\
&+ \sum_{\nu_1\nu_2\nu_3\nu_4} \hbar^{-2}\int_\tau^{t+\tau} dt' \Big[D^*_{\nu_4\nu_3\nu_2\nu_1}(t')\,\langle\{\tilde{P}_{\nu_1\nu_2}(-t')[A,P_{\nu_3\nu_4}]\}(t+\tau)B(t)\rangle \\
&\qquad + D_{\nu_3\nu_4\nu_1\nu_2}(t')\,\langle\{[P_{\nu_3\nu_4},A]\}(t+\tau)\{B\tilde{P}_{\nu_1\nu_2}(-[t'-\tau])\}(t)\rangle\Big]\,. \qquad (2.93)
\end{aligned}$$

To obtain this EOM the second order Born approximation has been explicitly applied and several the integration variables have been transformed. The second order Born approximation is applied a bit differently in the Heisenberg picture compared to the standard Schrödinger picture derivation of the RDM done in section 2.2.1. We therefore give an example of how to apply it in an expectation value containing both system and reservoir operators. Consider the following

$$\begin{aligned}
&\langle\{\tilde{R}_1(t-t')\tilde{P}_1(t-t')R_2P_2\}(t')\rangle \\
&\qquad = \mathrm{Tr}_\mathrm{SR}\Big[\Big\{\tilde{R}_1(t-t')\tilde{P}_1(t-t')R_2P_2\Big\}(t')\chi(0)\Big] \\
&\qquad = \mathrm{Tr}_\mathrm{SR}\Big[\{\tilde{R}_1(t-t')R_2\}(t')\{\tilde{P}_1(t-t')P_2\}(t')\chi(0)\Big] \\
&\qquad = \langle\{\tilde{R}_1(t-t')R_2\}(t')\{\tilde{P}_1(t-t')P_2\}(t')\rangle \\
&\qquad \approx \langle\{\tilde{R}_1(t-t')R_2\}(t')\rangle\,\langle\{\tilde{P}_1(t-t')P_2\}(t')\rangle \\
&\qquad \approx \langle\tilde{R}_1(t-t')R_2\rangle\,\langle\{\tilde{P}_1(t-t')P_2\}(t')\rangle\,.
\end{aligned}$$

In the first three lines a simple reorganization is performed, grouping the operators according whether they belong to the system or reservoir. In line four we factorize the expectation value into a system and reservoir correlation function, which corresponds to the second order Born approximation. Finally, in the last line the reservoir correlation function is assumed to only be governed by the free Hamiltonian of the reservoir, H_R, hence the properties of the reservoir do not change during the time-evolution.

From eq. (2.93) it is easy to see that the QRT holds for a Markovian reservoir, in which case the reservoir correlation functions are proportional to delta functions, $D_{\nu_3\nu_4\nu_1\nu_2}(t') \propto \delta(t')$. The terms deviating from the QRT are all contained in the memory integral extending from $t'=\tau$ to $t'=\tau+t$ on the last two lines, and will therefore all vanish for a delta correlated reservoir only contributing at $t'=0$. Another interesting case where the QRT also holds is whenever the limit $\tau\to\infty$ can be taken in the time-dependent rates contained in eq. (2.93), for which the correctional terms are seen to vanish due to the decay of the reservoir correlation function. We note that this limit does not correspond to the Markovian limit where $D_{\nu_3\nu_4\nu_1\nu_2}(t') \propto \delta(t')$ is assumed, see the discussions in sections 2.2.3, 3.2.4 and 3.2.6.

2.4 Semiconductor models

The philosophy toward physical modeling in this thesis is well captured by the famous quote by Albert Einstein: “Everything should be made as simple as possible, but no simpler.”. Our goal is to study complicated physical effects and focus on qualitative physical insights, using the simplest possible ingredients, rather than obtaining a very accurate quantitative understanding, using complicated ingredients. For this reason we employ simple theoretical descriptions for the different physical constituents in our system, namely the QD, the optical cavity, and the phonon systems.

Below we will briefly discuss the individual components and refer the reader to more comprehensive texts providing a thorough treatment.

2.4.1 Self-assembled quantum dots

The QDs we will be dealing with are known as self-assembled QDs, due to the fabrication technique, which is the Stranski-Krastanow technique [23]. The QDs are grown using two different semiconductor materials, typically GaAs and InAs, which have a slight mismatch in lattice constant. The procedure is as follows: A thin layer of InAs is placed on a surface of GaAs, where the lattice mismatch causes stress and strain to build in the interface between the two materials. To release the tension, and thereby lower the energy of the system, small islands of InAs randomly form on the so-called wetting layer of GaAs, see fig. 2.2(left) for an illustration of this stage in the process. Finally, the newly formed QDs are capped by another layer of GaAs completely encapsulating the InAs QDs in a bulk of GaAs.

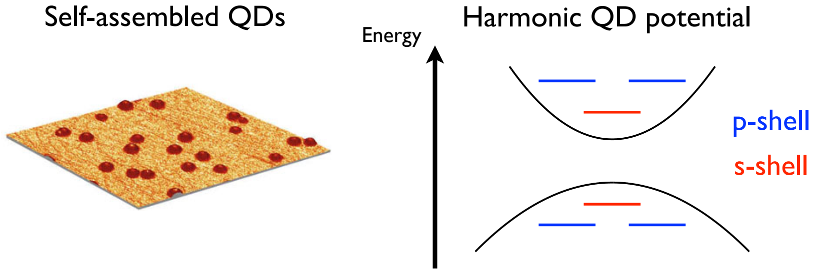

Figure 2.2: (left) Uncapped self-assembled QDs on a wetting layer [source: www.fotonik.dtu.dk] and (right) schematic illustration of a harmonic confinement potential used in the modeling and indication of the bound s- and p-shells on both bands.

As InAs has a lower bandgap energy than GaAs, the carriers moving in the lattice will see a potential well inside the QDs and localized carrier states will form in the spatial region near the InAs QD. An excellent approximation to the confining potential has been found to be provided by a harmonic oscillator potential in the in-plane directions [24], which yields analytical carrier wavefunctions greatly simplifying the modeling. The specific confinement potential model for the growth direction is less critical compared to the in-plane directions. This is due to the small length scale in this direction and corresponding large energy separation. This causes the carriers to remain in the lowest energy state in the growth direction and the important dynamics takes place in the in-plane directions. Typical choices of confinement potential models could be an infinite potential well or a harmonic potential with a smaller localization length than in the in-plane directions. The resulting energy eigenstates are illustrated schematically in fig. 2.2(right).

2.4.2 Optical microcavities

The control of the electromagnetic degrees of freedom is performed using optical microcavities. These are microfabricated structures where the smallest feature sizes can be accurately controlled, owing to the relatively long wavelength of light in the optical regime, something which is not possible for the electronic degrees of freedom due to the much smaller wavelength of electrons. This level of control entails the ability, to a very high degree, to engineer the properties of light confined in these structures.

In all-solid-state cQED the most common cavity designs are photonic crystal and micropillar cavities, see fig. 2.3. Both rely on multiple reflections of light in order to provide confinement. In the micropillar cavity, multiple Bragg reflectors surround a central region, where light created in this region undergoes many reflections before escaping, effectively creating a localization of light. The same mechanism occurs in the photonic crystal cavity, however here the reflections arise due to a periodic arrangement of holes in the material slap.

Both designs give rise to so-called photonic bandgaps, where only light with certain frequencies is allowed to propagate. The cavity typically appears as a Lorentzian lineshape within the bandgap, with a width reflecting the photon lifetime in the cavity. To model this situation we employ the so-called quasi-mode description [25], where we assign a finite lifetime to a single optical mode, typically using an appropriate Lindblad decay term. For a more extensive review of different cavity designs we refer the reader to [26].

2.4.3 Phonons

The study of vibrations of the atomic lattice comprising semiconductor crystals is standard textbook material [27]. In compound semiconductors like GaAs several modes of vibration exists, which are named according to frequency range and the nature of the vibration of the atoms within the atomic unit cell. The branches which exists for GaAs are shown in fig. 2.4, near the Γ point in $\boldsymbol{k}$-space. The acoustical branches are characterized by a linear dispersion near $k \approx 0$, in contrast to the optical branches which have a finite energy even at $k = 0$. A longitudinal mode refers to the fact that the atoms oscillates parallel to the propagation direction, given by the $\boldsymbol{k}$ vector, whereas the transverse modes oscillate perpendicular to the propagation direction.

The behavior discussed above assumes that we are dealing only with bulk modes of the system, which are assumed to isotropic in $\boldsymbol{k}$-space around the Γ

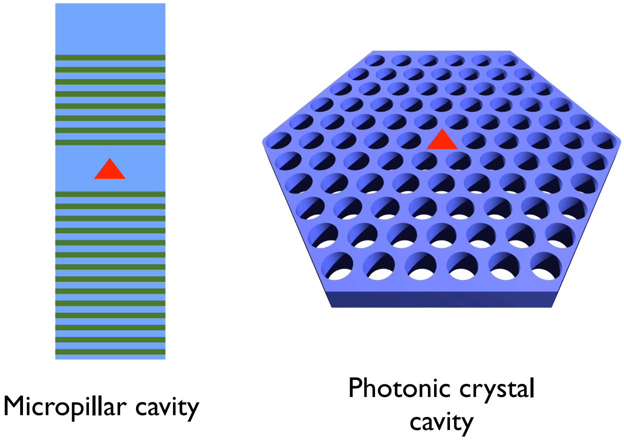

Figure 2.3: Schematic illustrations of different optical microcavity designs with an embedded QD (red triangle).

point. However, it is clear that a highly heterogeneous system consisting of self-assembled QDs arising in the interface between GaAs and InAs and surfaces associated with fabricating the optical cavity, gives rise to more than mere bulk phonon modes. Studies have however shown that for typical cQED structures the most important modes to include are bulk modes [28, 29, 30, 31], hence we proceed only including these in the further modeling.

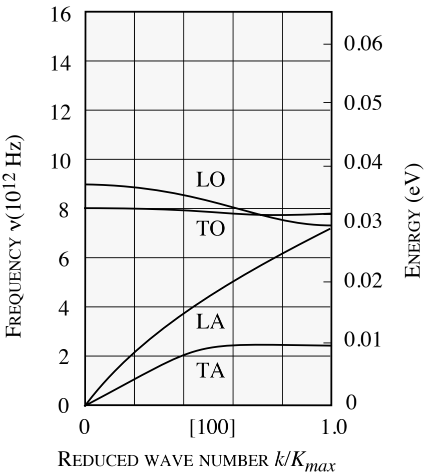

Figure 2.4: Phonon dispersion diagram for GaAs [27], where L=longitudinal, T=tranversal, O=optical, and A=acoustical.

2.4.4 Interaction mechanisms

The subsystems described above, all interact at some level via various physical mechanisms, where we will briefly discuss the most important in this section.

We start by considering the interaction between the electron confined in the QD and the photons confined in the cavity. The fundamental interaction Hamiltonian between electrons and photons may be derived at various levels of sophistication [32], however, the relevant Hamiltonian for most experiments in all-solid-state cQED is of the form

$$H_{\mathrm{el-phot}} = \sum_{ij} \sum_{m} \hbar g_{ij}^{m} (a_m^\dagger + a_m) c_i^\dagger c_j, \tag{2.94}$$

where $c_i^\dagger$, c_j are fermionic operators for the electronic states, $a_m^\dagger$, a_m are bosonic operators for the modes in the cavity, and g_{ij}^m is the interaction matrix element. If we assume that we only consider transitions where the photon energy, $\hbar\omega_m$, is much larger than the corresponding matrix element, $\hbar g_{ij}^m$, we may safely apply the so-called rotating wave approximation where highly non-resonant contributions to the interaction Hamiltonian are neglected. Further assuming that we only consider a single quasi-mode of the cavity and only a single two-level electronic system with a ground (g) and an excited state (e), we obtain

$$H_{\mathrm{el-phot}} = \hbar g (a^\dagger c_{\mathrm{g}}^\dagger c_{\mathrm{e}} + a c_{\mathrm{e}}^\dagger c_{\mathrm{g}}), \tag{2.95}$$

which will be used throughout this thesis.

Of the four phonon branches present in GaAs, fig. 2.4, only the interaction with the longitudinal optical (LO) and longitudinal acoustic (LA) branches is significant for our system [33]. If we consider fig. 2.4 we notice that LO phonons have energies in the vicinity of 35 meV in the long wavelength limit. This energy is much larger than any other we will be considering, hence we do not expect LO phonons to be important and they will henceforth be neglected, which leaves us with the LA phonons.

The main interaction mechanism between electrons and LA phonons is through the deformation potential interaction. We will not go into the details of this interaction, but merely sketch the physics involved and refer the reader to the literature for more details [34]. The displacements of the crystal lattice caused by the phonons induce strain fields, which in turn introduce a local energy shift in the band structure, which is the physical origin of the deformation potential (DP) interaction. The energy shift can be written as

$$\Delta E_{\mathrm{band}} = E_{\mathrm{band}}^{\mathrm{un-strained}} - E_{\mathrm{band}}^{\mathrm{strained}}. \tag{2.96}$$

For small displacements we may write the energy shift as

$$\Delta E_{\mathrm{band}} = \left(\frac{dE_{\mathrm{band}}}{dV} \right) \Delta V, \tag{2.97}$$

where V is a volume element and ΔV is the change in the volume element due to the phonons. If we assume an isotropic medium, the relative change in the volume element is given by $\Delta V/V = \boldsymbol{\nabla}\cdot\boldsymbol{u}(\boldsymbol{r})$, where $\boldsymbol{u}(\boldsymbol{r})$ is the displacement field of the phonons. Inserting this into the above yields the DP interaction Hamiltonian

$$H_{\text{band}}^{\text{DP}} = D_{\text{band}}\boldsymbol{\nabla}\cdot\boldsymbol{u}(\boldsymbol{r}), \tag{2.98}$$

where the deformation potential constant is defined as $D_{\text{band}} = V\left(\frac{dE_{\text{band}}}{dV}\right)$. Converting this Hamiltonian into second quantization renders it in the form which will be applied in the rest of the thesis.

Recent years have seen an explosion in the field of cavity optomechanics [35], where the coupling between phonons and photons is the central interaction mechanism. This new and exciting field promises both practical applications as well as new ways of probing fundamental physics. The coupling between the light field in a photonic crystal cavity and the phonons localized within the same optical cavity has recently been demonstrated experimentally [31]. While the coupling was measurable by studying the noise properties of light emitted from the cavity, the strength of the phonon-photon coupling constant was found to be several orders of magnitude smaller than any other relevant coupling constant in the system, hence we will not consider any interactions of this nature.

2.5 Summary

In this chapter we have described the theoretical approaches and physical models we will be using in this thesis.

The main theoretical tool is the one-time reduced density matrix (RDM), which describes the dynamical properties of a small system interacting with a number of larger reservoirs. We have derived reservoir scattering terms based on the time-convolutionless (TCL) formalism which enables the inclusion non-Markovian effects arising from the reservoir interaction, due to a finite memory depth of the reservoir correlation functions. On the basis of the TCL approach we derived the famous Lindblad formalism, achieved by taking the limit where the reservoir correlation functions are delta functions in time, yielding a memory-less reservoir and hence the dynamics become Markovian. A discussion of various limits of the non-Markovian TCL was also provided, which clarified the subtle differences between the pure Markovian Lindblad theory and the long-time limit of the non-Markovian TCL.

We derived and discussed the celebrated Quantum Regression Theorem (QRT), which is the standard method for calculating multi-time correlation functions in quantum optics. We emphasize the Markovian approximation underlying the derivation of QRT, which is often not sufficiently clear in many treatments. Following recent publications [6, 7], we derived corrections to the QRT arising when dealing with non-Markovian reservoirs and discuss under which circumstances the Markovian QRT is expected to hold.

Finally, we discussed the effective physical models we use to describe a semiconductor cQED system, including the individual constituents and their mutual interactions.

Chapter 3

Quantum dot decay dynamics

In this chapter we investigate the influence of the electron-phonon interaction on QD decay dynamics in a semiconductor cQED system. The work is mainly motivated by a series of papers which experimentally demonstrate strong coupling between a single QD and a cavity [36, 37, 38]. In these papers it became clear that the standard cQED model, consisting of the Jaynes-Cummings model including losses, could not describe the experimental data in detail. An example of this deficit is most prominently displayed in the paper by Hennessy *et al.* [38], see fig. 3.1(a), where a coupling exists between the QD resonance, which was pumped through the wetting layer, and the cavity resonance, even through these were spectrally separated by several tens of cavity linewidths. From the standard model it is predicted that once the QD-cavity detuning, $\Delta = \omega_{\mathrm{QD}} - \omega_{\mathrm{cav}}$, exceeded the largest linewidth in the system, usually the cavity linewidth, the emission at the cavity resonance should drastically decrease. This was, however, not observed experimentally. For this reason the effect was often referred to as the non-resonant or far-off-resonance coupling mechanism. Early theoretical attempts [39, 40, 41] tried to remedy the situation by including a pure dephasing rate in the Jaynes-Cummings model, which, surprisingly, turned out to significantly increase the detuning range over which the QD and the cavity could couple. However, the pure dephasing model could not explain the non-resonant coupling over the experimentally observed spectral range and also lacked an underlying mechanism.

Eventually it was realized [2, 43, 44] that the very non-resonant coupling, $\hbar|\Delta| > 10$ meV, was dependent on the excitation energy and power of the QD and arose due to multi-excitons in the QD and their Coulomb-mediated correlations with carriers in the wetting layer. In the weak excitation regime, the spectrally very long-ranged couplings did not occur. However, here another non-resonant coupling appeared which seemed to be important for $\hbar|\Delta| < 5$ meV and depended on the sign of QD-cavity detuning at low temperatures, see fig. 3.1(b). Also, the QD decay curves reflect the behavior of the emission spectra, see insets in fig. 3.1(b). Acoustic phonons in the surrounding matrix

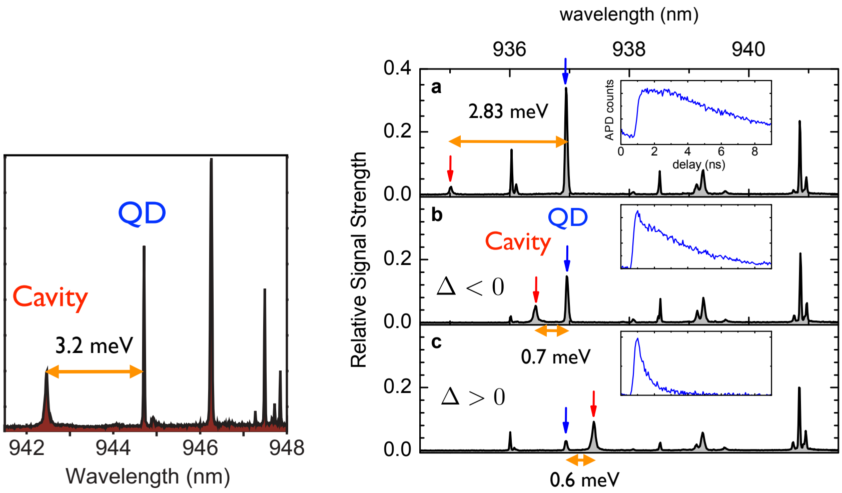

(a) Emission spectra recorded for non-weak excitation conditions and above-band pumping displaying the non-resonant coupling effect due to Coulomb-induced correlations. Reproduced from [38].

(b) As in fig. 3.1(a) but in the weak excitation regime, but for different QD-cavity detuning and with QD decay curves as insets. Reproduced from [42].

Figure 3.1: Experimental data showing the different regimes of the non-resonant coupling effect.

were quickly suggested as the underlying mechanism, which, at the time, was partly supported by semi-classical models [45, 46]. However, no full quantum model was available and detailed comparison between theory and experiment was not performed.

Here, we present a non-Markovian model of a cQED system coupled to phonons. We show agreement with experiment on both a qualitative and quantitative level for $\hbar|\Delta| < 5$ meV. Furthermore, a clear physical interpretation is given founded in a novel polariton-based picture, which emphasizes the quasi-particle nature of the coupled QD-cavity system. The theory reveals that the phonon interaction gives rise to a dramatically increased bandwidth of the QD-cavity interaction, that depends strongly on temperature. At low temperatures the phonons induce an asymmetry in the QD decay rate with respect to detuning, due to the absence of the thermally excited phonons available for absorption processes. For higher temperatures, the phonons are shown to cause a renormalization of the QD-cavity coupling strength to lower values, that in turn changes the criteria for obtaining strong coupling.

The results presented in this chapter are mainly based on [12, 47].

3.1 Model system

In this section we go through the model we use to describe the cQED system including the interaction with phonons. The system is illustrated schematically in fig. 3.2. We also devote a section to the so-called polaron transformation as this changes the representation of the system considerably.

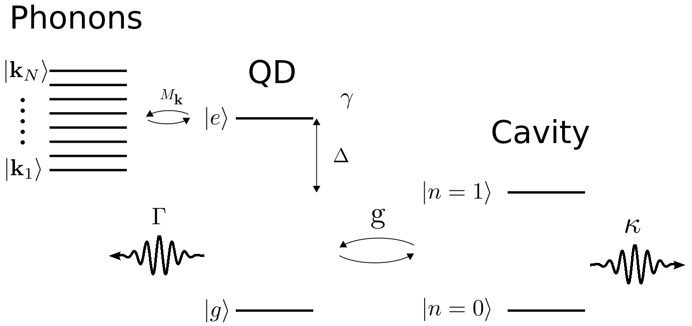

Figure 3.2: Schematic of the cavity QED system including the phonon interaction. The QD-cavity coupling strength is g and the QD-phonon interaction matrix elements are $M_{\boldsymbol{k}}$. The rates Γ and κ yield decay of the QD and cavity, respectively. Pure dephasing of the QD is included through γ and Δ is the QD-cavity detuning.

3.1.1 Cavity QED system

The part of the system consisting of the QD and cavity and their respective loss reservoirs will be introduced in this section. This part of the system can be represented by the Hamiltonian

$$H_{\mathrm{cQED}} = H_{\mathrm{s}} + H_{\gamma} + H_{\kappa} + H_{\Gamma}, \tag{3.1}$$

where H_{s} describes the QD-cavity system. The Hamiltonians H_{γ}, H_{κ}, and H_{Γ} describe various interactions with the environment which are described as Lindblad [8, 9] loss terms, which were discussed in general in section 2.2.2 and will be discussed in more detail below. The QD-cavity Hamiltonian, which is equivalent to the famous Jaynes-Cummings Hamiltonian, reads

$$H_{\mathrm{s}} = \hbar\omega_{\mathrm{g}} c_{\mathrm{g}}^{\dagger} c_{\mathrm{g}} + \hbar\omega_{\mathrm{e}} c_{\mathrm{e}}^{\dagger} c_{\mathrm{e}} + \hbar\omega_{\mathrm{cav}} a^{\dagger} a + \hbar g (a^{\dagger} c_{\mathrm{g}}^{\dagger} c_{\mathrm{e}} + c_{\mathrm{e}}^{\dagger} c_{\mathrm{g}} a), \tag{3.2}$$

where the usual rotating wave and dipole approximations have been applied, see the discussions in sections 2.4.1, 2.4.2 and 2.4.4 for more details. The energy of the ground (excited) QD state is $\hbar\omega_{\mathrm{g}}$ ($\hbar\omega_{\mathrm{e}}$) with corresponding fermionic operators $c_{\mathrm{g}}^{\dagger}, c_{\mathrm{g}}$ ($c_{\mathrm{e}}^{\dagger}, c_{\mathrm{e}}$), the energy of the cavity photon is $\hbar\omega_{\mathrm{cav}}$ with corresponding bosonic operators $a^{\dagger}, a$, and g is the interaction strength between the cavity photon and the electron in the QD. As we are only interested in describing the dynamics of the system on a single-photon level, it is advantageous to project the second quantized Hamiltonian presented above into a lower dimensional

Hilbert space. An appropriate basis to span this part of the total Hilbert space is the following: $\{|1\rangle = |\mathrm{e}, n=0\rangle, |2\rangle = |\mathrm{g}, n=1\rangle, |3\rangle = |\mathrm{g}, n=0\rangle\}$, where n refers to the number cavity photons in the given basis state. If we project onto this basis and further use a rotating frame we can write the QD-cavity system Hamiltonian as

$$H_{\mathrm{s}} = \hbar\Delta\sigma_{11} + \hbar g(\sigma_{12} + \sigma_{21}), \tag{3.3}$$

where $\Delta = \omega_{\mathrm{e}} - \omega_{\mathrm{g}} - \omega_{\mathrm{cav}} = \omega_{\mathrm{eg}} - \omega_{\mathrm{cav}}$ is the QD-cavity detuning and $\sigma_{pq} = |p\rangle\langle q|$ is the standard projection operator. The detailed steps are given in appendix B.

The remaining terms in H_{cQED} all give rise to different forms of losses, which we include through the Lindblad formalism. The Hamiltonian H_γ gives rise to pure dephasing processes, by a rate γ, for all transitions connected to the QD, whereas the Hamiltonians H_κ and H_Γ give rise to population decay from the excited cavity and QD, by a rates κ and Γ, respectively, see fig. 3.2. These rates are taken as parameters with values chosen to model experiment.

3.1.2 Phonons

The Hamiltonians involving phonons are given by

$$H_{0,\mathrm{ph}} = \sum_{\boldsymbol{k}} \hbar\omega_{\boldsymbol{k}} b^\dagger_{\boldsymbol{k}} b_{\boldsymbol{k}}, \tag{3.4}$$

$$H_{\mathrm{e-ph}} = \sum_{\boldsymbol{k}} \left(M^{\boldsymbol{k}}_{\mathrm{gg}} c^\dagger_{\mathrm{g}} c_{\mathrm{g}} + M^{\boldsymbol{k}}_{\mathrm{ee}} c^\dagger_{\mathrm{e}} c_{\mathrm{e}}\right)(b^\dagger_{-\boldsymbol{k}} + b_{\boldsymbol{k}}), \tag{3.5}$$

where $H_{0,\mathrm{ph}}$ describes the free phonons and $H_{\mathrm{e-ph}}$ describes the electron-phonon interaction, for more details see section 2.4.3 and section 2.4.4, respectively. It should be noticed that we assume bulk phonon modes [33, 48, 49, 28, 45, 50]. The LA phonon dispersion relation is assumed to be linear in the relevant energy range, hence $\omega_{\boldsymbol{k}} = c_{\mathrm{s}}|\boldsymbol{k}|$, with c_{s} being the speed of sound, and finally $b^\dagger_{\boldsymbol{k}}, b_{\boldsymbol{k}}$ are the bosonic operators for the phonons. The matrix element $M^{\boldsymbol{k}}_{\nu\nu}$ in the electron-phonon interaction is defined as [33, 48, 49, 45, 28]

$$M^{\boldsymbol{k}}_{\nu\nu} = \sqrt{\frac{\hbar k}{2dc_{\mathrm{s}}V}} D_\nu \int d\boldsymbol{r} |\phi_\nu(\boldsymbol{r})|^2 e^{-i\boldsymbol{k}\cdot\boldsymbol{r}}, \tag{3.6}$$

where d the is mass density, c_{s} is the speed of sound in the material, V is the phonon quantization volume, D_ν is the deformation potential for the band in question, and $\phi_\nu(\boldsymbol{r})$ is the electronic wavefunction for the state involved in the phonon process. We neglect the polar coupling to longitudinal optical (LO) phonons due to their large energies, ~ 37 meV in GaAs, compared to the energies involved in this model and we also neglect the piezoelectric coupling to LA phonons as it has been shown to have a small effect for the present system [33].

Unless otherwise stated, we model the QD wavefunctions, we consider harmonic confinement in the direction perpendicular to the growth direction[24] and infinite potentials in the growth direction. This implies ground state wavefunctions in both bands of the form

$$\phi_\nu(\boldsymbol{r}) = \frac{2^{1/2}}{\pi^{1/2} l_{xy,\nu} l_{\mathrm{eff,z}}^{1/2}} \exp[-(x^2+y^2)/(2l_{xy,\nu}^2)] \cos(\pi z/l_{\mathrm{eff,z}}),\ |z| \leq l_{\mathrm{eff,z}}/2 \tag{3.7}$$

where the confinement lengths $l_{xy,\nu}$ and $l_{\mathrm{eff,z}}$ can be chosen to model a specific system. We choose QD and phonon parameters suitable for typical InGaAs systems, see table 3.1.

description	symbol	value	unit	reference	note
material density	d	5370.0	kg m^{-3}	[33]	-
speed of sound	c_s	5110.0	m s^{-1}	[33]	-
deformation potential CB	D_e	-14.6	eV	[33]	-
deformation potential VB	D_g	-4.8	eV	[33]	-
QD in-plane confinement CB	$l_{xy,\mathrm{e}}$	6.18	nm	[51]	[a]
QD in-plane confinement VB	$l_{xy,\mathrm{g}}$	4.48	nm	[51]	[a]
QD z confinement	$l_{z,\mathrm{eff}}$	8.0	nm	[51]	[b]

Table 3.1: Phonon and QD parameters for typical InGaAs systems, where CB = conduction band and VB = valence band.

[a] The in-plane confinement lengths were determined by fitting to numerical effective mass simulations performed on realistic cone-shaped QDs [51].

[b] The z confinement length should be considered as an effective length, due to the fact that we employ infinite potential barriers in this direction, giving rise to an rather large effective height.

If we take advantage of the fact that we only consider a single electron, i.e. $c_\mathrm{g}^\dagger c_\mathrm{g} + c_\mathrm{e}^\dagger c_\mathrm{e} = 1$, and project onto the basis introduced above, we simply obtain

$$H_{\mathrm{e-ph}} = \sigma_{11} \sum_{\boldsymbol{k}} M^{\boldsymbol{k}} (b_{-\boldsymbol{k}}^\dagger + b_{\boldsymbol{k}}) = \sigma_{11} B, \tag{3.8}$$

where we introduced the effective matrix element

$$M^{\boldsymbol{k}} = M_{\mathrm{ee}}^{\boldsymbol{k}} - M_{\mathrm{gg}}^{\boldsymbol{k}}. \tag{3.9}$$

The details are presented in appendix B.

3.1.3 The polaron transformation

We start from the following Hamiltonian

$$H = \hbar\Delta\sigma_{11} + \hbar g(\sigma_{12} + \sigma_{21}) + \sigma_{11} \sum_{\boldsymbol{k}} M^{\boldsymbol{k}} (b_{-\boldsymbol{k}}^\dagger + b_{\boldsymbol{k}}) + \sum_{\boldsymbol{k}} \hbar\omega_{\boldsymbol{k}} b_{\boldsymbol{k}}^\dagger b_{\boldsymbol{k}}, \tag{3.10}$$

obtained by combining eqs. (3.3), (3.4) and (3.8). We then apply the so-called polaron transformation [52, 53, 54, 55, 56, 57], by which an operator O transforms in the following way

$$\bar{O} = e^{S} O e^{-S} \tag{3.11}$$

where

$$S = \sigma_{11} C, \quad C = \sum_{\boldsymbol{k}} \lambda_{\boldsymbol{k}} (b_{-\boldsymbol{k}}^{\dagger} - b_{\boldsymbol{k}}), \quad \lambda_{\boldsymbol{k}} = \frac{M^{\boldsymbol{k}}}{\hbar \omega_{\boldsymbol{k}}}. \tag{3.12}$$

The idea behind the transformation is to remove the term linear in the phonon operators in exchange for something which is easier to handle. Physically the transformation shifts the phonon modes according to the presence of the electron, determined by the operator σ_{11}. From the exponential nature of the transformation operator e^{S}, phonon processes are included to infinite order, even after standard approximations are applied. This has the consequence that multi-phonon effects are easily included in the theory, allowing for the description of experiments at high temperatures. While performing the polaron transformation we omit the contributions to the Hamiltonian giving rise to the Lindblad decay terms. Even though these Hamiltonians might not be invariant under the polaron transformation, the fact that the corresponding reservoirs are assumed to be memory-less or delta correlated in time, has the consequence that the polaron transformation has no effect on the resulting decay terms. For a detailed exemplification see appendix C. The Hamiltonian in the polaron frame becomes

$$\bar{H} = \bar{H}_{\mathrm{s}'} + \bar{H}_{\mathrm{s}'-\mathrm{ph}'} + H_{0,\mathrm{ph}}, \tag{3.13}$$

where we use the bar, $O \to \bar{O}$, to signify the transformed frame. We have

$$\bar{H}_{\mathrm{s}'} = \hbar \Delta \sigma_{11} + \hbar g \left\langle X \right\rangle (\sigma_{12} + \sigma_{21}), \tag{3.14a}$$

$$\bar{H}_{\mathrm{s}'-\mathrm{ph}'} = \hbar g (\sigma_{12} \delta X_{+} + \sigma_{21} \delta X_{-}), \tag{3.14b}$$

$$H_{0,\mathrm{ph}} = \sum_{\boldsymbol{k}} \hbar \omega_{\mathrm{k}} b_{\mathrm{k}}^{\dagger} b_{\mathrm{k}}, \tag{3.14c}$$

it should be noted that a constant energy shift induced by the phonons has been included in the QD-cavity detuning Δ, see eq. (C.8). Also, new phonon related operators have been introduced

$$\delta X_{\pm} = X_{\pm} - \left\langle X \right\rangle, \tag{3.15}$$

$$X_{\pm} = e^{\pm C}, \tag{3.16}$$

$$\left\langle X \right\rangle = \left\langle X_{\pm} \right\rangle, \tag{3.17}$$

where the brackets denote the expectation with respect to the thermal density matrix for the phonons, more precisely $\langle \cdots \rangle = \mathrm{Tr}_{\mathrm{ph}} \left\{ \rho_{\mathrm{ph},0} \cdots \right\}$. The detailed derivation can be found in appendix C and various relevant properties of the operators $X_{\pm}$ are described in appendix E. Due to the polaron transformation the division of the total Hamiltonian into a QD-cavity system part and a phonon part is no longer possible. Indeed, the new system Hamiltonian, $\bar{H}_{\mathrm{s}'}$, contains the phonon quantity $\langle X \rangle$ which is seen to renormalize the light-matter coupling strength g. It should also be noted that defining the new system Hamiltonian in this way, we include photon processes to infinite order as well as respecting the detailed balance condition [58]. From the expression for $\langle X \rangle$, see eq. (E.14), it is obvious that $0 < \langle X \rangle \leq 1$. The interaction with phonons will always decrease the effective light-matter coupling strength as a consequence of this, however the effective bandwidth of the QD increases due to phonon-assisted processes. The new interaction Hamiltonian, $\bar{H}_{\mathrm{s}'-\mathrm{ph}'}$, contains the phonon fluctuation operators $\delta X_{\pm}$, describing fluctuations of the phonon bath around its equilibrium value, as well as the light-matter coupling strength g.

3.2 Equations of motion

In this section we present the EOM employed for analyzing the system, described by the Hamiltonians of the previous section.

3.2.1 Time-convolutionless approach

Our basic approach is to set up an EOM for the RDM of the QD-cavity system, where the phonon degrees of freedom have been traced out. This is a standard technique [11, 8, 9] in which the effect of the reservoir enters through various scattering terms in theEOM for the RDM. These scattering terms can be derived in two forms. In the first, known as the Nakajima-Zwanzig projection operator technique [9], the resulting EOM have memory: such that the present state of the system depends on the past of the system. In the second, known as the time-convolutionless [9], the EOM do not have memory and are therefore time-local, however, one gets time-dependent scattering rates. Both of these approaches yield, without further approximations, an exact and non-Markovian description of the dynamics.

In this paper we employ the TCL up to second order in the perturbation for the following two reasons; The first and most important is based on the observation that in the limit where the light-matter coupling tends to zero, our model reduces to the so-called independent boson model [10]. This famous model is known to be exactly solvable using a number of methods, one being the second order TCL [59]. Even though the present model can not be solved exactly using the second order TCL, we expect the result to be more accurate compared to that obtained using the method involving memory integrals, as this does not result in the exact solution to second order for $g \rightarrow 0$. Other studies have also shown the TCL to be superior to the corresponding equation with memory [11]. The second reason is purely practical, as it is more straightforward to solve time-local equations compared to equations that containing memory integrals

The EOM arising from the TCL may be derived in a completely general framework [9], however we follow a less rigorous approach in deriving the TCL and present the resulting formulas in section 2.2.1.

3.2.2 Phenomenological losses

As mentioned in section 3.1.1, we also include interactions with other reservoirs than phonons to simulate a real system with losses. These are included within the Lindblad formalism, see section 2.2.2, where terms of the form

$$L_\gamma \{O\} \rho(t) = -\frac{\gamma}{2} \left[O^\dagger O \rho(t) + \rho(t) O^\dagger O - 2O\rho(t)O^\dagger \right], \tag{3.18}$$

are added to the EOM for $\rho(t)$, where $\rho(t) = \mathrm{Tr}_{\mathrm{ph}} \{\chi(t)\}$ is the RDM for the QD-cavity system, $\chi(t)$ is the density matrix for the total system, and $\mathrm{Tr}_{\mathrm{ph}} \{\cdots\}$ denotes the trace operation with respect to the phonon degrees of freedom. The above formula yields decay occurring at a rate γ on the transition determined by the operator O and is the zero temperature limit, $n = 0$, of eq. (2.55).

The decay of the photon in the cavity is modeled by including the Lindblad term $L_\kappa \{\sigma_{32}\} \rho(t)$, the decay of the excited QD is modeled by including $L_\Gamma \{\sigma_{31}\} \rho(t)$, and finally a Markovian pure dephasing rate is also included through $L_{2\gamma} \{\sigma_{11},\} \rho(t)$. For a reminder on the notation, we refer the reader to section 3.1.1 and fig. 3.2. The LA phonons we include explicitly, amongst other effects, give rise to a pure dephasing rate and as such it might seem redundant to introduce an additional pure dephasing channel. However, previous work has demonstrated that excited states for electrons and holes contribute to pure dephasing processes near the ground state transition energy, due to both LA [60, 61] and LO [62] phonon interactions. Also, including a finite lifetime of either LO and LA phonons, arising, e.g., from anharmonic effects [63], induces a contribution to the pure dephasing rate [64]. For simplicity we assume γ to be an independent parameter.

3.2.3 Notational remarks

The EOM we arrive at are all linear in the elements of the RDM. This fact makes it advantageous to formulate the EOM in the language of linear algebra. This can be achieved by mapping the RDM onto a vector form as follows

$$\begin{aligned} \langle \boldsymbol{\sigma}(t) \rangle = [&\langle \sigma_{11}(t) \rangle, \langle \sigma_{22}(t) \rangle, \langle \sigma_{12}(t) \rangle, \langle \sigma_{21}(t) \rangle, \\ &\langle \sigma_{23}(t) \rangle, \langle \sigma_{32}(t) \rangle, \langle \sigma_{13}(t) \rangle, \langle \sigma_{31}(t) \rangle]^T . \end{aligned} \tag{3.19}$$

Where $\langle \sigma_{qp}(t) \rangle = \mathrm{Tr}_{\mathrm{s}} \{\rho(t)\sigma_{qp}\} = \rho_{pq}(t)$, where $\mathrm{Tr}_{\mathrm{s}} \{\cdots\}$ denotes the trace with respect to the QD-cavity basis. The QD ground state population, i.e. $\langle \sigma_{33}(t) \rangle$, has been omitted as it does not matter for the dynamics we are going to consider and may be trivially obtained using population conservation. The matrix describing the coupling between different elements can be divided into three main contributions

$$\begin{aligned} \partial_t \langle \boldsymbol{\sigma}(t) \rangle &= [M_{\mathrm{coh}} + M_{\mathrm{Lindblad}} + M_{\mathrm{LA}}(t)] \langle \boldsymbol{\sigma}(t) \rangle \\ &= M(t) \langle \boldsymbol{\sigma}(t) \rangle , \end{aligned} \tag{3.20}$$

where M_{coh} describes terms originating from the coherent unitary evolution provided by the QD-cavity Hamiltonian, M_{Lindblad} describes terms from the

Lindblad operators, and finally $M_{\mathrm{LA}}(t)$ describes the, possibly time-dependent, scattering terms induced by the coupling to LA phonons.

As will be shown $M(t)$ can be written as two decoupled sub-matrices

$$M(t) = \begin{bmatrix} m^{(11)}(t) & 0 \\ 0 & m^{(22)}(t), \end{bmatrix} \tag{3.21}$$

where $m^{(11)}(t)$ couples the first four elements of $\langle \boldsymbol{\sigma}(t) \rangle$, $m^{(22)}(t)$ couples the last four, and all other elements are zero.

In the following two sections we will derive the EOM for the system using the TCL. We present the equations arising from the Hamiltonian without the polaron transformation, denoted the original frame, and with the polaron transformation, denoted the polaron frame. Employing the polaron transformed Hamiltonian is expected to yield more accurate results compared to the original Hamiltonian, especially for elevated temperatures. However, the equations resulting from the polaron transformation are also more complicated, due to the change of basis, are harder to interpret physically. On the other hand, the equations arising in the original frame are very simple and can be used to gain important insights into the physics in a straight-forward manner.

3.2.4 Original frame

In the original frame the total Hamiltonian without the Lindblad contributions is

$$H = H_{\mathrm{s}} + H_{0,\mathrm{ph}} + H_{\mathrm{e-ph}}, \tag{3.22}$$

where the individual contributions can be found in eqs. (3.3), (3.4) and (3.8), respectively. We choose $H_{\mathrm{e-ph}}$ as the interaction Hamiltonian in which we perform the perturbation expansion. With this identification only the electron-phonon interaction is treated approximately, which is expected to be a good approximation, whereas the electron-photon interaction is treated exactly and the theory is not limited to small values of the light-matter coupling strength g.

To write up the TCL EOM for the RDM we use eq. (2.35) and the time-local scattering term given in eq. (2.40) and finally add the Lindblad terms discussed in section 3.2.2 to get [12]

$$\begin{aligned} \partial_t \rho(t) = -i\hbar^{-1} \left[H_{\mathrm{s}}, \rho(t) \right] + S_{\mathrm{LA}}(t) \\ + \left(L_{\kappa} \{\sigma_{32}\} + L_{\Gamma} \{\sigma_{31}\} + L_{2\gamma} \{\sigma_{11}\} \right) \rho(t). \end{aligned} \tag{3.23}$$

Written in terms of the operator expectation values $\langle \sigma_{nm}(t) \rangle$, the populations in the QD-cavity system are obtained as follows: The cavity population is $\langle a^{\dagger}(t) a(t) \rangle = \langle \sigma_{22}(t) \rangle$ and the excited QD population $\langle c_{\mathrm{e}}^{\dagger}(t) c_{\mathrm{e}}(t) \rangle = \langle \sigma_{11}(t) \rangle$. The off-diagonal elements correspond to different polarizations or coherences in the QD-cavity system, where the relevant one for one-time dynamics is the so-called photon-assisted polarization $\langle \sigma_{12}(t) \rangle$. Remapping the RDM to vector form we get the following coupling matrices. The coherent terms are

$$m_{\mathrm{coh}}^{(11)} = \begin{bmatrix} 0 & 0 & -ig & ig \\ 0 & 0 & ig & -ig \\ -ig & ig & i\Delta & 0 \\ ig & -ig & 0 & -i\Delta \end{bmatrix}, \tag{3.24}$$

and

$$m_{\mathrm{coh}}^{(22)} = \begin{bmatrix} 0 & 0 & ig & 0 \\ 0 & 0 & 0 & -ig \\ ig & 0 & i\Delta & 0 \\ 0 & -ig & 0 & -i\Delta \end{bmatrix}, \tag{3.25}$$

and the Lindblad contributions

$$\begin{aligned} &\mathrm{diag}\left\{M_{\mathrm{Lindblad}}\right\} = \\ &\qquad -\frac{1}{2}\left[2\Gamma, 2\kappa, \Gamma+\kappa+2\gamma, \Gamma+\kappa+2\gamma, \kappa, \kappa, \Gamma+2\gamma, \Gamma+2\gamma\right], \end{aligned} \tag{3.26}$$

and finally the phonon induced terms are

$$m_{\mathrm{LA}}^{(11)}(t) = \begin{bmatrix} 0 & 0 & 0 & 0 \\ 0 & 0 & 0 & 0 \\ -i\mathcal{G}^{>}(t) & i\mathcal{G}^{<}(t) & -[\gamma_{12}(t) - i\Delta_{\mathrm{pol}}] & 0 \\ i[\mathcal{G}^{>}(t)]^{*} & -i[\mathcal{G}^{<}(t)]^{*} & 0 & -[\gamma_{12}^{*}(t) + i\Delta_{\mathrm{pol}}] \end{bmatrix}, \tag{3.27}$$

$$m_{\mathrm{LA}}^{(22)}(t) = \begin{bmatrix} 0 & 0 & 0 & 0 \\ 0 & 0 & 0 & 0 \\ i\mathcal{G}^{<}(t) & 0 & -[\gamma_{13}(t) - i\Delta_{\mathrm{pol}}] & 0 \\ 0 & -i[\mathcal{G}^{<}(t)]^{*} & 0 & -[\gamma_{13}^{*}(t) + i\Delta_{\mathrm{pol}}] \end{bmatrix}. \tag{3.28}$$

The elements of m_{LA} will defined below in eqs. (3.29), (3.30) and (3.32), but first we provide a brief discussion of the elements. If one disregards the phonon induced scattering terms these equations are the standard lossy Jaynes-Cummings model including pure dephasing, which has been studied intensely in recent years [39, 41, 40, 65, 66]. Let us start by discussing the terms in $m_{\mathrm{LA}}^{(11)}(t)$ in more detail, i.e., the quantities $\gamma_{12}(t)$ and $\mathcal{G}^{\gtrless}(t)$. If we compare the structure of the phonon scattering term eq. (3.27) with the non-phonon related terms in the coherent and Lindblad contributions to M, it becomes possible to provide a physical interpretation of the effects of phonons.

The rate $\gamma_{12}(t)$ multiplies the photon-assisted polarization and therefore the real part of $\gamma_{12}(t)$ will give pure dephasing of this specific polarization, whereas the imaginary part will give rise to an energy shift. The long-time limit of this energy shift has, however, been subtracted in the form of the quantity $\Delta_{\mathrm{pol}} = \mathrm{Im}\left\{\gamma_{12}(\infty)\right\}$, usually referred to as the polaron shift, to provide a consistent expansion in the electron-phonon interaction [67]. The subtraction has been performed everywhere the detuning, Δ, enters and results in an effective QD-cavity detuning close to zero, $\Delta \approx 0$, when phonons are included.

The quantities $\mathcal{G}^{\gtrless}(t)$ multiply the populations of the excited QD-cavity system in such a way that the real part of $\mathcal{G}^{\gtrless}(t)$ renormalizes the bare light-matter coupling strength g. However, in general $\mathrm{Re}\left[\mathcal{G}^{>}(t)\right] \neq \mathrm{Re}\left[\mathcal{G}^{<}(t)\right]$ and hence the renormalization is not an overall change in the value of g in the EOM for $\langle \sigma_{12}(t) \rangle$. The imaginary part of $\mathcal{G}^{\gtrless}(t)$ gives rise to an additional decay or gain of the polarization, depending on the sign of $\mathrm{Im}\left[\mathcal{G}^{\gtrless}(t)\right]$, if population is present in state 1 or 2. The dependence on the presence of excitation in the QD-cavity system makes this dephasing channel of a different nature than the pure dephasing normally induced by phonons which is well understood, see e.g. [33].

From the scattering term eq. (2.40) we get

$$\mathcal{G}^{\gtrless}(t) = i\hbar^{-2} \int_0^t dt' U_{11}^{*}(t') U_{21}(t') D^{\gtrless}(t'), \tag{3.29}$$

$$\begin{aligned} \gamma_{12}(t) &= \hbar^{-2} \int_0^t dt' [|U_{11}(t')|^2 D^{<}(t') - |U_{21}(t')|^2 D^{>}(t')] \\ &= \hbar^{-2} \int_0^t dt' [D^{<}(t') - |U_{21}(t')|^2 2\mathrm{Re}[D^{<}(t')]], \end{aligned} \tag{3.30}$$

$$\Delta_{\mathrm{pol}} = \mathrm{Im}\left\{\gamma_{12}(\infty)\right\}, \tag{3.31}$$

$$\begin{aligned} \gamma_{13}(t) &= \hbar^{-2} \int_0^t dt' |U_{11}(t')|^2 D^{<}(t') \\ &= \hbar^{-2} \int_0^t dt' [D^{<}(t') - |U_{21}(t')|^2 D^{<}(t')] \end{aligned} \tag{3.32}$$

where it has been used that both $D^{\gtrless}(t-t')$ and $U_{nm}(t-t')$ only depend on the difference between the two time arguments and further the initial time has been assumed to be zero. The ingredients are the phonon bath correlation functions

$$D^{\gtrless}(t) = \sum_{\boldsymbol{k}} |M^{\boldsymbol{k}}|^2 \left[n_{\boldsymbol{k}} e^{\pm i\omega_{\boldsymbol{k}} t} + (n_{\boldsymbol{k}} + 1)\, e^{\mp i\omega_{\boldsymbol{k}} t}\right] \tag{3.33}$$

$$= \sum_{\boldsymbol{k}} |M^{\boldsymbol{k}}|^2 \left[(2n_{\boldsymbol{k}} + 1)\cos(\omega_{\boldsymbol{k}} t) \mp i \sin(\omega_{\boldsymbol{k}} t)\right], \tag{3.34}$$

which are related to the phonon bath operators B in the following way

$$D^{\gtrless}(t-t') = \langle \tilde{B}(\pm[t-t'])B \rangle, \tag{3.35}$$

and $n_{\boldsymbol{k}}$ is the thermal occupation factor for the $\boldsymbol{k}$'th phonon mode defined in eq. (E.8). The matrix $U(t)$ is the time-evolution operator for the QD-cavity system which, due to the time-independence of H_{s} seen in eq. (3.3), can be given as a closed form expression

$$U(t) = \exp(-iH_{\mathrm{s}}t/\hbar). \tag{3.36}$$

The products of the elements of $U(t)$ occurring in eqs. (3.29) and (3.30) can be interpreted as propagators of the QD-cavity system governed by H_s, which is the pure lossless Jaynes-Cummings model. This is easily realized by writing the time-evolution of the density matrix for the pure Jaynes-Cummings model as

$$\rho^{\mathrm{JC}}(t) = U(t)\rho^{\mathrm{JC}}(0)U^\dagger(t). \tag{3.37}$$

If we assume that $\rho^{\mathrm{JC}}(0) = \sigma_{kk}$, i.e. the time-evolution starts with the excitation in a single state, we get

$$\rho^{\mathrm{JC}}_{nm}(t, \sigma_{kk}) = U_{nk}(t)U^\dagger_{km}(t) = U_{nk}(t)U^*_{mk}(t). \tag{3.38}$$

As the time-evolution of $\rho^{\mathrm{JC}}_{nm}(t, \sigma_{kk})$ contains the light-matter coupling, so do the Jaynes-Cummings propagators entering the phonon induced scattering terms. This leads to the interpretation that the phonons interact not with the bare electron, but rather with an electron-photon quasi-particle [12] often referred to as a polariton. In fact, if we approximate the $U(t)$ matrix in the phonon induced scattering terms with the time-evolution operator obtained for $g = 0$, i.e., the non-interacting QD-cavity system, then $U(t)$ becomes strictly diagonal [68]. As a consequence $\mathcal{G}^{\gtrless}(t) = 0$ and $\gamma_{12}(t) = \hbar^{-2}\int_0^t dt' D^<(t')$ and the phonon induced scattering terms would be independent on the properties of the QD-cavity system.

3.2.5 Polaron frame

In the RDM formalism we derive an EOM for

$$\rho(t) = \mathrm{Tr}_{\mathrm{ph}}\left\{\chi(t)\right\}, \tag{3.39}$$

which is useful for calculating expectation values provided that the operator of interest belongs to the system part of the Hilbert space. In this case we may perform the following operation

$$\begin{aligned} \langle O(t)\rangle &= \mathrm{Tr}_{\mathrm{s+ph}}\left\{\chi(t)O\right\} = \mathrm{Tr}_{\mathrm{s}}\left\{\mathrm{Tr}_{\mathrm{ph}}\left\{\chi(t)\right\}O\right\} && (3.40)\\ &= \mathrm{Tr}_{\mathrm{s}}\left\{\rho(t)O\right\}. && (3.41)\end{aligned}$$

If we now perform an arbitrary basis change operation given by the unitary operator T, where $T^\dagger T = T^{-1}T = I$, the expectation value of the operator O must of course not change, hence

$$\begin{aligned} \langle O(t)\rangle &= \mathrm{Tr}_{\mathrm{s+ph}}\left\{\chi(t)O\right\} && (3.42)\\ &= \mathrm{Tr}_{\mathrm{s+ph}}\left\{TT^\dagger\chi(t)TT^\dagger OTT^\dagger\right\} && (3.43)\\ &= \mathrm{Tr}_{\mathrm{s+ph}}\left\{\bar{\chi}(t)\bar{O}\right\}, && (3.44)\end{aligned}$$

where the bar signifies the operator in the new basis. In the new basis we may also define a RDM for the system as follows

$$\bar{\rho}(t) = \mathrm{Tr}_{\mathrm{ph}}\left\{\bar{\chi}(t)\right\}. \tag{3.45}$$

However, in order for this object to be useful for calculating physical expectation values we need to be able to perform the following operation

$$\langle O(t)\rangle = \mathrm{Tr}_{\mathrm{s+ph}}\left\{\bar{\chi}(t)\bar{O}\right\} = \mathrm{Tr}_{\mathrm{s}}\left\{\mathrm{Tr}_{\mathrm{ph}}\left\{\bar{\chi}(t)\right\}\bar{O}\right\} \tag{3.46}$$

$$= \mathrm{Tr}_{\mathrm{s}}\left\{\bar{\rho}(t)\bar{O}\right\}. \tag{3.47}$$

That is, the basis change should not entangle the system operator with the reservoir degrees of freedom or more formally $\bar{O} = \bar{o}_{\mathrm{s}} \otimes I_{\mathrm{ph}}$, I_{ph} being the identity operator in the phonon Hilbert space.

In the case of the polaron transformation, see eq. (3.11), all system projection operators are left invariant under the polaron transformation, i.e. $\bar{\sigma}_{nm} = \sigma_{nm}$, except for the off-diagonal operators: σ_{12}, σ_{13}, and their hermitian conjugates. This has the consequence, e.g., that the bare electron polarization $\langle c_{\mathrm{e}}^{\dagger}(t)c_{\mathrm{g}}(t)\rangle = \mathrm{Tr}_{\mathrm{s}}\left[\rho(t)\sigma_{13}\right]$, often used to calculate the linear optical susceptibility, cannot be determined directly within the polaron frame [52, 53]. Fortunately, all operators needed for our purposes are left invariant.

As the polaron transformed Hamiltonian derived in section 3.1.3 is expressed in terms of bare QD-cavity operators, the elements of the RDM that are projected out are with respect to the bare QD-cavity system operators and hence do not always correspond to the actual physical elements. To distinguish between expectation values calculated in the polaron and original frame, we introduce the following notation for the expectation values in the polaron frame

$$\langle O(t)\rangle_{\mathrm{p}} = \mathrm{Tr}_{\mathrm{s}}\left\{\bar{\rho}(t)O\right\}, \tag{3.48}$$

and as a consequence we get a new vector representation of the RDM in the polaron frame

$$\langle \boldsymbol{\sigma}(t)\rangle_{\mathrm{p}} = \Big[\langle\sigma_{11}(t)\rangle, \langle\sigma_{22}(t)\rangle, \langle\sigma_{12}(t)\rangle_{\mathrm{p}}, \langle\sigma_{21}(t)\rangle_{\mathrm{p}}, \\ \langle\sigma_{23}(t)\rangle, \langle\sigma_{32}(t)\rangle, \langle\sigma_{13}(t)\rangle_{\mathrm{p}}, \langle\sigma_{31}(t)\rangle_{\mathrm{p}}\Big]^{T}. \tag{3.49}$$

The polaron transformed Hamiltonian is given by

$$\bar{H} = \bar{H}_{\mathrm{s'}} + \bar{H}_{\mathrm{s'-ph'}} + H_{0,\mathrm{ph}}, \tag{3.50}$$

where the individual terms are defined in eq. (3.14). As in the previous section we set up the EOM for the RDM

$$\partial_t\bar{\rho}(t) = -i\hbar^{-1}\left[\bar{H}_{\mathrm{s'}}, \bar{\rho}(t)\right] + \bar{S}_{\mathrm{LA}}(t) \\ + \left(L_{\kappa}\{\sigma_{32}\} + L_{\Gamma}\{\sigma_{31}\} + L_{2\gamma}\{\sigma_{11}\}\right)\bar{\rho}(t), \tag{3.51}$$

where the LA scattering term in this case contains the interaction Hamiltonian $\bar{H}_{\mathrm{s'-ph'}}$. The coupling matrices in the polaron frame for the coherent and Lindblad terms are identical to those in the original frame, see eqs. (3.24) to (3.26), except that the replacement $g \to \langle X\rangle\, g$ should be performed in the coherent terms. The terms arising from the coupling to the LA phonons are

$$m_{\mathrm{LA}}^{(11)}(t) = \begin{bmatrix} -\Gamma_1(t) & +\Gamma_2(t) & -iG_2^*(t) & +iG_2(t) \\ +\Gamma_1(t) & -\Gamma_2(t) & +iG_2^*(t) & -iG_2(t) \\ +iG_1(t) & +iG_1(t) & -\gamma_1(t) & -iG_3^*(t) \\ -iG_1^*(t) & -iG_1^*(t) & +iG_3(t) & -\gamma_1^*(t) \end{bmatrix}, \tag{3.52}$$

and

$$m_{\mathrm{LA}}^{(22)}(t) = \begin{bmatrix} -\gamma_2(t) & 0 & iG_5(t) & 0 \\ 0 & -\gamma_2^*(t) & 0 & -iG_5^*(t) \\ iG_4(t) & 0 & -\gamma_3(t) & 0 \\ 0 & -iG_4^*(t) & 0 & -\gamma_3^*(t) \end{bmatrix}. \tag{3.53}$$

All elements are explicitly defined appendix F. As these expressions are in the polaron frame, we can not easily interpret the different terms as directly as in the original frame. However, we will still note a few differences and similarities. We now see a direct phonon induced lifetime renormalization of states 1 and 2 through Γ_1 and Γ_2, as well as several quantities playing a role similar to $\mathcal{G}^{\gtrless}(t)$ in the original frame, via the $G_n(t)$'s. Also, all polarizations now have a phonon induced pure dephasing rate given by the quantities $\gamma_n(t)$. All quantities are built from terms of the form

$$K_{nmkl}^{\pm}(t) = g^2 \int_0^t dt' \bar{U}_{n,m}(t') \bar{U}_{k,l}^*(t') B_{\pm}(t'), \tag{3.54}$$

where

$$\bar{U}(t) = \exp(-i\bar{H}_{\mathrm{s}'} t/\hbar), \tag{3.55}$$

is the time-evolution operator with respect to $\bar{H}_{\mathrm{s}'}$. The functions $B_{\pm}(t)$ are correlation functions for the polaron defined in eq. (E.15) and play a role similar to $D^{\gtrless}(t)$ in the original frame. The structure of $K_{nmkl}^{\pm}(t)$ is similar to that of the scattering terms in the original frame, but the interpretation is complicated by the fact that we are in the polaron frame.

3.2.6 Degree of non-Markovianity

The scatterings terms arising from the TCL are time-dependent giving rise to non-Markovian behavior. In the case of an initial excitation of the system, the duration of the time-dependence is set by the memory depth of the associated reservoir correlation function, $D^{\gtrless}(t)$ for the original and $B_{\pm}(t)$ for the polaron frame. This is evident from eqs. (3.29), (3.30), (3.32) and (3.54) as the time-evolution operator itself for either frame does not decay.

In fig. 3.3 we show examples of the various correlation functions for a range of relevant temperatures. The correlation function in the original frame, $D^{\gtrless}(t)$, has a temperature independent imaginary part (see eq. (3.33)), whereas the real part varies significantly with temperature. The amplitude is smallest and memory depth is largest for low temperatures (the memory depth is extracted from the normalized correlation function, not shown), where an increasing temperature leads to a larger amplitude and smaller memory depth. In the polaron frame the corresponding correlation functions are $B_{\pm}(t)$, for which both the real and imaginary part are temperature dependent. The amplitude and memory depth behave as in the original frame. For completeness we also show $\varphi(t)$ underlying $B_{\pm}(t)$, see eq. (E.26).

Above we discussed the dependence of the phonon correlation functions on temperature, however other parameters also influence the amplitude and

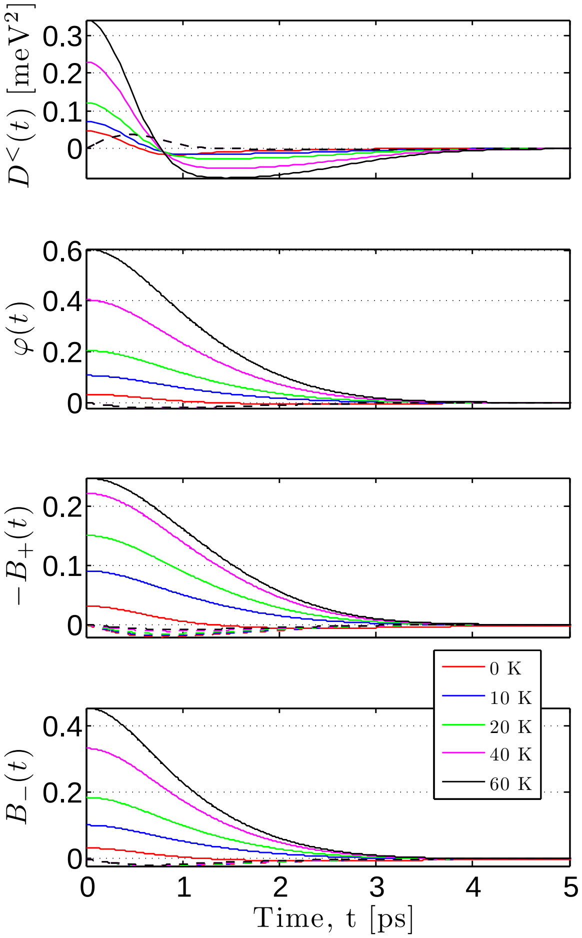

Figure 3.3: Illustrations of the various correlation functions for the phonon reservoir for fixed material parameters table 3.1 and a range of temperatures. Solid (dashed) lines are for the real (imaginary) part. $D^>(t)$ *can be as* $D^>(t) = [D^<(t)]^*$.

memory depth of the correlation functions. The spatial extent of the QD wavefunction turn out to be important. The phonon coupling matrix element, see eq. (3.6), is directly related to the spatial Fourier transform of the absolute square of the wavefunction of the relevant QD state. A small QD will have relatively wide spectrum in $\boldsymbol{k}$-space and thus couple to more phonon modes, causing the corresponding correlation function to decay faster. Conversely, a large QD will have a more narrow spectrum and couple to fewer phonon modes, resulting in a slower decay of the correlation function [33]. In the following, we keep the size of the QD fixed and will not investigate this further.

From fig. 3.3 we conclude that the time-dependence of the phonon correlation functions and therefore the TCL scattering terms only becomes important within the first few ps of the time evolution. For the time-dependence of the rates to have a significant effect on the dynamics, the RDM has to change significantly within the first few ps after the initial excitation, which is not the case for experimentally relevant parameters. For this reason, we may safely let $t \to \infty$ in all TCL scattering terms rendering them as constants, significantly simplifying the solution of the equations.

Taking the $t \to \infty$ limit in the TCL is sometimes referred to as performing a Markov approximation [11], whereas the non-Markovian regime is accessed for times smaller than the memory depth of the reservoir. However, in the case of a memory-less reservoir, taking the long time limit does not impose any further approximations. A memory-less reservoir is assumed in the derivation of the famous Lindblad result, see eq. (3.18), which is customary referred to as the Markovian limit in the field of cQED.

In our model the reservoir does have memory and we obtain qualitatively different results compared to a Markovian description of the phonon coupling within the Lindblad formalism, even though we take the long time limit in the TCL scattering terms. To distinguish the two qualitatively different descriptions, we will refer to the memory-less (Lindblad) case as the Markovian and the case including memory effects as non-Markovian, even though the $t \to \infty$ limit has been taken.

3.3 Results

In this section we present the results obtained from the theory described in the previous sections. In section 3.3.1 we provide a parameter investigation of QD decay dynamics obtained by numerically solving the EOMs in the time-domain and using the polaron frame. We choose the polaron frame to obtain the most accurate results. In section 3.3.2 we derive analytical expressions for the QD decay rate within both the original and polaron frame. We compared them numerically and discuss the insights that are obtained from their analytical forms.

3.3.1 Quantum dot decay dynamics

In fig. 3.4 we show a series of decay curves calculated within the polaron frame for an initially excited QD and compare the results for different signs and values of the detuning [42, 69, 12, 56]. The excitation could be achieved by means of an optical pulse, resonant with the photon-emitting $|g\rangle \leftrightarrow |e\rangle$ transition or higher states of the QD. The chosen parameter values ($g > \kappa$, Γ, γ) places this system well within the so-called strong coupling regime and the temperature has been set to 0 K to freeze out thermal excitation of phonons.

For the resonant case we observe a very fast decay, and clear Rabi oscillations indicating the strong coupling regime. For non-zero detuning we observe an asymmetry with respect to the sign of the detuning, which has been predicted theoretically [12] and observed experimentally [42, 69, 70]. The physical origin of the asymmetry is related to emission of phonons, stimulated by the

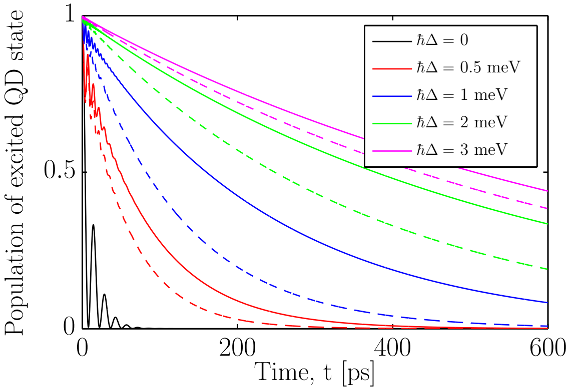

Figure 3.4: QD decay curves for an initially excited QD, calculated as $\sigma_{11}(t)$. The curves are for different signs of the detuning, solid (dashed) is for negative (positive) detuning, defined as $\Delta = \omega_{\mathrm{eg}} - \omega_{\mathrm{cav}}$. Parameters: $T = 0$ K, $\hbar g = 150$ μeV, $\hbar\kappa = 100$ μeV, $\Gamma = 1$ ns^{-1}, and $\hbar\gamma = 0$ μeV.

vacuum phonon field. Absorption of phonons is unlikely at very low temperatures, which could otherwise restore symmetry. The decay is fastest for positive detuning, as here the initially excited electron may emit a phonon to become resonant with the cavity and decay through it, whereas for negative detuning phonon absorption is needed. It is clearly seen that the asymmetry is strongest for intermediate detuning values, which may be explained by examining the interaction matrix element, see eq. (3.6). From the nature of the deformation potential interaction, the matrix element vanishes for small phonon energies becoming proportional to $\sqrt{\omega_k}$, while for large energies the form factor imposed by the finite QD wavefunction [71] causes the matrix element to decay. This gives rise to a natural maximum in the phonon matrix element, leading to the largest degree of asymmetry.

To more systematically quantify the dependence on detuning and the influence of finite temperature on the phonon induced asymmetry, we calculated the degree of asymmetry by taking the ratio between the slow QD lifetime for $\Delta < 0$, $\tau_{\Delta<0}$, and the faster lifetime obtained for $\Delta > 0$, $\tau_{\Delta>0}$. The results are presented in fig. 3.5 along with the absolute lifetime for both signs of the detuning. The lifetime is obtained by fitting a single exponential to the decay curve from the numerical solution of the model. In the situations where oscillatory behavior is present the fitted lifetime thus represents the decaying envelope of entire curve.

For the zero temperature case studied in fig. 3.4, we observe a degree of asymmetry of almost 2 near a detuning of approximately 1 meV. The value of the detuning for which the maximum is obtained is determined by the effective size of the QD through the form factor entering the phonon matrix element $M_{\boldsymbol{k}}$ [13]. For comparison, we also show the curve with no phonons in the model and it shows that for low temperatures the QD lifetime for $\Delta < 0$ is only very weakly influenced by the phonons. As the temperature is increased, the general

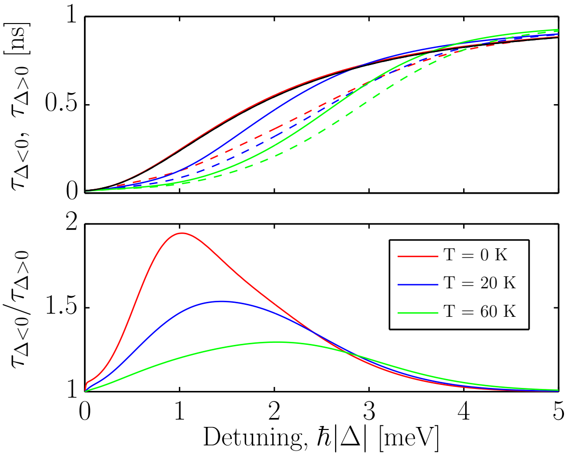

Figure 3.5: (Top) QD lifetimes for negative, $\tau_{\Delta<0}$*, (solid curve) and positive,* $\tau_{\Delta>0}$*, (dashed curve) detuning at three temperatures for a range detuning values. The black curve is with no phonons in the model. (Bottom) Degree of asymmetry quantified by the ratio between the QD lifetimes for opposite sign of detuning. Parameters are* $\hbar g = 150\ \mu eV$*,* $\hbar\kappa = 100\ \mu eV$*,* $\Gamma = 1\ ns^{-1}$*, and* $\hbar\gamma = 0\ \mu eV$*.*

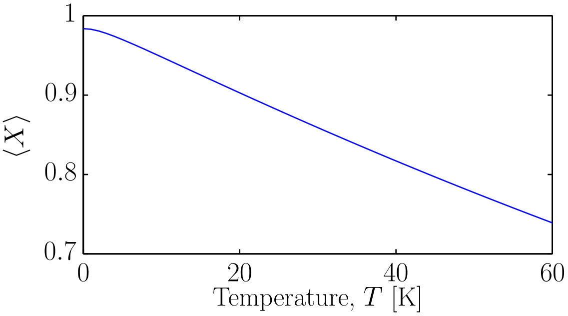

Figure 3.6: Dependence of $\langle X\rangle$*, see eq.* (E.14)*, on temperature.*

trend is that the degree of asymmetry decreases. Intriguingly, the QD is seen to decay more slowly at very large detuning as temperature is increased, even though this is basically outside the bandwidth of the phonons. We believe this to be due to the renormalization of g caused by $\langle X\rangle$, lowering the effective value of g, see fig. 3.6, where the temperature dependence of $\langle X\rangle$ is shown. The smaller asymmetry for higher temperatures is caused by the presence of thermally excited phonons, making it more probable for the electron to absorb a phonon and thereby becoming resonant with the cavity in the case when $\omega_{\text{cav}} > \omega_{\text{eg}}$, i.e., $\Delta < 0$.

To illustrate the behavior of the phonons at different temperatures we calculated the real part of the phonon correlation function eq. (3.33) in the frequency domain

$$\mathrm{Re}\left[D^{>}(\omega)\right] = \pi \sum_{\boldsymbol{k}} |M^{\boldsymbol{k}}|^2 [n_{\boldsymbol{k}} \delta(\omega + \omega_{\boldsymbol{k}}) + [n_{\boldsymbol{k}} + 1]\, \delta(\omega - \omega_{\boldsymbol{k}})], \tag{3.56}$$

where the Fourier transform is performed as

$$f(\omega) = \int_0^\infty dt e^{i(\omega + i0^+)t} f(t), \tag{3.57}$$

where 0^+ is a positive infinitesimal. The quantity $\mathrm{Re}\,[D^{>}(\omega)]$ gives information about the phonon modes interacting with the QD for a given temperature and can thus be considered as an effective phonon density. Also, it enters directly into the QD decay rate, as will be demonstrated in section 3.3.2.

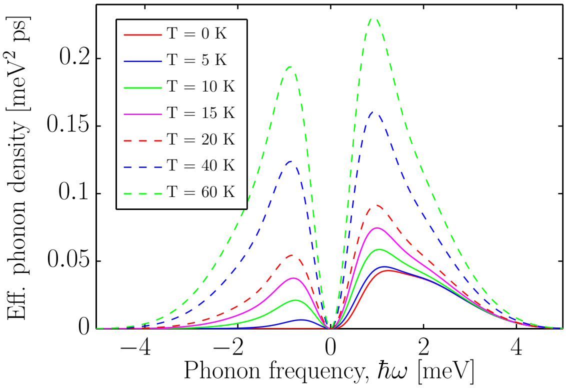

Figure 3.7: Effective phonon density calculated as $\mathrm{Re}\,[D^{>}(\omega)]$*, see eq.* (3.56)*, for a set of temperatures. The weak shoulder visible at low temperatures near* $\hbar\omega \sim 2$ *meV arises due to different localization lengths for the electron in the excited and ground states.*

In fig. 3.7 we show $\mathrm{Re}\,[D^{>}(\omega)]$ for a range of temperatures. For zero temperature, no phonons are available for absorption processes, corresponding to negative frequencies in the figure, while the vacuum phonon field reveals its presence through the non-zero density for positive energies. This explains why the asymmetry is largest for zero temperature, as illustrated in fig. 3.5. As the temperature is increased, more and more phonons are being thermally excited and become available for both absorption and stimulated emission processes. The strong asymmetry is no longer present in the effective phonon density, which correlates nicely with the observed behavior of the QD lifetimes.

We will now investigate the dependence of the phonon-induced asymmetry on the light-matter coupling strength g. In fig. 3.8(a) we show decay curves for a QD for both signs of the detuning and vary the light-matter coupling strength from very small values to larger values representing current state-of-the-art samples [42, 55]. The temperature is fixed at 0 K. The first observation

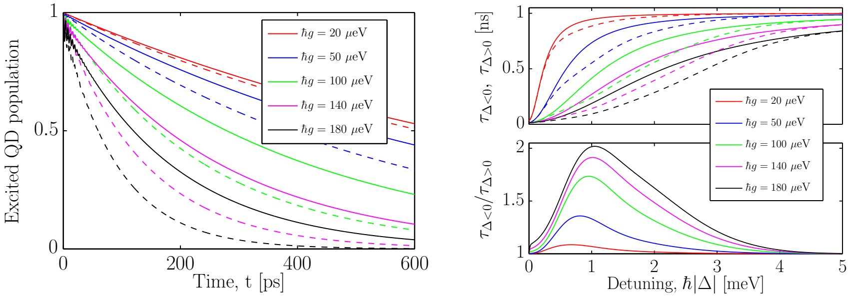

(a) QD decay curves for an initially excited QD. The curves are for different values of the light-matter coupling strength, g, while the solid (dashed) lines are for a detuning of -1 (+1) meV. Parameters: $T = 0$ K, $\hbar\kappa = 100$ μeV, $\Gamma = 1$ ns^{-1}, and $\hbar\gamma = 0$ μeV.

(b) Same as fig. 3.5, except here the light-matter coupling strength is varied through the differently colored series and $T = 0$ K.

Figure 3.8: Dependency on light-matter coupling strength.

is the decrease of lifetime for increasing g, consistent with the Purcell effect [72]. However, we also observe an increasing asymmetry between lifetimes for positive and negative detuning values as g is increased. This trend is seen more clearly in fig. 3.8(b) where we show the degree of asymmetry as a function of detuning, for varying light-matter coupling strength g. It is apparent that one may go from a situation of basically no asymmetry, obtained for a sample in the regime of weak / intermediate coupling strength [73], to more than a factor of 2 in ratio between lifetimes in state-of-the-art samples [42, 55, 74]. This behavior might seem surprising at first, since, as independently of the value of the detuning, the electron has to emit a photon in order to decay to the ground state, regardless of whether a phonon was emitted or absorbed. From this observation one would expect the degree of asymmetry to be independent of g, since the Purcell enhancement scales with g, independently of the detuning.

The degree of asymmetry is seen to approach unity in the limit of small light-matter coupling strength, where cavity-mediated effects play a less significant role for the QD decay dynamics. Indeed, in the limit of small g or large Δ, the dominant decay channel for the QD becomes the background decay rate, Γ, which includes, e.g., decay into radiation modes and non-radiative decay. To illustrate the effect of the background QD decay rate, we show in fig. 3.9 the degree of asymmetry as a function of Γ for a few typical values of the light-matter coupling strength, covering weak, intermediate, and strong coupling. For a typical weak coupling sample, $\hbar g = 30$ μeV, a noticeable asymmetry is only visible for very small Γ, corresponding to very good optical cavity structures. The asymmetry disappears as the phonon contributions become dominated by the background decay rate. On the other hand, for a sample well within the strong coupling regime, $\hbar g = 150$ μeV, a significant asymmetry should be observable for basically all values of the background decay rate, where now the cavity-mediated terms dominate the background decay of the QD.

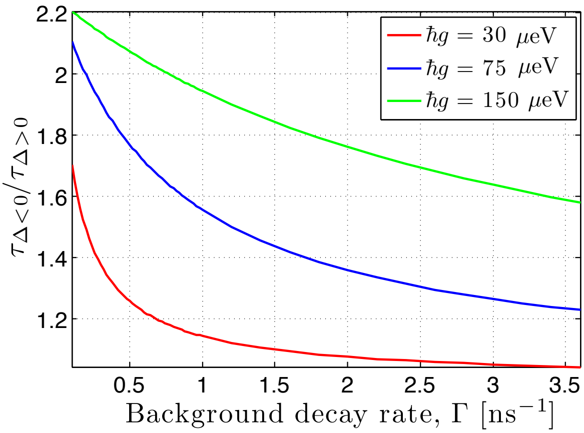

Figure 3.9: Degree of asymmetry as a function of QD background decay rate. The detuning is fixed at $\hbar|\Delta| = 1$ meV, while the light-matter coupling strength is varied. Other parameters are: $T = 0$ K, $\hbar\kappa = 100\ \mu$eV, and $\hbar\gamma = 0\ \mu$eV.

3.3.2 Approximate analytical expressions

While the results from the previous section are numerically exact solutions for the dynamics, more physical insight can be gained through approximate analytical expressions for the QD decay rates. In the limit of large detuning, $\Delta \gg g$, such expressions can be obtained in both the original and polaron frame. This is possible as we can adiabatically eliminate the involved polarizations, and the time evolution operator, $U(t)$, may be expanded to a low order in the quantity g/Δ, see appendix G for details.

In the original frame we obtain the following expression for the total QD decay rate

$$\Gamma_{\text{tot,orig}} = \Gamma + 2g^2 \frac{\gamma_{\text{tot}}}{\gamma_{\text{tot}}^2 + \Delta^2} \left\{ 1 + \frac{\hbar^{-2}}{\gamma_{\text{tot}}} \text{Re}\left[D^{>}(\omega = \Delta) \right] \right\}, \tag{3.58}$$

and for the polaron frame we obtain

$$\Gamma_{\text{tot,pol}} = \Gamma + 2[g\langle X\rangle]^2 \frac{\gamma_{\text{tot}}}{\gamma_{\text{tot}}^2 + \Delta^2} + 2g^2 \text{Re}\left[B_{-}(\omega = \Delta) \right], \tag{3.59}$$

where the total dephasing rate is defined as

$$\gamma_{\text{tot}} = \frac{1}{2}(\kappa + \Gamma) + \gamma. \tag{3.60}$$

In eqs. (3.58) and (3.59) the Fourier transform is performed as in eq. (3.57).

In figs. 3.10(a) and 3.10(b) we compare the QD lifetime ($\tau = 1/\Gamma_{\text{tot}}$) calculated from the approximate expressions with single exponential fits to the numerically exact solutions, for two typical sets of parameters. For all but very small detuning values, the approximate expressions compare very well to the corresponding numerical fits. The strong asymmetry at low temperatures,

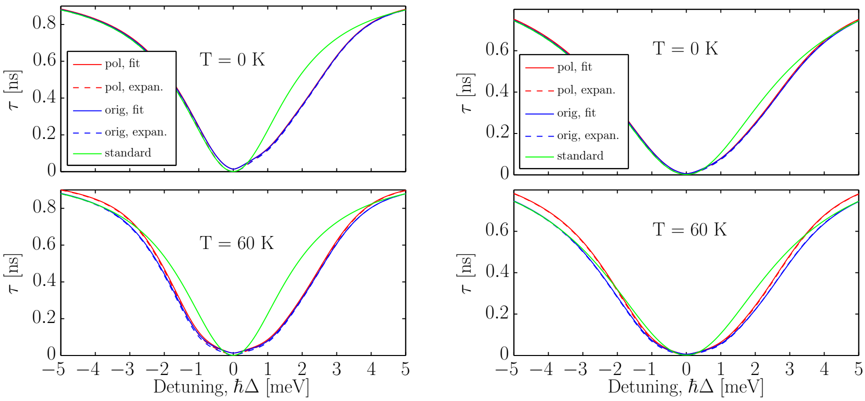

(a) Comparison of QD lifetimes obtained through the approximate rates (dashed curves) in the original (blue), eq. (3.58), and polaron frame (red), eq. (3.59), and a single exponential fit (solid curves) to the numerically exact solution. We also show the result for no phonons in the model (green). Parameters are: $\hbar\kappa = 100\ \mu$eV, $\hbar g = 150\ \mu$eV, $\Gamma = 1\ \text{ns}^{-1}$, and $\hbar\gamma = 0\ \mu$eV.

(b) As in fig. 3.10(a), except that $\hbar\kappa = 250\ \mu$eV.

Figure 3.10: Comparison between approximate analytical rates and fits to the numerical solutions.

as well as the more symmetric decay rates at elevated temperatures, are well captured by the approximate expressions. At high temperatures, we observe significant deviation between the results in the original and the polaron frame. This is expected as only the polaron frame takes into account multi-phonon effects that become increasingly important at elevated temperatures [56, 75].

The expression for the decay rate in the original frame, eq. (3.58), has a form very suitable for interpretation. In addition to the background QD decay rate Γ, there are two contributions. The first contribution accounts for the direct decay of the QD through the cavity by emission of a photon, with the total dephasing rate γ_{tot} including a Lindblad pure dephasing rate γ [76]. This gives rise to the familiar symmetric dependence on the detuning, see the green curve in figs. 3.10(a) and 3.10(b). However, the second contribution goes beyond the standard models of cQED by depending on the effective phonon density $\text{Re}[D^{>}(\omega = \Delta)]$ evaluated at the QD-cavity detuning, see eq. (3.56) and fig. 3.7. Thus, the phonon-assisted QD decay simultaneously depends on the cavity, through the Purcell rate prefactor, and on the availability of phonons that couple to the QD at the given QD-cavity detuning. Loosely, one can think of the second contribution as a product between the effective photon and phonon densities involved in the phonon-assisted QD decay.

Using the analytical expression of the QD decay rate in the original frame, eq. (3.58), we can provide a more physical transparent discussion of the depen-

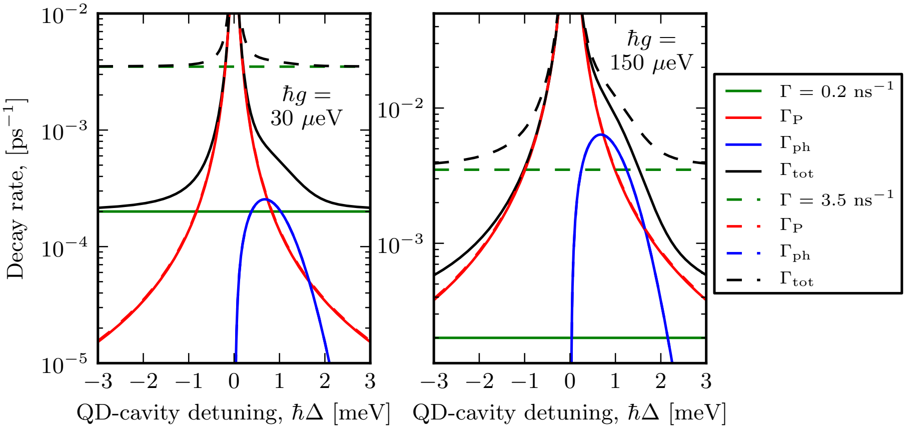

Figure 3.11: Contributions to the total QD decay rates given in eq. (3.61). *Note that for these figures a spherical QD model has been employed, using a harmonic confinement length of* 5 *nm. Parameters:* $\hbar\kappa = 100$ *μeV,* $\hbar\gamma = 0$ *μeV, and* $T = 0$ *K.*

dence on g and Γ of the degree of asymmetry discussed in figs. 3.8 and 3.9. We begin by formally dividing the total QD decay rate into the three contributions discussed above as

$$\Gamma_{\mathrm{tot}} = \Gamma + \Gamma_{\mathrm{P}} + \Gamma_{\mathrm{ph}}, \tag{3.61}$$

$$\Gamma_{\mathrm{P}} = 2g^2 \frac{\gamma_{\mathrm{tot}}}{\gamma_{\mathrm{tot}}^2 + \Delta^2}, \tag{3.62}$$

$$\Gamma_{\mathrm{ph}} = 2g^2 \frac{\hbar^{-2}}{\gamma_{\mathrm{tot}}^2 + \Delta^2} \mathrm{Re}\left[D^{>}(\omega = \Delta)\right], \tag{3.63}$$

where Γ is the background decay, Γ_{P} is the usual Purcell enhanced rate, and Γ_{ph} is the rate containing the phonon contribution and can be thought of as a phonon-assisted Purcell enhanced rate. With reference to fig. 3.9 we show in fig. 3.11 the three contributions to Γ_{tot} for two values, one small and one large, of Γ and g, as a function of detuning. For both values of the QD-cavity coupling we observe that neither the bare Purcell rate nor the phonon-assisted rate are affected much by going from the small background decay rate, $\Gamma = 0.2$ ns^{-1}, to the larger background rate, $\Gamma = 3.5$ ns^{-1}. Close to resonance, also the total decay rate appears rather independent of the magnitude of the background as it is completely dominated by the bare Purcell enhanced rate. However, this picture changes dramatically once we increase the detuning and the contribution from the bare Purcell rate becomes comparable to the two other contributions. In the case of the large background rate and small QD-cavity coupling, $\hbar g = 30$ μeV, the constant background dominates over the phonon-assisted rate, Γ_{ph}, and hardly any phonon-induced asymmetry is observed. Referring to fig. 3.9 this situation corresponds to a typical micropillar cavity in the weak coupling regime. If we now decrease the background rate to a lower value, corresponding to a typical photonic crystal cavity in the weak coupling regime [fig. 3.9], the background and the phonon-assisted contributions become comparable and the degree of asymmetry consequently rises. This illustrates that one may enter a regime, where phonon-induced spectral asymmetries become significant, by changing the background decay, a parameter which is often thought of as being of minor importance and with trivial physical implications. Increasing the QD-cavity coupling to values typically found in the strong coupling regime, $\hbar g = 150\ \mu\text{eV}$, we significantly increase both the bare and the phonon-assisted Purcell enhanced rates. For both values of the background rate, a clear asymmetry in the total QD decay rate is now observed, owing to the fact that the constant and symmetric background rate no longer masks the phonon-assisted decay processes.

The approximate expression in the polaron frame, see eq. (3.59), is not as straightforward to interpret as the expression in the original frame. The background decay Γ enters in the same fashion and we also observe a term similar to the one representing decay directly through the cavity in the original frame. However, in contrast, the quantity $\langle X \rangle$ only enters the polaron frame, where it plays the role of renormalizing the light-matter coupling strength to a smaller value. The dependence of $\langle X \rangle$ on temperature is shown in fig. 3.6, where it is seen that the renormalization can be quite significant. The last term involves the spectral properties of the phonons, through the Fourier transform of the correlation function $B_-(t)$

$$2g^2 \mathrm{Re}[B_-(\omega = \Delta)] = 2g^2 \langle X \rangle^2 \mathrm{Re}\left[\int_0^\infty dt e^{i\Delta t} \left\{ e^{\varphi(t)} - 1 \right\}\right], \tag{3.64}$$

where $\varphi(t)$ is defined in eq. (E.22). As $B_-(t)$ contains $\langle X \rangle^2$ as a factor, g is renormalized by $\langle X \rangle$ everywhere it occurs. This is not the case for other cQED models also employing the polaron transformation [56].

The remaining part involving the Fourier integral over $\exp[\varphi(t)] - 1$ is harder to interpret than the corresponding expression for $D^>(\omega)$ in the original frame. Even though $\varphi(t)$ and $D^>(t)$ appear rather similar, compare eq. (3.33) and eq. (E.22), $\mathrm{Re}[D^>(\omega)]$ more directly reflects the effective spectral features of the phonon reservoir. Also, in the original frame, $D^>(\omega)$ carries the familiar Lorentzian-style denominator of the cavity lineshape, which is missing in the polaron frame. Mathematically, the Lorentzian denominator appears in the expression since the phonon induced term enters via a polarization, whereas in the polaron frame, it enters directly as a lifetime. Despite the fact that they superficially look rather different, their numerical values compare very well, especially for low temperatures, as evidenced in figs. 3.10(a) and 3.10(b).

3.3.3 Renormalization of the strong coupling criteria

In sections 3.1.3 and 3.2.4 it was discussed how the interaction with phonons in general will renormalize the light-matter coupling constant toward smaller values. In this section we will investigate the effect of this renormalization on the possibility of reaching the strong coupling regime, using the EOM in the original frame.

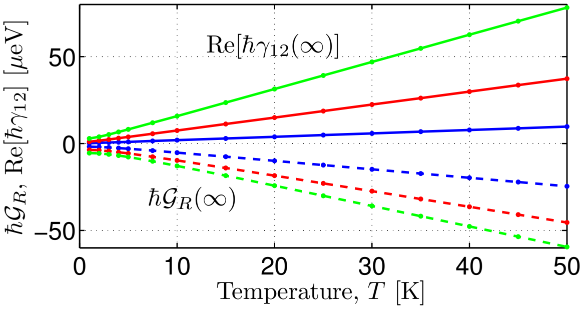

Figure 3.12: Real part of $\hbar\gamma_{12}(\infty)$ *(solid) and* $\hbar\mathcal{G}_R(\infty)$ *(dashed) for* $\hbar g = 50\ \text{(blue)}, 100\ \text{(red)}, 150\ \text{(green)}\ \mu eV$*. The imaginary parts are independent of temperature and much smaller than the real part and therefore not shown.*

We restrict ourselves to zero detuning. For this case

$$\mathcal{G}^{\gtrless}(t, \Delta = 0) = \mathcal{G}_R(t) \mp i\mathcal{G}_I(t), \tag{3.65}$$

where $\mathcal{G}_R(t)$ and $\mathcal{G}_I(t)$ are real functions. In fig. 3.12 we show the effect of temperature on the phonon induced rates $\mathcal{G}^{\gtrless}(\infty)$ and $\gamma_{12}(\infty)$, see eqs. (3.29) and (3.30), within the low temperature regime typically explored in cQED experiments. As expected, the pure dephasing rate increases with temperature. We also observe an increase as a function of the bare coupling strength g. $\mathcal{G}_R(\infty)$ also increases in magnitude with increasing temperature, but has a negative value. This leads to a lowering of the effective coupling strength entering the equation for the photon-assisted polarization $\langle\sigma_{12}(t)\rangle$ as temperature is increased. This can be realized by considering the EOM for $\langle\sigma_{12}(t)\rangle$, eq. (3.23), where we find the effective coupling to be $g_{\text{eff}}(\infty) = g - |\mathcal{G}_R(\infty)| < g$. The effective coupling strength thus depends significantly on temperature. We expect this dependence to have a detrimental effect on the possibility of reaching the strong coupling regime. To quantify this prediction we have investigated

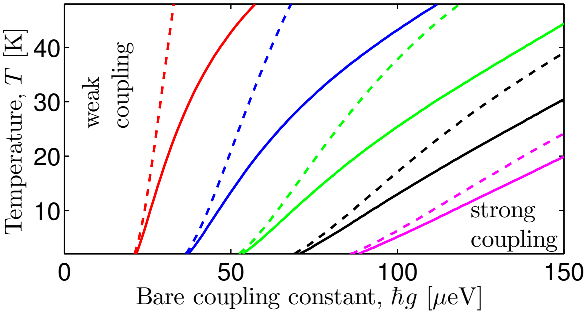

Figure 3.13: (color online). Parameter space showing the presence of strong or weak coupling for the full model (solid) and for $\mathcal{G}^{\gtrless}(t) = 0$ *(dashed), with* $\hbar\kappa =$ *75 (red), 125 (blue), 175 (green), 225 (black), 275 (magenta)* μeV*.*

the transition between the weak and strong coupling regime, while varying the most important parameters in the model, namely g, κ, and T. We define the weak coupling regime as the situation where the initially populated excited state of the QD decays monotonically toward zero. In fig. 3.13 we show the results both for the full model and for comparison the case where we have artificially put $\mathcal{G}^{\gtrless}(t) = 0$. This is done to emphasize the effect of the temperature induced renormalization of g, by allowing only the pure dephasing rate to be temperature dependent, as is common practice in phenomenological cQED models. As expected, we generally observe the presence of strong coupling in the system for large g and low T, with the parameter space of strong coupling becoming extended as we increase the quality of the cavity. Comparing the results of the full model with those where $\mathcal{G}^{\gtrless}(t) = 0$ we notice a strong effect of the renormalization of the bare coupling constant g. The parameter space where strong coupling is obtained is significantly decreased when including the renormalization of g. This result is relevant in the interpretation of experimental data, as state-of-the-art cQED models [40, 39, 41] do not include the renormalization effects contained in the functions $\mathcal{G}^{\gtrless}(t)$. These effects are of significant importance and therefore cQED models neglecting them can lead to misinterpretation of experimental data.

3.4 Comparison with experiment

Recently a series of measurements have been carried out in the Quantum Photonics Group headed by Prof. Peter Lodahl, performed jointly by Kristian Madsen and Asger Kreiner-Møller, where the detuning dependence of the QD decay rate was investigated in different cavity designs [3].

In fig. 3.14(a)(b) we show measured QD decay rates for a standard L3 cavity in photonic crystal membrane, while fig. 3.14(a)(c) reports decay rates measured for a QD interacting with an Anderson Localized (AL) mode in a disordered photonic crystal waveguide [77]. Both types of localized optical modes are illustrated in the inset of the respective figures. The large detuning range is comparable to the bandwidth of LA phonons, see fig. 3.7, for typical self-assembled QDs and has been achieved by a combination of temperature and gas deposition tuning.

Figure 3.14(a) also shows fits to the QD decay rate derived from the standard Jaynes-Cummings model, given by the first two terms in eq. (3.61), and the phonon model presented in section 3.2.4, all terms in eq. (3.61). We observe how the Jaynes-Cummings model nicely fits the measured decay rates for the AL cavity mode, however, for the L3 cavity the Jaynes-Cummings model is unable to explain the data at large detuning. See caption in fig. 3.14 for parameters extracted from the fitting procedure. If we include the effect of phonons for the L3 cavity, through eq. (3.61), we observe a surprisingly good agreement between theory and experiment at large detuning, especially taking into account the very small rates measured at large detuning. In fig. 3.14(b) we show the effective phonon density extracted from the experiment, along with the theoretical density calculated using the fitting parameters and we see a very good agreement between the two. We should note that to achieve this level

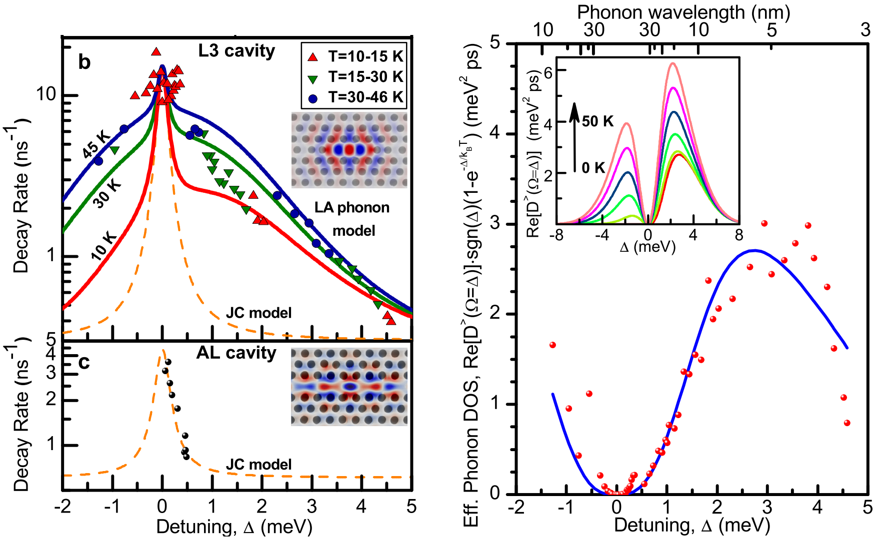

(a) Measured QD decay rates for (b) a L3 photonic crystal cavity and (c) an Anderson Localized mode in a disordered photonic crystal waveguide. Also shown are theoretical fits to different parts of eq. (3.61) and simulations of the localized modes are shown in the insets. Reproduced from [3].

(b) Experimentally extracted effective phonon density, see eq. (3.56), for the L3 cavity system where the effect of temperature has been factored out. The inset shows the behavior for increasing temperature of the theoretical phonon density. Reproduced from [3].

Figure 3.14: Comparison between theory and experiment for detuning dependent QD decay rates. Parameters used for the L3 cavity are: $\hbar\kappa_{\mathrm{L3}} = 195$ *µeV,* $\hbar g_{\mathrm{L3}} = 22$ *µeV, and* $\hbar\Gamma_{\mathrm{L3}} = 0.2$ *µeV. And for the AL cavity:* $\hbar\kappa_{\mathrm{AL}} = 230$ *µeV,* $\hbar g_{\mathrm{AL}} = 13.3$ *µeV,* $\hbar\Gamma_{\mathrm{AL}} = 0.4$ *µeV. The following harmonic confinement lengths were extracted for the QD wavefunctions:* $l_{\mathrm{e,xy}} = 3.4$ *nm,* $l_{\mathrm{e,z}} = 1.4$ *nm,* $l_{\mathrm{g,xy}} = 3.9$ *nm, and* $l_{\mathrm{g,z}} = 2.3$ *nm. Other parameters are is in table 3.1, except for an overall scaling of* $D^>(\omega)$ *by a factor of 5.57.*

of agreement the effective phonon density $D^>(\omega)$ has been scaled by a factor of 5.57 compared to the bare value derived from table 3.1. This rescaling is reasonable given the uncertainty on the input parameters of the model and has also been observed elsewhere, see the discussion in [78].

The large difference in the effect of phonons between the two cavity designs arises for the same reasons as discussed in connection with fig. 3.11. This difference can be emphasized by taken the large detuning limit of eq. (3.61), $|\Delta| \gg \gamma_{\mathrm{tot}}$ where phonons are most important, and dividing by Γ which yields

$$\frac{\Gamma_{\mathrm{tot}}}{\Gamma} = 1 + \frac{2g^2}{\Gamma} \times \frac{\gamma_{\mathrm{tot}} + \hbar^{-2}\mathrm{Re}[D^>(\omega = \Delta)]}{\Delta^2}. \tag{3.66}$$

This can be though as a generalized Purcell factor [3] and measures the enhancement of the decay rate relative to the background rate Γ. The second factor of the second term will be relatively similar for the two cavity designs, however if we calculate the prefactor for each cavity we get

$$\left(\frac{2g^2}{\Gamma}\right)_{\mathrm{L3}} \approx 4.96\ \mu\mathrm{eV}, \quad \left(\frac{2g^2}{\Gamma}\right)_{\mathrm{AL}} \approx 1.54\ \mu\mathrm{eV}. \tag{3.67}$$

This indicates that cavity-mediated effects, like the phonon-assisted Purcell effect, are more than a factor of 3 stronger in the L3 cavity compared to the AL cavity, given rise to the surprising qualitative difference between the two.

3.5 Summary

In this chapter, we have presented a theory for coupled QD-cavity systems including the interaction with phonons and illustrated the importance of the phonon interaction for the QD decay dynamics.

Furthermore, we have provided a detailed account of the theory used in recent studies [12, 3], which is based on a second order expansion in the phonon coupling, while accounting for the polaritonic nature of the QD-cavity to all orders. It was shown that it is essential to include the polaritonic nature in the interaction, when describing non-Markovian phonon reservoirs.

For elevated temperatures, multi-phonon effects are expected to play an important role. To study the influence of phonons in this regime, we included a theory based on the so-called polaron transformation, which takes certain phonon processes into account to infinite order, while still maintaining important polaritonic aspects of the QD-cavity system.

Using the polaron theory, an extensive investigation of the parameter dependence of the QD decay dynamics was carried out for experimentally relevant regimes. An asymmetric detuning-dependence of the QD lifetime was observed, where a positive detuning, $\omega_{\mathrm{eg}} > \omega_{\mathrm{cav}}$, yielded a significantly faster decay compared to negative detuning, $\omega_{\mathrm{eg}} < \omega_{\mathrm{cav}}$. The faster decay observed for positive detuning reflects that the QD may emit a photon by the simultaneous emission of a phonon, thereby overcoming the energy mismatch. Conversely, for negative detuning, absorption of a phonon is required to bridge the gap in energy, but at low temperatures phonon absorption is very unlikely. As the temperature is increased, the asymmetry gradually disappears, due to the availability of phonon absorption processes. Beyond introducing spectral asymmetries, the interaction with phonons also gives rise to a significantly increased bandwidth of the QD-cavity interaction. It greatly extents the bandwidth beyond that imposed by the cavity linewidth, normally thought to be the limiting factor, relaxing the resonant nature of many cQED phenomena.

We also provide a simple explanation for the lack of experimental observations of phonon-induced asymmetries in QD decay curves until recently [69, 3, 42]. We showed how the background decay rate of the QD, normally considered insignificant compared to other loss channels, plays a surprisingly important role in observing phonon effects for non-zero detuning. Phonon effects are strongest at relatively large detunings, $1-2$ meV in our case, which typically spans many cavity linewidths of $0.05-0.3$ meV, and thus the effect of the cavity is usually small at these detunings. In order for cavity-mediated effects, such as the phonon asymmetry, to remain significant either a small background decay or a large light-matter coupling strength is needed. Both of these requirements demand high quality samples, which have only become available recently.

To provide further insight into the physics, we derived approximate analytical expressions for the total QD decay rate, which distills the essential ingredients added by the phonon interaction to well-known results from cQED. The power and accuracy of these expressions has recently been demonstrated experimentally through an extraction of the effective phonon density [3] and verification of the predictions provided in the present thesis.

Beyond considerably influencing cQED dynamics for large detuning, phonons also have a pronounced effect for zero detuning, especially for elevated temperatures. In this case, we showed how the phonon interaction renormalized the QD-cavity coupling towards a lower effective value and investigated its influence on reaching the strong coupling regime. We found that the phase space for strong coupling became significantly smaller when including the phonon-induced QD-cavity coupling renormalization.

Chapter 4

Single-photon indistinguishability

The quantum mechanical nature of single photons is essential in linear optical quantum computing [1], relying on their ability to interfere with each other. Interference requires the photons to be coherent, which implies that they are indistinguishable in the quantum mechanical sense. The sensitive phase relation between the spectral components of a single-photon wavepacket can, however, be ruined by decoherence effects. Decoherence renders the photons distinguishable to some degree and thus decreases their applicability in linear optical quantum computing.

For a semiconductor SPS the main source of decoherence stems from the interaction with acoustic phonons [79, 80, 60] in the low temperature and weak excitation regime where a SPS is bound to operate. However, despite their fundamental role, little attention has been given to the influence of the phonon interaction on the coherence properties, and thus indistinguishability, of single photons. Only a few experimental investigations have been performed [81, 70, 82] and previous theoretical studies have employed a simple Markovian pure dephasing rate description [83, 84, 85, 86, 87, 88, 89, 90] or phenomenological finite-memory dephasing processes [91] to model the interaction with phonons, none providing a microscopic treatment. As demonstrated previously in this thesis, the influence of phonon scattering depends in a non-trivial fashion on the properties of the cQED system, hence simple phenomenological treatments can not be expected to yield accurate results.

In this chapter we present a microscopic model describing the effect of phonons on single-photon indistinguishability. We perform an exact diagonalization procedure on the coupled electron-photon-phonon system and hence retain all non-Markovian effects arising from the phonon interaction to all orders in the phonon coupling constant. We compare to the standard pure dephasing rate description based on Lindblad operators and to the long-time limit of the TCL approach employed in the previous chapter. Surprisingly, we find that both the Lindblad and long-time TCL approaches yield results, that are both quantitatively and qualitatively wrong in experimentally relevant parameter different regimes. The failure of these celebrated approximations, is traced back to their inadequacy in describing the short-time non-Markovian regime, which turns out to play an important role for the indistinguishability. This illustrates the importance of an accurate description of the short-time non-Markovian regime.

This chapter is mainly based on [92], while providing more details and several extended discussions.

4.1 Indistinguishability: The Hong-Ou-Mandel experiment

To experimentally measure the single-photon degree of indistinguishability, one employs a two-photon interference experiment, a so-called Hong-Ou-Mandel (HOM) experiment [93]. A schematic of the experimental setup is shown in fig. 4.1, where single photons are emitted from system 1 and 2 and subsequently brought to interfere on the 50/50 beam-splitter (BS). Even though the experimental setup looks similar to that of the well-known Hanbury Brown-Twiss (HBT) experiment [94], the two are different in nature despite that both probe two-photon correlations. In quantum optics, the HBT experiment is often used to determine whether a given emitter is a proper SPS. This is achieved by "splitting" a single light pulse on the BS and detecting coincidence events on the two output arms. The fundamental indistinguishability associated with quantum particles has the consequence that two single photons that enter the BS in different arms will coalesce into a single two-photon state, which exits the BS in either arm 3 or 4 with a 50 % chance of going either way [95]. The total absence of coincidence events implies that the single photons are indistinguishable, however any amount of decoherence will render the photons distinguishable, resulting in coincidence events at the two output arms.

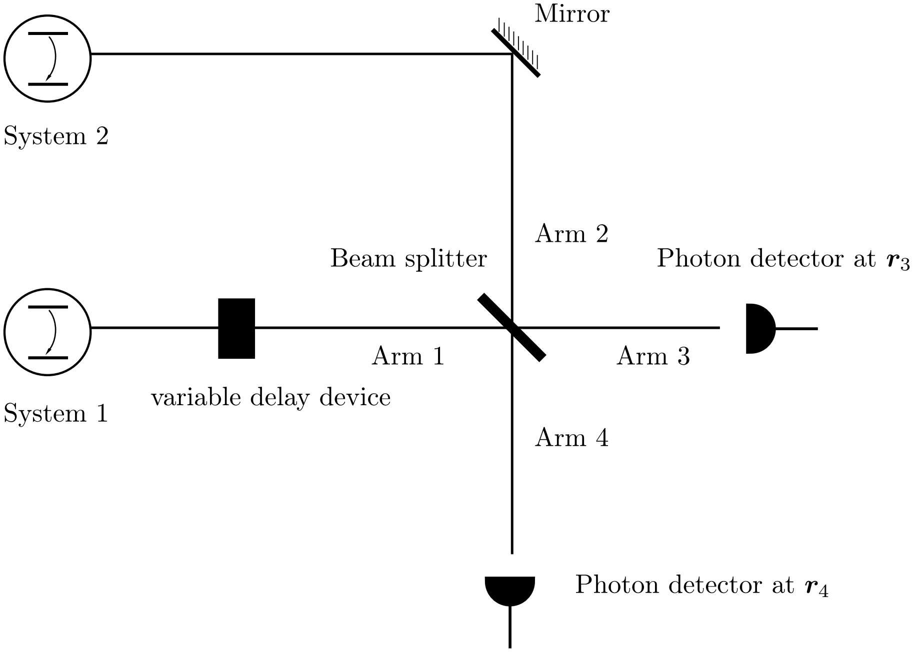

Figure 4.1: Schematic illustration of the HOM experiment designed to measure $G^{(2)}(\boldsymbol{r}_3 t_3, \boldsymbol{r}_4 t_4; \boldsymbol{r}_4 t_4, \boldsymbol{r}_3 t_3)$. A variable delay device is inserted to adjust the path length for the photons from system 1, so one may control the arrival times of photons from system 1 on the BS.

4.1.1 The HOM correlation function

The theoretical object describing the HOM experiment is the second order coherence function for the electromagnetic field operator, defined as [96]

$$G^{(2)}(\boldsymbol{r}_3 t_3, \boldsymbol{r}_4 t_4; \boldsymbol{r}_4 t_4, \boldsymbol{r}_3 t_3) = \langle E^{(-)}(\boldsymbol{r}_3, t_3) E^{(-)}(\boldsymbol{r}_4, t_4) E^{(+)}(\boldsymbol{r}_4, t_4) E^{(+)}(\boldsymbol{r}_3, t_3) \rangle , \tag{4.1}$$

which is related to the probability of detecting a photon at the space-time point $(\boldsymbol{r}_4, t_4)$ given that a photon was detected at $(\boldsymbol{r}_3, t_3)$. The field operators are defined in terms of positive and negative frequency components of the quantized electric field as

$$E^{(+)}(\boldsymbol{r}, t) = \sum_m \mathcal{E}_m a_m(t) u_m(\boldsymbol{r}), \quad E^{(-)}(\boldsymbol{r}, t) = \sum_m \mathcal{E}_m a_m^\dagger(t) u_m(\boldsymbol{r}). \tag{4.2}$$

The mode functions, $u_m(t)$, and expansion coefficients, $\mathcal{E}_m$, are assumed to be real. For simplicity we will assume that the fields on both sides of the BS can be represented by a single quasi- or wavepacket-mode in each arm, hence

$$E^{(-)}(\boldsymbol{r}, t) = \sum_{\substack{i=1,2\\ \text{or}\\ 3,4}} E_i^{(-)}(\boldsymbol{r}, t) = \sum_{\substack{i=1,2\\ \text{or}\\ 3,4}} \mathcal{E}_i a_i^\dagger(t) u_i(\boldsymbol{r}). \tag{4.3}$$

On the input side of the BS these quasi-modes are taken as the intra-cavity quasi-modes of the cQED system, which will be related to those on the output side by a simple BS relation. Applying this set of approximations hugely simplifies the calculation of the second order coherence function, since we avoid having to deal with radiation modes in the far field where the actual detectors are located. The price to pay is the neglect of any kind of propagation effects from the cavity to the detector. The neglect of such effects is justified if the Green's function, propagating the light from the cavity to the detector, only has a weak frequency dependence in the vicinity of the cavity and QD transition frequencies [97].

To proceed, we insert eq. (4.3), with $i = 3, 4$, into eq. (4.1) resulting, in a number of different photon correlation functions. Fortunately, most of these can be neglected as they contain spatial cross terms of the type $u_3(\boldsymbol{r}_4)$ or $u_4(\boldsymbol{r}_3)$, where a spatially localized mode function is evaluated at the detector position in the other output arm, which can safely neglected. Neglecting these cross terms we get

$$G^{(2)}_{\mathrm{HOM}}(t_3, t_4) = \langle a_3^\dagger(t_3) a_4^\dagger(t_4) a_4(t_4) a_3(t_3) \rangle , \tag{4.4}$$

where we omitted a constant prefactor and simplified the notation. Next, we relate the output photon operators to those on the input side, using a standard 50/50 BS relation [84]

$$\begin{bmatrix} a_3(t) \\ a_4(t) \end{bmatrix} = \frac{1}{\sqrt{2}} \begin{bmatrix} 1 & -e^{-i\pi/4} \\ e^{i\pi/4} & 1 \end{bmatrix} \begin{bmatrix} a_1(t) \\ a_2(t) \end{bmatrix} , \tag{4.5}$$

performing the BS action as a unitary operation. Using eq. (4.5) in eq. (4.4) generates 16 terms, expressing $G^{(2)}_{\mathrm{HOM}}(t_3, t_4)$ in terms of input photon operators.

To simplify the further analysis, we assume that system 1 and 2 are identical and independent. The identical part means that their respective Hamiltonians are equal, and the independence means that their Hamiltonians commute, $[H_1, H_2] = 0$, i.e. do not interact. The independence leads to an exact factorization of expectation values involving system 1 and 2, e.g. $\langle a_2^\dagger(t_3)a_1^\dagger(t_4)a_1(t_4)a_2(t_3)\rangle = \langle a_2^\dagger(t_3)a_2(t_3)\rangle \langle a_1^\dagger(t_4)a_1(t_4)\rangle$. The assumption of identical subsystems effectively means that we only need to consider a single system and hence we omit the reference to the individual systems. In practice this situation can be realized by employing the same cQED system as both system 1 and 2, using the following procedure; The first emitted photon transmitted along a longer path, while the system returns to equilibrium and is excited again to emit the second photon, which is brought to interfere with the first (delayed) photon on the BS. In the end we obtain

$$\begin{aligned}G^{(2)}_{\mathrm{HOM}}(t_3, t_4) = {} & \langle a^\dagger(t_3)a(t_3)\rangle \langle a^\dagger(t_4)a(t_4)\rangle - |\langle a^\dagger(t_3)a(t_4)\rangle|^2 + \langle a^\dagger(t_3)a^\dagger(t_4)a(t_4)a(t_3)\rangle \\ & + \frac{1}{\sqrt{2}}\left[\langle a^\dagger(t_3)a^\dagger(t_4)a(t_3)\rangle \langle a(t_4)\rangle + \langle a^\dagger(t_3)a(t_4)a(t_3)\rangle \langle a^\dagger(t_4)\rangle\right. \\ & \left. - \langle a^\dagger(t_3)a^\dagger(t_4)a(t_4)\rangle \langle a(t_3)\rangle - \langle a^\dagger(t_4)a(t_4)a(t_3)\rangle \langle a^\dagger(t_3)\rangle\right]. \qquad (4.6)\end{aligned}$$

The correlation functions in the second and third lines all contain an odd number of photon operators, and will only be non-zero if the cavity field is coherent. A coherent cavity field can only arise if the cQED system is driven coherently. In general, a cQED system can be excited using two different schemes; through relaxation from higher excited states or through resonant / quasi-resonant excitation with a short optical pulse. In the first case, the relaxation processes responsible for loading the QD with the excitation are inherently incoherent in nature and thus the excitation will also arrive in an incoherent state. In the second case, the QD is excited using a short coherent pulse. However, if the duration of the pulse is much shorter than typical timescales in the cQED system, the coherence induced by the pulse during its passage will be negligible. Hence, in both cases we may omit the terms in the last two lines of eq. (4.6) from the further analysis. The last term in the first line is equal to the second order correlation function measured in the HBT experiment, where coincidence events signify that the source does not satisfy the requirements for a SPS. In a theoretical analysis we can rigorously enforce a SPS simply by only including 1-photon states in the Hilbert space in which case the HBT contribution is identically zero. Under these assumptions we finally obtain

$$G^{(2)}_{\mathrm{HOM}}(t+\tau, t) = \langle a^\dagger(t+\tau)a(t+\tau)\rangle \langle a^\dagger(t)a(t)\rangle - |\langle a^\dagger(t+\tau)a(t)\rangle|^2, \qquad (4.7)$$

where we introduced the difference time $\tau = t_3 - t_4$ and relabeled $t = t_4$. This expressions forms the basis for investigating indistinguishability in the rest of this thesis. We note that while the above derivation was performed for light emission from the cavity, a similar exercise could be performed for light emitted from any source. The end result would be a suitable replacement of the photon operators $a^\dagger$ and a with the corresponding creation and annihilation operators for this system, e.g., for a two-level QD one should use $\sigma_+ = |\mathrm{e}\rangle\langle\mathrm{g}|$ and $\sigma_- = |\mathrm{g}\rangle\langle\mathrm{e}|$.

4.1.2 The degree of indistinguishability and pure dephasing

As discussed above, perfectly indistinguishable single photons imply the complete absence of coincidence events in a HOM experiment, whereas any amount of decoherence will lead to coincidence events. Based on this observation, we [83, 84] define the degree of indistinguishability, I, as the two-time integrated second order coherence function $G^{(2)}_{\mathrm{HOM}}(t+\tau,t)$ normalized by the same coherence function with no interference taking place, i.e., with no BS in the experimental setup, and subtract this from unity. Formally,

$$\begin{aligned} I &= 1 - \frac{\int_{-\infty}^{+\infty} dt \int_{-\infty}^{+\infty} d\tau G^{(2)}_{\mathrm{HOM}}(t+\tau,t)}{\int_{-\infty}^{+\infty} dt \int_{-\infty}^{+\infty} d\tau G^{(2)}_{\mathrm{no-BS}}(t+\tau,t)} && (4.8) \\ &= 1 - \frac{\int_{-\infty}^{+\infty} dt \int_{0}^{+\infty} d\tau G^{(2)}_{\mathrm{HOM}}(t+\tau,t)}{\int_{-\infty}^{+\infty} dt \int_{0}^{+\infty} d\tau G^{(2)}_{\mathrm{no-BS}}(t+\tau,t)}, && (4.9) \end{aligned}$$

where in the second line we have used the relation $G^{(2)}(t,t') = [G^{(2)}(t',t)]^*$ [96] and the fact that both $G^{(2)}_{\mathrm{HOM}}(t+\tau,t)$ and $G^{(2)}_{\mathrm{no-BS}}(t+\tau,t)$ are real quantities. The second order coherence function may be decomposed as

$$G^{(2)}_{\mathrm{HOM}}(t+\tau,t) = G^{(2)}_{\mathrm{no-BS}}(t+\tau,t) - C(t+\tau,t), \tag{4.10}$$

where

$$G^{(2)}_{\mathrm{no-BS}}(t+\tau,t) = \langle A^\dagger(t+\tau)A(t+\tau)\rangle \langle A^\dagger(t)A(t)\rangle, \tag{4.11}$$

is the second order coherence function for the HOM experiment with no interference taking place and

$$C(t+\tau,t) = |\langle A^\dagger(t+\tau)A(t)\rangle|^2, \tag{4.12}$$

is the contribution arising from the interference. The operator A represents the relevant quantum field. Using the above, the degree of indistinguishability can be calculated as

$$I = \frac{\int_{-\infty}^{+\infty} dt \int_{0}^{+\infty} d\tau C(t+\tau,t)}{\int_{-\infty}^{+\infty} dt \int_{0}^{+\infty} d\tau G^{(2)}_{\mathrm{no-BS}}(t+\tau,t)}. \tag{4.13}$$

It is worth noting that this expression for the indistinguishability only contains first order coherence functions and none of second order, which might seem a bit peculiar as we model a two-photon experiment. Formally, this arised as we assumed the two photon-emitting systems to be independent and neglected trivial two-photon processes within each system. Physically, it makes sense as the indistinguishability is a single-photon property and the two-photon HOM experiment is only a means to probe the degree of indistinguishability.

To verify that eq. (4.13) behaves as expected according to the heuristic arguments used to derive it, we calculate the indistinguishability for the simplest, yet non-trivial, cQED system relevant for experiments, namely a QD weakly coupled to a cavity. The decay dynamics of this system was treated in section 3.3.2 where adiabatic elimination of the cavity lead to an expression, see eq. (3.58), for the effective decay rate of the QD

$$\Gamma_{\text{eff}} = \Gamma + 2g^2 \frac{\gamma_{\text{tot}}}{\gamma_{\text{tot}}^2 + \Delta^2}, \quad \gamma_{\text{tot}} = \frac{1}{2}(\kappa + \Gamma) + \gamma, \tag{4.14}$$

where the explicit phonon coupling has been omitted and the total dephasing rate, γ_{tot}, crucially includes the pure dephasing rate γ. To calculate the indistinguishability of this system we need two correlation functions, namely $\langle \sigma_{\text{eg}}(t+\tau)\sigma_{\text{ge}}(t)\rangle$ and $\langle \sigma_{\text{ee}}(t)\rangle$. The excited state QD population is trivially given by

$$\langle \sigma_{\text{ee}}(t)\rangle = \exp(-\Gamma_{\text{eff}} t), \tag{4.15}$$

where an initially fully excited QD has been assumed. From the EOM of $\langle \sigma_{\text{eg}}(t)\rangle$

$$\partial_t \langle \sigma_{\text{eg}}(t)\rangle = (i\Delta - \Gamma_{\text{eff}}/2 - \gamma) \langle \sigma_{\text{eg}}(t)\rangle, \tag{4.16}$$

the relevant two-time function may be found using the QRT, eq. (2.72), and is

$$\langle \sigma_{\text{eg}}(t+\tau)\sigma_{\text{ge}}(t)\rangle = \langle \sigma_{\text{ee}}(t)\rangle \exp\left[(i\Delta - \Gamma_{\text{eff}}/2 - \gamma)\tau\right]. \tag{4.17}$$

Inserting these expressions into eq. (4.13) we obtain a simple expression for the indistinguishability of single photons emitted from a weakly coupled cQED system [83, 88]

$$I = \frac{\Gamma_{\text{eff}}}{\Gamma_{\text{eff}} + 2\gamma}. \tag{4.18}$$

In the limit of vanishing pure dephasing, i.e. $\gamma \to 0$, the indistinguishability is seen to approach unity as expected.

This simple expression has formed the basis for understanding the effect of pure dephasing on photon indistinguishability. It basically expresses that one should either decrease the pure dephasing rate, e.g. through freezing out phonons by going to low temperatures, or decrease the QD lifetime, e.g. by placing the QD in a cavity and exploiting the Purcell effect to achieve a large Γ_{eff}. Low temperatures in all-solid-state quantum optical experiments has long been a necessity for obtaining a reasonable signal-to-noise ratio. However, even at temperatures very close to absolute zero a finite dephasing rate has been measured [79, 70], from the results presented in section 3.3.1 it is apparent that even at $T = 0$ K phonon emission processes can still occur leading to decoherence. The pursuit of larger indistinguishability has therefore mainly been focused on lowering the QD lifetime through placing it in a cavity and utilizing the Purcell effect. The underlying assumption behind this optimization strategy is that the pure dephasing rate, or more generally, the decoherence processes, remain unaffected by changing any of the parameters leading to a larger Purcell effect, typically g, Δ, and κ. As we will demonstrate, this assumption does not hold in general and in fact the decoherence induced by phonons depends strongly on the properties of the cQED system.

4.2 Theory

4.2.1 Modeling indistinguishability

To investigate the effect of the phonon interaction on the indistinguishability we employ the same cQED model as used to describe QD decay dynamics in chapter 3, see section 3.1 for the details. However, where the populations of the cQED system, describing the decay dynamics, are one-time correlation functions (CFs), the indistinguishability is inherently a two-time quantity owing to the nature of the HOM experiment. Typically, cQED models deal with completely Markovian reservoirs and obtaining two-time, or multi-time, CFs is in principle no more complicated than obtaining one-time CFs. This is due to the QRT, which asserts that multi-time CFs evolve in time according to the same EOM as one-time CFs, see section 2.3.1. However, in the general case of a non-Markovian reservoir, the QRT does not hold, as one can no longer assume that the total density matrix factorizes at all times, see section 2.3.2.

The non-Markovianity of the reservoir manifests itself through memory-effects, which in the TCL framework results in time-dependent scattering rates, placing the system in the short-time non-Markovian regime, according to the discussion in section 2.2.3. The extent of the short-time non-Markovian regime is governed by the memory-depth of the reservoir, which for typical phonon reservoirs is on the order of a few picoseconds, see fig. 3.3. Studying one-time dynamics, e.g. populations, the short-time non-Markovian regime is only important within a timespan limited by the memory-depth from the initial excitation of the system, see discussion section 3.2.6, and the long-time non-Markovian regime provides an excellent description of the population dynamics.

If we consider the EOM for the two-time CF, eq. (2.93), we observe that the time-integrals contain the difference time τ in the integration limits, rather than the absolute "laboratory" time t. Hence, we can not naively expect the importance of the short-time non-Markovian regime to be related to the value of the absolute time t, as was the case for the one-time dynamics. Physically, this can be understood by considering the two-time plane, see fig. 4.2, in which the two-time photon correlation function, $\langle a^\dagger(t+\tau)a(t)\rangle$, exists. The two-time function probes temporal correlations by, at *each* instant t, removing a photon from the system, $a(t)$, and at an instant $t+\tau$ later adding it back, $a^\dagger(t+\tau)$, and then records the probability of the process. The fact that this excitation "measurement" occurs at each instant in the laboratory time frame t, means that we continuously enter new short-time non-Markovian regimes, illustrated as the shaded band surrounding the time-diagonal in fig. 4.2. Consequently, we can

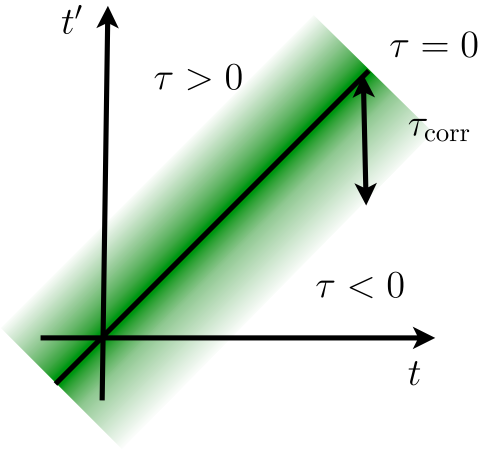

Figure 4.2: Two-time plane for the photon correlation function $\langle a^\dagger(t+\tau)a(t)\rangle$, indicating the time-diagonal, $\tau = 0$, and an indication of the short-time non-Markovian regime illustrated as the shaded region surrounding the time-diagonal, with a width given by the reservoir correlation time τ_{corr}.

expect short-time non-Markovian effects to play an important role throughout the entire lifetime of the excitation, as opposed to one-time correlation functions, where these effects are limited to a short time interval after the initial excitation.

Having explained why the short-time non-Markovian regime is expected to be important when modeling indistinguishability, it would seem that the next logical step would be to employ eq. (2.93) to calculate the indistinguishability in the presence of phonons. We will, however, pursue another approach for obtaining the two-time photon correlation functions involving an exact diagonalization (ED) procedure of the complete coupled system. Following such an approach is obviously more accurate than any of the approximate formalisms we have presented so far, as it treats the non-Markovian reservoir to all orders and rigorously includes all memory-effects associated with the reservoir interaction providing an equal-footing treatment of coupled electron-photon-phonon system. An ED procedure implies that all phonon related Hamiltonians are now included in the system Hamiltonian governing the EOM for the RDM, see eq. (2.70), hence the QRT can be used to calculate two-time functions without any approximations relating to the phonon interaction. The downside of such an approach is that it is bound to be numerical in nature and as such will, by itself, not provide much insight into the physics and will basically act as a "black-box" experiment. However, as we will demonstrate much useful insight can be extracted from the ED approach, as we have easy access to study the full dynamics of the phonon degrees of freedom. This allows for a less abstract understanding of the reservoir processes causing decoherence, as now these can easily be associated with actual dynamics. A further advantage of the ED approach, is that it offers the rare opportunity to quantify the accuracy of approximative methods, which is seldom in the field of open quantum systems.

4.2.2 Effective phonon modes *a la* Hohenester

In this section we will describe the enabling step, due to Hohenester [98], for performing the ED procedure consisting of replacing the original set of 3D phonon modes with in an effective set of 1D modes. The reduction in dimensionality is necessary as a full treatment of 3D phonon modes would be beyond the computational capabilities of most university clusters, whereas a 1D model can be treated even on a personal laptop.

Our starting point for deriving the effective 1D modes is the total Hamiltonian, eq. (3.10), of the unitarily coupled electron-photon-phonon system

$$H = H_{\mathrm{JC}} + \sigma_{\mathrm{ee}} \sum_{\boldsymbol{k}} M^{\boldsymbol{k}} (b^{\dagger}_{-\boldsymbol{k}} + b_{\boldsymbol{k}}) + \sum_{\boldsymbol{k}} \hbar\omega_{\boldsymbol{k}} b^{\dagger}_{\boldsymbol{k}} b_{\boldsymbol{k}}, \tag{4.19}$$

where the cQED system represented by the Jaynes-Cummings Hamiltonian

$$H_{\mathrm{JC}} = \hbar\Delta\sigma_{\mathrm{ee}} + \hbar g(a\sigma_{\mathrm{eg}} + a^{\dagger}\sigma_{\mathrm{ge}}). \tag{4.20}$$

The phonon wavevector $\boldsymbol{k} = (k_x, k_y, k_z)$ is a 3D vector which we would like to reduce to a 1D vector. To this end, we note that our model describing the LA phonons, see sections 2.4.3 and 2.4.4, is assumed to be isotropic, hence no single direction in space is preferred by these modes, rendering the phonon dispersion relation a function of the length of $\boldsymbol{k}$ alone, $\omega_{\boldsymbol{k}} = f(|\boldsymbol{k}|) \equiv f(k)$. The phonon matrix element, see eqs. (3.6) and (3.9), however, depends explicitly on the electronic wavefunctions as

$$M^{\boldsymbol{k}} = \sqrt{\frac{\hbar k}{2dc_{\mathrm{s}}V}} \int d\boldsymbol{r} \left[D_{\mathrm{e}}|\phi_{\mathrm{e}}(\boldsymbol{r})|^2 - D_{\mathrm{g}}|\phi_{\mathrm{g}}(\boldsymbol{r})|^2\right] e^{-i\boldsymbol{k}\cdot\boldsymbol{r}}. \tag{4.21}$$

The disc shaped wavefunctions employed in the previous chapter, section 3.1 and eq. (3.7), introduces an angular dependence on $\boldsymbol{k}$ in the phonon matrix element. However, if we employ an isotropic harmonic confinement, we obtain spherically symmetric wavefunctions given by

$$\phi_{\nu}(r) = \frac{1}{\pi^{3/4} l_{\nu}^{3/2}} e^{-r^2/(2l_{\nu}^2)}. \tag{4.22}$$

Inserting this into the phonon matrix element we get

$$M^{k} = \sqrt{\frac{\hbar k}{2dc_{\mathrm{s}}V}} \left[D_{\mathrm{e}} e^{-\frac{1}{4}(kl_{\mathrm{e}})^2} - D_{\mathrm{g}} e^{-\frac{1}{4}(kl_{\mathrm{g}})^2}\right], \tag{4.23}$$

which only depends on k. We have now reduced all numerical quantities in the Hamiltonian to depend only on k, hence every phonon process will take place on spherical shells in $\boldsymbol{k}$-space with a radius of k.

To obtain an effective description of this physical situation let us consider the greater phonon correlation function, eq. (3.33), for simplicity evaluated at zero temperature, and take the integral limit of the sum

$$D^{>}(t) = \sum_{\boldsymbol{k}} |M^{k}|^2 e^{i\omega_k t} \tag{4.24}$$

$$= 4\pi \frac{V}{(2\pi)^3} \int_0^\infty dk k^2 |M^k|^2 e^{i\omega_k t} \tag{4.25}$$

$$\approx 4\pi \frac{V}{(2\pi)^3} \sum_p \Delta k_p k_p^2 |M^{k_p}|^2 e^{i\omega_{k_p} t} \tag{4.26}$$

$$= \sum_p |\tilde{M}_p|^2 e^{i\omega_{k_p} t}, \tag{4.27}$$

where we introduced the effective phonon matrix element

$$\tilde{M}_p = \sqrt{4\pi \Delta k_p k_p^2 V/(2\pi)^3} M_{k_p}, \;\; \Delta k_p = k_{p+1} - k_p. \tag{4.28}$$

This shows as that one may obtain an arbitrarily good approximation to the correlation function $D^{>}(t)$ by replacing the original 3D modes with an effective discrete 1D set with a slightly modified matrix elements $\tilde{M}_p$ and discrete (radial) wavevectors k_p. Motivated by this, we replace the original Hamiltonian by

$$H = H_{\mathrm{JC}} + \sigma_{\mathrm{ee}} \sum_p \tilde{M}_p (\tilde{b}_p^\dagger + \tilde{b}_p) + \sum_p \hbar\omega_p \tilde{b}_p^\dagger \tilde{b}_p, \tag{4.29}$$

where $\omega_p \equiv \omega_{k_p} = c_{\mathrm{s}} k_p$ and $\tilde{b}_p$, $\tilde{b}_p^\dagger$ are standard bosonic operators for the new effective phonon modes.

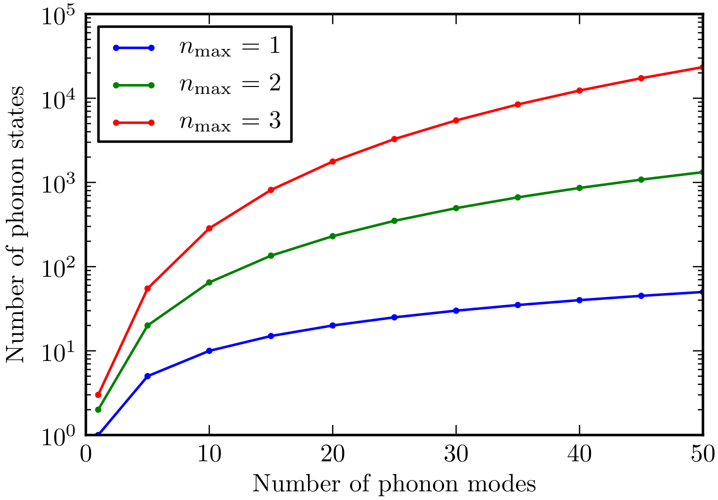

Figure 4.3: Total dimension of phonon Hilbert space as a function of number of phonon modes for 1, 2, and 3 excitations, see eq. (4.31).

Having reduced the phonon modes to 1D is a huge simplification and a phonon Fock state becomes

$$|n_0, n_1, \ldots, n_{N-1}\rangle = \frac{(\tilde{b}_0^\dagger)^{n_0}}{\sqrt{n_0!}} \frac{(\tilde{b}_1^\dagger)^{n_1}}{\sqrt{n_1!}} \cdots \frac{(\tilde{b}_{N-1}^\dagger)^{n_{N-1}}}{\sqrt{n_{N-1}!}} |0\rangle , \tag{4.30}$$

where n_p is the occupation number for mode p and N is the total number of included modes. If we only include a single phonon excitation the dimension of the phonon Hilbert space will be $N + 1$. However, beyond one excitation the dimension becomes equal to the number of ways to put n excitation in N modes, which is [99]

$$\texttt{Dim}(N, n_{\max}) = \sum_{n=1}^{n_{\max}} \texttt{div}[\texttt{div}[(N - n + 1)!, n!], (N - 1)!], \tag{4.31}$$

where $\texttt{div}[p, q]$ denotes integer division between integers p and q. This function is illustrated in fig. 4.3 for up to 50 modes and 3 excitations and shows that even for very few excitations and a moderate number of modes we easily end up with thousands of phonon states. However, from the analysis of QD decay dynamics in section 3.3, we know that not all phonon modes are equally important, as illustrated in fig. 3.7, showing the interaction matrix element, eq. (4.23). Furthermore, we know from the exact solution of the independent boson model [98] that the effective interaction strength of each phonon mode scales as the dimensionless number $\alpha_p = |\widetilde{M}_p/(\hbar\omega_p)|$, which makes sense physically as low energy modes should be easier to excite. The importance of a given phonon state can therefore be quantified by calculating

$$\Lambda(n_0, n_1, \ldots, n_{N-1}) = \frac{\alpha_0^{n_0} \times \alpha_1^{n_1} \times \cdots \times \alpha_{N-1}^{n_{N-1}}}{\alpha_{\max}}, \tag{4.32}$$

where $\alpha_{\max}$ is the maximum value of the dimensionless coupling constant, corresponding to the most important phonon state. $\Lambda(n_0, n_1, \ldots, n_{N-1})$ can now be compared to a specified cut-off, ϵ, where only states above the cut-off are included in the simulation.

In fig. 4.4 we show the effect of the cut-off procedure on the dimensionality of the phonon Hilbert space for equal sized QD wavefunctions, $l_\mathrm{e} = l_\mathrm{g} = 5$ nm, where the other parameters are as in table 3.1. For a fixed maximum phonon wavevector, $k_{\max}$, the maximum number of available phonon modes is determined by Δk as $N = \texttt{int}(k_{\max}/\Delta k)$. However, according to the specified cut-off only the most important modes will be included, hence the cut-off determines the actual number of the modes included (and thus also $k_{\max}$) in a simulation, which will always be smaller than $N = \texttt{int}(k_{\max}/\Delta k)$. This dependence is indicated in the figure legend in fig. 4.4. Illustrations of the actual phonon Hilbert spaces are shown in fig. 4.4(a), (b), and (c) for cut-off values corresponding the inclusion of one-phonon, two-phonon, and three-phonon excitations, respectively. The transition from including n to $n + 1$ excitations is clearly visible in the bottom figure as distinct kinks in the curve, occuring

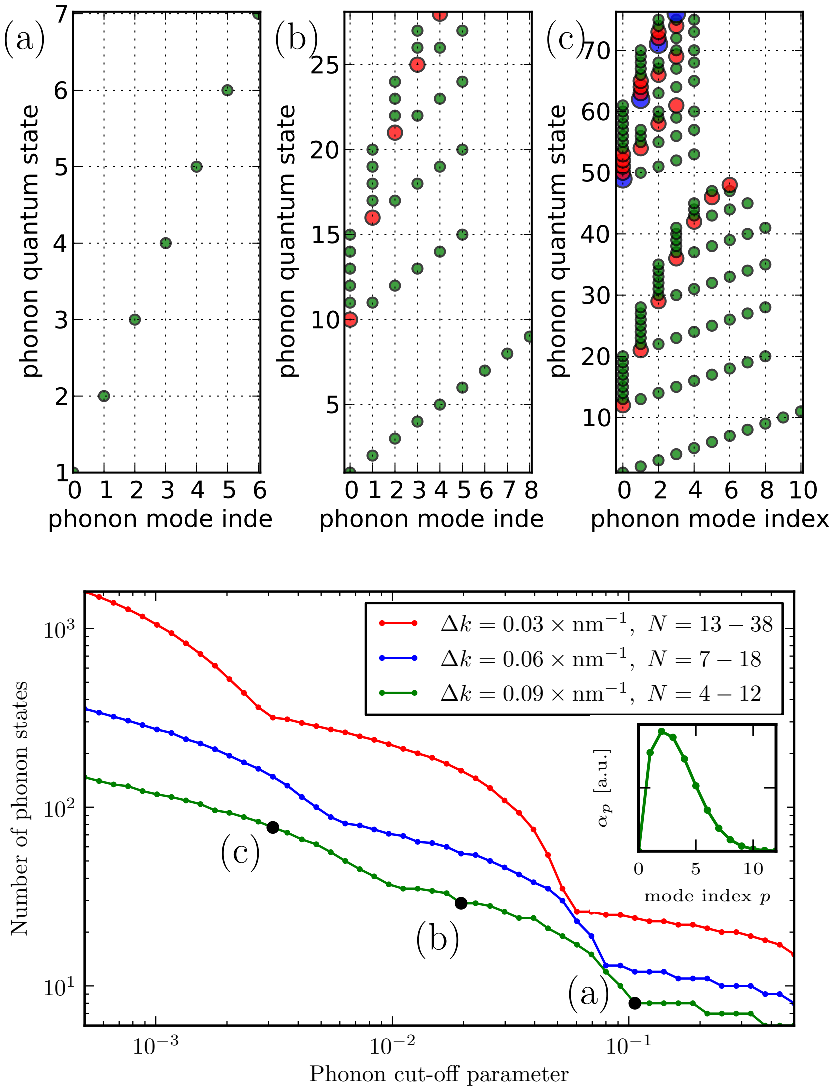

Figure 4.4: Illustration of the cut-off scheme. Dimensionality of phonon Hilbert space as a function of cut-off parameter, ϵ, for three values of the equidistant grid spacing in k-space, Δk. The number of phonon modes is also indicated, which depends on ϵ. The inset shows the dimensionless coupling α_p for $\Delta k = 0.09 \times \mathrm{nm}^{-1}$. (a), (b), and (c) show all phonon quantum (Fock) states, see eq. (4.32), included for three typical cut-off values, containing one-phonon (green), two-phonon (red), and three-phonon (blue) excitations. Parameters: $l_\mathrm{e} = l_\mathrm{g} = 5$ nm, the rest are as in table 3.1.

when

$$\epsilon_\mathrm{kink} = \frac{\alpha_\mathrm{max}^{n+1}}{\alpha_\mathrm{max}}. \tag{4.33}$$

In fig. 4.4(b) and (c) we see a preference for including modes with small mode index, which correlates nicely with the dimensionless coupling α_p shown in the inset in the bottom figure.

Using Δk and the cut-off parameter ϵ, we can easily control the number of phonon states included in the simulations and obtain a solution to a given degree of accuracy, resulting in a numerically exact solution of the many-body problem.

4.2.3 Numerical implementation

In sections 3.1 and 3.2.3 the EOM for studying phonon effects in the TCL, were set up analytically and the full system of equations was presented. This makes perfect sense for quantum systems where the Hilbert space dimension is small, as one may become more familiar with the individual terms and more easily extract physical insight from the equations. However, once the Hilbert space dimension increases, the number of equations increases dramatically and it becomes less useful and practical to derive the EOM by hand. For the ED approach we therefore employ a more systematic approach for setting up the EOM. The matrix describing an operator in the total composite Hilbert space is obtained as

$$O_{\text{total}} = O_{\text{cav}} \otimes O_{\text{QD}} \otimes O_{\text{phon}}, \tag{4.34}$$

where $O_{\text{sub-system}}$ denotes an operator in the respective subsystem and $\otimes$ is the tensor product. From this follows that dimension of the total Hilbert space, P_{total}, scales as

$$P_{\text{total}} = P_{\text{cav}} P_{\text{QD}} P_{\text{phon}}, \tag{4.35}$$

where $P_{\text{sub-system}}$ is the dimension of the respective subsystem. This formula shows an aggressive scaling, illustrating the challenges faced when investigating multiple subsystems.

As discussed in section 4.2.1, due to the exact treatment of the phonon degrees of freedom, the QRT remains valid for calculating two-time functions. From section 2.3.1 it then follows that we need to solve for the modified RDM, eq. (2.67), which can be done efficiently in the Schrödinger picture. For computational reasons, related to the memory layout in modern computers, it is, however, advantageous to solve for the transposed RDM

$$\Sigma(t) = [\rho(t)]^T. \tag{4.36}$$

This is easily illustrated by considering the expectation value of an arbitrary operator

$$\begin{aligned} \langle A(t) \rangle &= \mathrm{Tr}\left[\rho(t) A\right] && (4.37) \\ &= \sum_{a_1 a_2} \rho_{a_2 a_1}(t) A_{a_1 a_2} && (4.38) \\ &= \sum_{a_1 a_2} \Sigma_{a_1 a_2}(t) A_{a_1 a_2}, && (4.39) \end{aligned}$$

where the indices of A and $\Sigma(t)$ appear in the same order, whereas they do not for $\rho(t)$, reflecting how the arrays storing $\Sigma(t)$ and $\rho(t)$ are laid out in memory. This has the consequence that the trace operation can be performed more memory efficient for transposed RDM as oppose to the normal RDM.

The EOM for $\Sigma(t)$ is obtained by taking the transpose of the EOM for $\rho(t)$, hence combining the coherent time-evolution with a sum of generic Lindblad terms, eq. (2.55), we get

$$\partial_t\Sigma = -i\hbar^{-1}\left[\Sigma H^T - H^T\Sigma\right] - \sum_i \frac{\Gamma_i}{2}\left[\Sigma L_i^T L_i^* + L_i^T L_i^*\Sigma - 2L_i^*\Sigma L_i^T\right] \tag{4.40}$$

where we used that $(O^\dagger)^T = O^*$ and for notational simplicity omitted the time argument on $\Sigma(t)$. The above EOM is in a matrix form, which is less practical for our purposes, however, using the `vec` operation [100] we may bring the equation into much more useful vector form. The `vec` operation is defined as

$$\texttt{vec}(AXB) = (A \otimes B^T)\boldsymbol{x} \tag{4.41}$$

where the "row-stacked" version of the matrix X is

$$\boldsymbol{x} = \texttt{vec}(X) = [X_{00}, X_{01}, X_{02}, \ldots, X_{10}, X_{11}, X_{12}, \ldots]^T. \tag{4.42}$$

If we write eq. (4.40) as

$$\partial_t\Sigma = -i\hbar^{-1}\left[I\Sigma H^T - H^T\Sigma I\right] - \sum_i \frac{\Gamma_i}{2}\left[I\Sigma L_i^T L_i^* + L_i^T L_i^*\Sigma I - 2L_i^*\Sigma L_i^T\right], \tag{4.43}$$

employing the `vec` operation yields

$$\partial_t \langle\boldsymbol{\sigma}(t)\rangle = M\langle\boldsymbol{\sigma}(t)\rangle, \tag{4.44}$$

with

$$\langle\boldsymbol{\sigma}(t)\rangle = \texttt{vec}(\Sigma(t)) = [\Sigma_{00}(t), \Sigma_{01}(t), \Sigma_{02}(t), \ldots, \Sigma_{10}(t), \Sigma_{11}(t), \Sigma_{12}(t), \ldots]^T \tag{4.45}$$

and where the coupling matrix is given by

$$\begin{aligned} M = {} & -i\hbar^{-1}\left(I\otimes H - H^T\otimes I\right) \\ & -\sum_i \frac{\Gamma_i}{2}\left(I\otimes L_i^\dagger L_i + \left[L_i^\dagger L_i\right]^T \otimes I - 2L_i^*\otimes L_i\right), \end{aligned} \tag{4.46}$$

which plays a role identical to the Liouvillian super-operator of the density matrix, eq. (2.70). We note that the dimension of M scales as P_{total}^2 with being P_{total} the Hilbert space dimension.

In section 3.2.3 we saw that the coupling matrix for the Jaynes-Cummings model contained several independent blocks, where only the block relevant for the specific physical quantity in question needed to be taken into account.

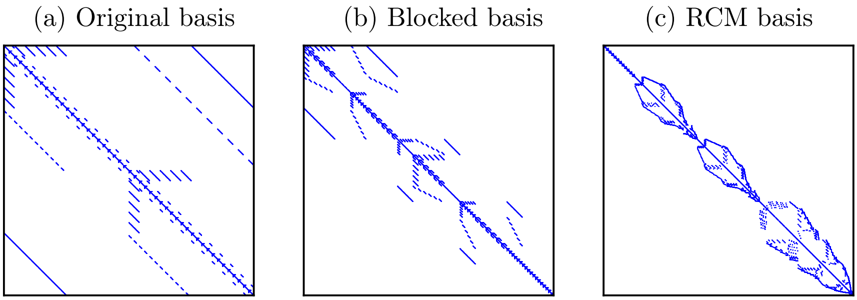

Figure 4.5: Illustration of the coupling matrix M, eq. (4.46)*, in different bases; (a) original basis, (b) basis that orders M into a diagonal block structure, and (c) the reverse Cuthill-McKee basis (RCM) which minimizes the matrix bandwidth, as well as revealing the block structure. Blue denotes non-zero values, while white denotes zero values.*

While exploiting this feature is rather trivial for a 9×9 M matrix, it becomes significantly more difficult if M consists of tens of thousands of rows and columns. This is the case for the ED approach, where even a moderate case of 50 phonon states leads to a dimensionality of $(2 \times 2 \times 50)^2 = 40 \times 10^3$ of M. In fig. 4.5(a) we show M for an illustrative set of parameters in the basis obtained by performing the steps outlined above. We notice that M is a rather sparse matrix, which is very fortunate in terms of computational resources, but on the other hand no obvious block structure of the matrix is seen. Figuring out which possible independent blocks exists for M is a computationally very hard problem, which is dealt with in the mathematically field of graph theory where a matrix is represented as an abstract graph object. Efficient algorithms for finding the connected components of a graph are available in several software packages. These algorithms yield a reordered basis where the (possible) block structure of a matrix is clear. The result of such a reordering is illustrated in fig. 4.5(b) where the underlying block structure of the matrix is evident. One may go one step further and try to minimize the bandwidth of the resulting blocks, which can be achieved using the reverse Cuthill-McKee (RCM) algorithm [101], see fig. 4.5(c) for an example of such a minimization. Ideally, the RCM results in faster matrix-vector products, however, we did not find any significant speed-up using the RCM possibly related to a too small matrix size, hence we have employed the simple blocked basis in our code.

In order to verify the effective phonon model and our numerical implementation we have compared with exact analytical solutions obtained for the independent boson model [10], which corresponds to our model for the case of $g = 0$. The analytical solutions were obtained for the original 3D set of phonon modes. The exact solutions for the correlation functions $\langle \sigma_{\mathrm{eg}}(t) \rangle$ and $\langle \sigma_{\mathrm{eg}}(t+\tau)\sigma_{\mathrm{ge}}(t) \rangle$ may be obtained using a range of different methods, e.g., the Magnus expansion [102, 103], the displacement operator techniques used in appendix E, or the modified QRT derived in section 2.3.2, which turns out to be exact for the IBM. For the one-time function, the result is

$$\langle \sigma_{\mathrm{eg}}(t)\rangle = \langle \sigma_{\mathrm{eg}}(0)\rangle \exp\left[f(t)\right], \tag{4.47}$$

while the two-time function becomes

$$\langle \sigma_{\mathrm{eg}}(t+\tau)\sigma_{\mathrm{ge}}(t)\rangle = \langle \sigma_{\mathrm{ee}}(0)\rangle \exp\left[f(\tau) + 2i\mathrm{Im}\left\{\varphi(t) - \varphi(\tau+t)\right\}\right], \tag{4.48}$$

where we defined the common function

$$f(t) = i(\omega_{\mathrm{eg}} - \omega_{\mathrm{pol}})t - \varphi(0) + \varphi(t). \tag{4.49}$$

Here the polaron shift is given by $\omega_{\mathrm{pol}} = \sum_{\boldsymbol{k}} |M^{\boldsymbol{k}}|^2/(\hbar^2\omega_{\boldsymbol{k}})$ and the phonon correlation function $\varphi(t)$ is defined in eq. (E.22). We find excellent agreement between the analytical results based on the original 3D modes and our numerical results based on the effective 1D modes.

4.3 Results

In this section we present simulations of the single-photon indistinguishability with the main focus on the ED approach presented above. The governing EOM is

$$\partial_t \rho(t) = -i\hbar^{-1}\left[H, \rho(t)\right] + S_{\mathrm{L}}\rho(t), \tag{4.50}$$

where the Hamiltonian contains the effective phonon modes as described by eq. (4.29) and Lindblad population decay terms have been included as

$$S_{\mathrm{L}}\rho(t) = (L_{\kappa}\left\{a\right\} + L_{\Gamma}\left\{\sigma_{\mathrm{eg}}\right\})\rho(t). \tag{4.51}$$

This models the system presented in section 3.1, with the exception that Markovian pure dephasing is not included in eq. (4.50). For comparison we include simulations based on two alternative approaches for including the effect of phonons.

The first approach is the second order TCL in the original frame, described in section 3.2.4, with the RDM $\bar{\rho}(t) = \mathrm{Tr}_{\mathrm{phon}}\left[R_{\mathrm{phon}}\rho(t)\right]$, where phonons are treated as a reservoir. The EOM is

$$\partial_t \bar{\rho}(t) = -i\hbar^{-1}\left[H_{\mathrm{JC}}, \bar{\rho}(t)\right] + S_{\mathrm{TCL}}(t)\bar{\rho}(t) + S_{\mathrm{L}}\bar{\rho}(t). \tag{4.52}$$

The unitary Hamiltonian only includes the Jaynes-Cummings contributions from eq. (4.29) and $S_{\mathrm{TCL}}(t)\bar{\rho}(t)$ contains the phonon induced scattering terms described in detail in section 3.2.4. We take the long-time limit in the TCL terms, $S_{\mathrm{TCL}}(t \to \infty)$, for two reasons. The first reason is that this places us in the long-time non-Markovian regime, see the discussion in section 2.2.3, where short-time non-Markovian effects are neglected and hence, through a comparison with the ED approach, we can estimate the importance of the short-time non-Markovian regime. The second reason is to compare to commonly used approaches in literature, where the long-time limit is used almost exclusively

[56, 69, 104, 105]. It should be noted that the cited literature all employ the polaron transformation, see sections 3.1.3 and 3.2.5, however for low temperatures we expect the results obtained in the original and polaron frame to be comparable. As discussed in section 3.2.5, the polaron transformation implies that the expectation value of any system operator can not necessarily be calculated using the resulting RDM, without additional approximations. This stems from the lack of invariance of certain operators under the polaron transformation [52], an issue which our model in the original frame does not suffer from.

The second alternative approach that we consider, models phonons by including a phenomenological pure dephasing rate and is by far the most used method in the cQED literature [39, 41, 40]. Here the TCL term from eq. (4.52) is replaced by the Lindblad term $L_{2\gamma}\left\{\sigma_{\mathrm{ee}}\right\}$, which leads to the EOM

$$\partial_t \bar{\rho}(t) = -i\hbar^{-1}\left[H_{\mathrm{JC}}, \bar{\rho}(t)\right] + L_{2\gamma}\left\{\sigma_{\mathrm{ee}}\right\}\bar{\rho}(t) + S_{\mathrm{L}}\bar{\rho}(t). \tag{4.53}$$

The pure dephasing rate γ enters in this theory as a parameter with no *a priori* value, hence we choose the pure dephasing rate to provide a reasonable fit to the ED in the simulations to follow.

With the three different models presented above we cover all three regimes of non-Markovianity discussed in section 2.2.3. The ED approach describes both the short-time and long-time non-Markovian regimes, whereas the long-time limit of the TCL only captures effects in the energy-conserving long-time non-Markovian regime, and finally the Lindblad pure dephasing approach assumes the phonon reservoir to be completely memory-less and hence provides a description in the Markovian limit.

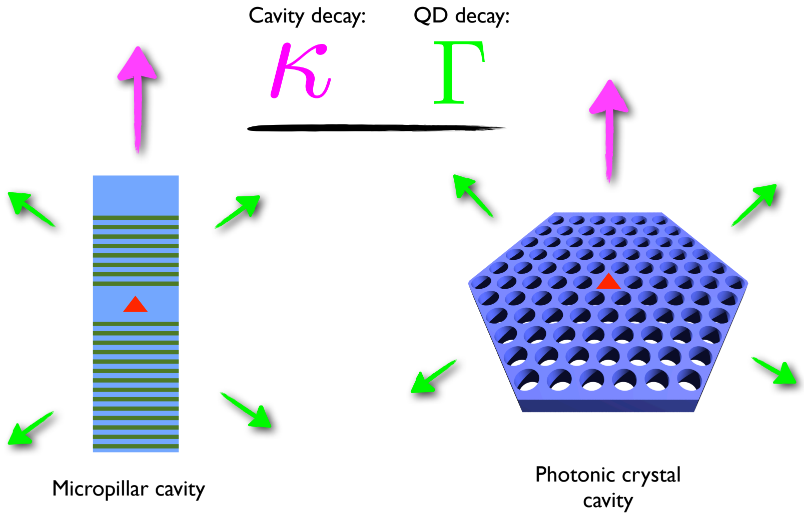

Figure 4.6: Schematic illustrations of idealized spatial directions of emission from the QD, Γ channel, and from the cavity, κ channel, for a photonic crystal crystal and a micropillar cavity.

In cQED models it is usually assumed that energy can decay from the system either via photons escaping from the cavity, by a rate κ, or by direct decay of the QD through radiative or non-radiative processes, by a rate Γ, see section 3.1.1 for a schematic illustration. These two decay channels provide the light emission measured in an experiment and are typically assumed to be associated with certain spatial directions relative to the experimental sample, see illustration in fig. 4.6 for a photonic crystal cavity and a micropillar cavity. In the case of a microscopic treatment of phonons also phonon emission can carry away energy, which is not the case for a pure dephasing rate treatment of decoherence. However, it is not very well understood to which degree and under which conditions, the emission from the cavity and QD mix and interfere with each other. For this reason, it is important to investigate the indistinguishability of photons emitted both from the cavity and the QD. This can be achieved by choosing $A = a$ (photon annihilation operator) for cavity emission and $A = \sigma_{\mathrm{ge}}$ (QD de-excitation operator) for QD emission in using eq. (4.13).

As for the initial condition, we choose the QD to be in the excited state and both the photon and phonon fields in their respective vacuum states. This models the experimental situation corresponding to excitation of the QD using a short optical pulse, with a duration smaller than any other timescale in the system. Initiating the phonons in the vacuum state corresponds to a temperature of zero in the phonon reservoir, hence no phonons are thermally excited. From section 3.3 we know that $T = 0$ K has the consequence that only phonon emission processes will initially be available, and thus we expect the present initial state to describe the fundamental limitation imposed by the phonon interaction on indistinguishability. Raising the temperature just a few degrees above zero dramatically increases the number of phonon states to be included in the ED approach and we limit ourselves to zero temperature. We note that this is not a fundamental limitation of the ED approach and more sophisticated cut-off schemes could possibly remedy this practical limitation.

To obtain an effective QD-cavity detuning equal to zero, we counteract the polaron energy shift induced by the phonons, eq. (4.47), by choosing the QD-cavity detuning equal to the polaron shift $\hbar\Delta = \hbar\omega_{\mathrm{pol}} \approx 27.78\ \mu\mathrm{eV}$.

The typical number of included phonon modes in the ED approach was 30 to 50, with up to 2 phonon excitations in each mode, which resulted in 200 to 500 phonon states. Through sampling of the 3 phonon excitation space, we estimate an error of at most 0.1 percent in fig. 4.7 and at most 1 percent in fig. 4.11.

4.3.1 Dependence on QD-cavity coupling strength

In fig. 4.7 we show the indistinguishability for light emitted from both the QD and the cavity as a function of the QD-cavity coupling strength, g, for the three different approaches discussed above. We have chosen system parameters corresponding to a typical experimental cQED system and vary g from small values [70], corresponding to the weak coupling regime, through intermediate values, and to large values that place the system in the strong coupling regime, observed in state-of-the-art samples [74]. Increasing the QD-cavity coupling from a value of $g = 0$ we observe a pronounced increase in indistinguishability for the ED and Lindblad approaches, while the TCL starts out at unity

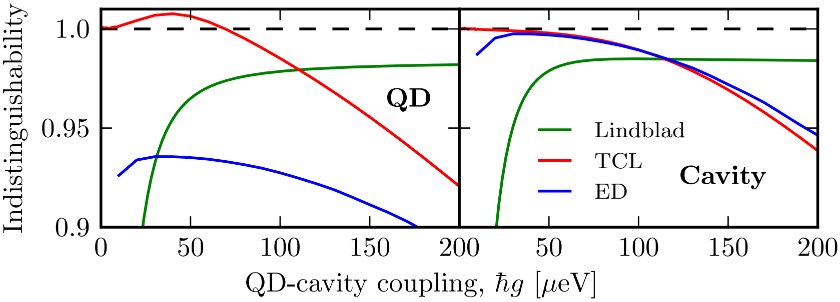

Figure 4.7: Calculated indistinguishability as a function of the QD-cavity coupling strength for light emitted from the QD and the cavity. Parameters: $\Gamma = 0.5$ *ns*$^{-1}$, $\hbar\kappa = 125$ μ*eV,* $\hbar\Delta = 27.78$ μ*eV, and* $\hbar\gamma = 0.85$ μ*eV.*

or even slightly above. The above-unity indistinguishability predicted by the TCL in the QD case is unphysical and is expected to arise as the TCL in general does not conserve the positivity of the RDM, see discussion in the end of section 2.2.1. As we further increase g, the ED predicts a clear maximum in the indistinguishability, followed by a steep decrease for both the ED and TCL results. In stark contrast to this behavior, the commonly used Lindblad approach does not predict a decrease in indistinguishability, merely a saturation as the QD-cavity coupling is increased. The emergence of a pronounced maximum is an important and surprising prediction of the ED and will be especially important in experiments where a high indistinguishability is needed, e.g., in experiments implementing linear quantum computing protocols [1].

The qualitative behavior of the Lindblad approach can understood using eq. (4.18), which we reiterate

$$I = \frac{\Gamma_{\text{eff}}}{\Gamma_{\text{eff}} + 2\gamma}, \tag{4.54}$$

where, in the weak coupling regime, an explicit expression for Γ_{eff} may be obtained

$$\Gamma_{\text{eff}} = \Gamma + 2g^2 \frac{\gamma_{\text{tot}}}{\gamma_{\text{tot}}^2 + \Delta^2}, \quad \gamma_{\text{tot}} = \frac{1}{2}(\kappa + \Gamma) + \gamma. \tag{4.55}$$

This expression predicts an initial increase in indistinguishability as g is increased, due to the Purcell enhancement off the effective QD decay rate. However, as we enter the strong coupling regime near $\hbar g \approx 100$ μeV, the Purcell effect no longer decreases the effective QD lifetime, leading to a saturation of the indistinguishability. It is clear that the simple expression for the indistinguishability derived using the phenomenological Lindblad theory can not explain the behavior displayed by the ED and TCL approaches, upon variation of g.

To facilitate the interpretation of the results obtained in the microscopic ED and TCL approaches, it is useful to rewrite the Hamiltonian, eq. (4.29),

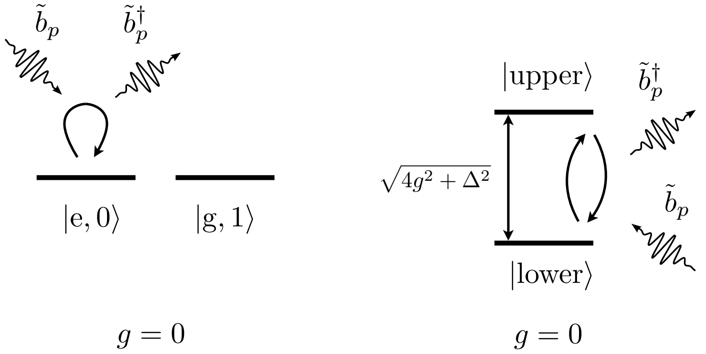

Figure 4.8: (left) Illustration of the effect of phonons for a purely virtual interaction, i.e. when $g=0$, (right) contrasted to the polariton dressed case, $g \neq 0$, where the phonons cause real transitions. In both cases we assume $\Delta = 0$ for simplicity.

in terms of polariton (dressed) states that diagonalize the Jaynes-Cummings Hamiltonian, eq. (4.20). The result is

$$\begin{aligned} H' = {} & \hbar\omega_\mathrm{u}\sigma_\mathrm{uu} + \hbar\omega_\mathrm{l}\sigma_\mathrm{ll} + \sum_p \hbar\omega_p \tilde{b}_p^\dagger \tilde{b}_p \\ & + \left[A_\mathrm{uu}\sigma_\mathrm{uu} + A_\mathrm{ll}\sigma_\mathrm{ll} + A_\mathrm{ul}\sigma_\mathrm{ul} + A_\mathrm{lu}\sigma_\mathrm{lu}\right] \sum_p \tilde{M}_p(\tilde{b}_p^\dagger + \tilde{b}_p), \end{aligned} \tag{4.56}$$

where the polariton energies of the upper (u) and lower (l) branches are

$$\omega_\mathrm{u/l} = \frac{\Delta \pm \sqrt{4g^2+\Delta^2}}{2} \tag{4.57}$$

with respective eigenvectors

$$|\mathrm{b}\rangle = N_\mathrm{b}\left[\omega_\mathrm{b}\,|\mathrm{e}, n=0\rangle + g\,|\mathrm{g}, n=1\rangle\right],\ N_\mathrm{b} = \left[\omega_\mathrm{b}^2 + g^2\right]^{-1/2}, \tag{4.58}$$

written in terms of the excited QD, $|\mathrm{e}, n=0\rangle$, and excited cavity, $|\mathrm{g}, n=1\rangle$, states and where $\mathrm{b} = \mathrm{u}, \mathrm{l}$. The A_pq elements are

$$A_\mathrm{uu} = N_\mathrm{u}^2\omega_\mathrm{u}^2 = \frac{\omega_\mathrm{u}^2}{\omega_\mathrm{u}^2 + g^2},\ A_\mathrm{ll} = N_\mathrm{l}^2\omega_\mathrm{l}^2 = \frac{\omega_\mathrm{l}^2}{\omega_\mathrm{l}^2 + g^2}, \tag{4.59}$$

$$A_\mathrm{lu} = A_\mathrm{ul} = N_\mathrm{u}\omega_\mathrm{u}N_\mathrm{l}\omega_\mathrm{l} = \frac{\omega_\mathrm{u}\omega_\mathrm{l}}{\sqrt{\omega_\mathrm{u}^2+g^2}\sqrt{\omega_\mathrm{l}^2+g^2}}. \tag{4.60}$$

In the original representation, eq. (4.29), the phonons interacted with the excited state of the QD through the operator σ_ee in a purely virtual fashion, i.e., where phonon processes take the QD from $|\mathrm{e}\rangle$ and back to the same state. However, in the polariton representation the effect of the coupling to the cavity on the electron-phonon interaction becomes much more clear. Importantly, we observe that as A_lu and A_ul are in general non-zero, the phonons can cause transitions between the two different branches of the polariton. The energy separation between the upper and lower branches, $\omega_{\mathrm{u}} - \omega_{\mathrm{l}} = \sqrt{4g^2 + \Delta^2}$, is therefore expected to play an important role in understanding the effect of phonons on the physics. This is illustrated in fig. 4.8 and compared to the (virtual) $g = 0$ case. In fig. 4.9(a) we show pure dephasing rates calculated within the TCL, more specifically $\gamma_{13}(t)$ [see eqs. (3.28) and (3.32)], for a small and a large value of the QD-cavity coupling strength g. We also show in fig. 4.9(b) the corresponding effective phonon density, eq. (3.56), defined as

$$d_{\mathrm{ph}}(\omega) = \pi \sum_p |\tilde{M}_p|^2 \left[(n_p + 1)\delta(\omega - \omega_p) + n_p \delta(\omega + \omega_p) \right], \tag{4.61}$$

where the thermal occupation factor n_p is zero for $T = 0$ K.

For both values of g, the pure dephasing rate shown in fig. 4.9(a) attains large values within the first few ps after the initial excitation, after which it settles to a positive non-zero value in the long-time limit. The initial temporal variations of the pure dephasing rate are directly related to a sampling of the entire effective phonon spectrum, shown in fig. 4.9(b), through virtual processes, see fig. 4.8, which are allowed for short times due to the energy-time uncertainty relation. These virtual processes are a hallmark of the short-time non-Markovian regime and give rise to the well-known phonon sidebands in the spectral domain [33] and emission of a phonon wavepacket in the spatial domain [98], as discussed further below. In the long-time limit, where energy conservation must be enforced, sustained phonon decoherence reflects real phonon-mediated transitions, fig. 4.8, corresponding to the effective phonon density being sampled at the transition energy of these transitions. This explains why the long-time value of the dephasing rate is much larger for $\hbar g = 200$ μeV compared to $\hbar g = 30$ μeV. The phonon density is thus sampled, respectively, at the energies given by the polariton transitions, namely $\hbar(\omega_{\mathrm{u}} - \omega_{\mathrm{l}}) = 2 \times 30$ $\mu\mathrm{eV} = 0.06$ meV, where the phonon density is small, and $\hbar(\omega_{\mathrm{u}} - \omega_{\mathrm{l}}) = 2 \times 200$ $\mu\mathrm{eV} = 0.4$ meV, where it is much larger. The TCL only considers the long-time limit of the dephasing rate in fig. 4.9(a), hence explaining why the indistinguishability tends to unity for small QD-cavity coupling strengths as observed in fig. 4.7. For a more complete analysis, also the behavior of the phonon-induced rates $\mathcal{G}^{\gtrless}(t)$, section 3.2.4, should be investigated, since a non-zero imaginary part of these rates gives rise to excitation-induced dephasing, which for some parameters dominate over the pure dephasing rate discussed above.

To verify the intuitive explanation provided by the polariton picture, we show in fig. 4.9(c) and (d) the phonon population distribution function, $\langle \tilde{b}_p^\dagger \tilde{b}_p \rangle(t)$, calculated using the ED. For small QD-cavity coupling strength we observe that no specific phonon energy is singled out, consistent with the small phonon density at the corresponding energy of 0.06 meV. However, for the larger QD-cavity coupling strength a significant increase in phonon population occurs near 0.4 meV, as expected from the polariton interpretation. For both values of the QD-cavity coupling we observe an underlying pattern in the phonon distribution function, which is related to virtual processes in the short-time regime. However, for the large coupling an additional modulation is present, occurring periodically in time, which has the effect of suppressing the underlying pattern.

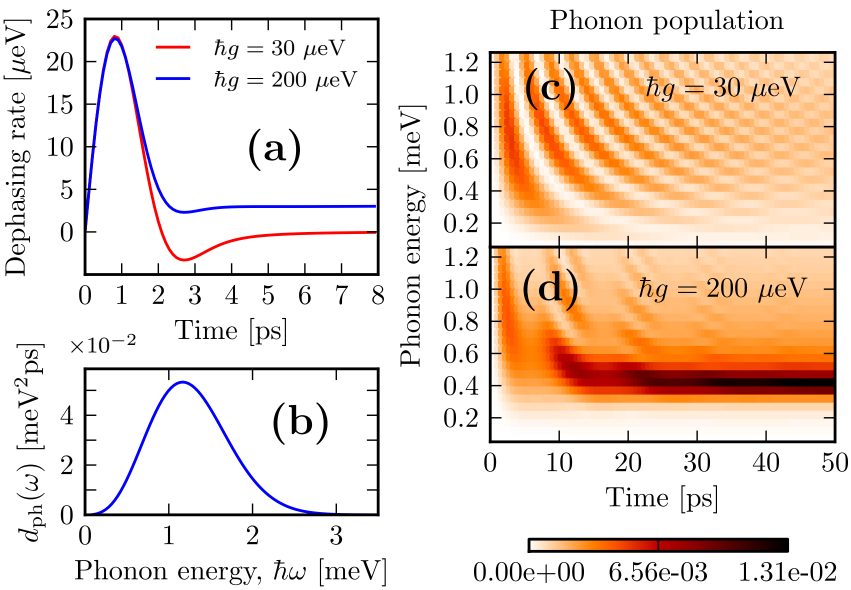

Figure 4.9: ***(a)*** *Time-dependent dephasing rate from the TCL.* ***(b)*** *Effective phonon density at zero temperature.* ***(c)*** *Phonon population distribution function for $\hbar g = 30\ \mu eV$, $\Gamma = 0.5\ ns^{-1}$, $\hbar\kappa = 125\ \mu eV$, and $\hbar\Delta = 27.78\ \mu eV$.* ***(d)*** *As* ***(c)*** *with $\hbar g = 200\ \mu eV$.*

To investigate the origin of this we show in fig. 4.10 the population dynamics of the QD and cavity, for both values of the QD-cavity coupling, along with the absolute value of the displacement field operator for the phonons in real-space coordinates, given by [106]

$$U(t,r) \propto \sum_{\boldsymbol{k}} \frac{1}{k^{1/2}} e^{i\boldsymbol{k}\cdot\boldsymbol{r}} \langle b_{\boldsymbol{k}}(t)\rangle + c.c. \tag{4.62}$$

$$\propto \int_0^\infty dk k^{1/2} \frac{\sin(kr)}{r} \langle b_k(t)\rangle + c.c. \tag{4.63}$$

$$\approx \sum_{p=0}^{\infty} \Delta k_p k_p^{1/2} \frac{\sin(k_p r)}{r} \langle \tilde{b}_p(t)\rangle + c.c. \tag{4.64}$$

where r is the radial distance from the center of the QD.

For $\hbar g = 30\ \mu$eV, the QD and cavity populations show behavior typical for the weak coupling regime, with a monotonous decay of the QD to its ground state. In the real space, the fast excitation of the QD leads to the emission of a phonon wavepacket, which appears because the QD is excited too fast for the lattice to adiabatically equilibrate itself to the presence of the electron [98]. It reacts by emitting the phonon wavepacket, which carriers quantum information into the reservoir causing decoherence of the QD-cavity system and consequently a lower degree of indistinguishability. After the wavepacket

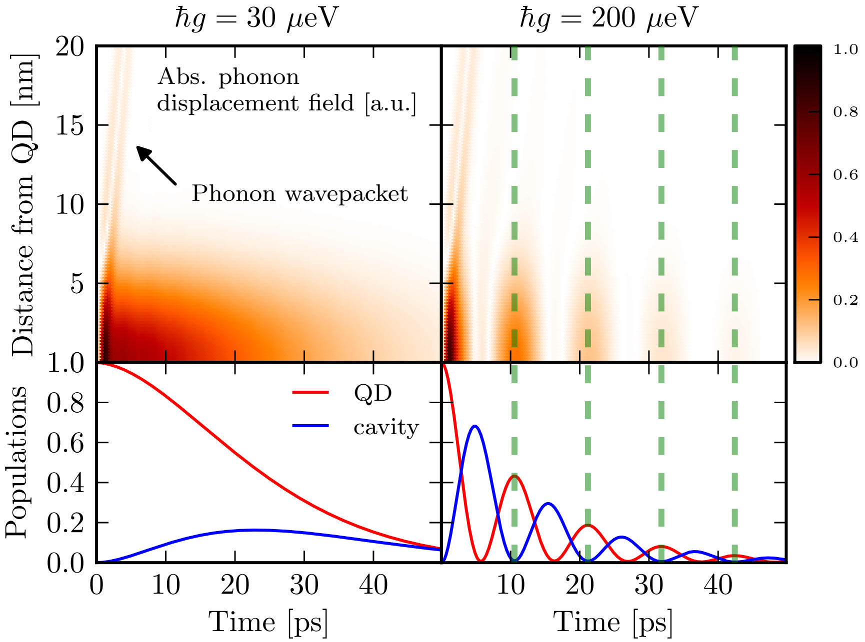

Figure 4.10: (top panels) Absolute value of the phonon displacement field operator, eq. (4.62)*, where the vertical dashed lines indicate the instances where the QD is in its excited state, due to Rabi flopping with the cavity photon. (bottom panels) Corresponding population dynamics for the QD and cavity. Parameters are as in fig. 4.9.*

emission the QD dynamics occurs on a slow enough timescale for the lattice to continuously equilibrate itself and very little quantum information is lost into the reservoir in the form of phonon wavepackets. This is imprinted into the pure dephasing rate in fig. 4.9(a) which shows large values initially (wavepacket emission) and afterward settles to a small positive value (lattice has time to equilibrate).

For $\hbar g = 200\ \mu$eV the dynamics appears qualitatively different, being in the strong coupling regime, the QD and cavity populations display clear Rabi oscillations. The phonon dynamics has also changed markedly, however the initial wavepacket emission is still present. We observe very clearly how the lattice only becomes distorted when the QD is in its excited state, which correlates with the form of the electron-phonon Hamiltonian, eq. (4.29), and gives rise to the modulation in time of the phonon population distribution function observed in fig. 4.9(d). Due to the strong Rabi oscillations exhibited by the QD, the lattice is now forced to distort on significantly faster timescales than was the case in the weak coupling regime discussed above. This leads to the emission of a series of phonon wavepackets, although much smaller than the initial, each time the QD reaches the excited state. Correspondingly, there is a loss of quantum information into the reservoir and a reduction of the indistinguishability. Again, this physical picture is reflected by the pure dephasing rate in fig. 4.9(a), where instead of settling at a low value in the long-time limit as in the case of $\hbar g = 30\ \mu$eV, the continued emission of wavepackets leads to a significant long-time value.

In light of the above analysis, we can now interpret the variation of the indistinguishability with coupling strength seen for the ED approach. The relatively small indistinguishability observed for weak QD-cavity coupling, arises from the complicated phonon dynamics in the short-time regime, where virtual processes dominate the decoherence of the QD-cavity system. This is manifested in the emission of a phonon wavepacket and leads to the large dephasing rate in fig. 4.9(a) for early times. Also, the weak QD-cavity coupling only leads to a small Purcell enhancement, increasing the importance of the strong short-time decoherence even further. Moving toward the maximum in fig. 4.7(c) and (d), real processes become increasingly important and contribute further to the decoherence. However, a stronger Purcell effect combats the influence of decoherence by making the QD decay faster and the indistinguishability increases. Beyond the maximum, the decoherence continues to increase, but the QD-cavity system is now in the strong-coupling regime, leading to a saturation of the Purcell enhancement and the effective decay rate. The increasing decoherence is thus left unopposed and the indistinguishability decreases

Comparing the indistinguishability for the QD and the cavity, only the ED predicts a significant difference between the two. The smaller indistinguishability found for the QD is interpreted as a result of the direct interaction between the QD and the phonon degrees of freedom, as well as the longer lifetime of the QD compared to the cavity, i.e., $1/\Gamma \ggg 1/\kappa$.

4.3.2 Dependence on QD-cavity detuning

In fig. 4.11(a) and (b) we show the indistinguishability as a function of the QD-cavity detuning, Δ, which is an important experimentally controllable parameter. As above, the Lindblad theory is unable to explain the variations with detuning that are predicted by the ED, both on a quantitive and qualitative level. The behavior of the Lindblad theory can again be understood using eq. (4.18), since the Purcell enhancement decreases for increasing detuning thus leading to a lower degree of indistinguishability. A common feature displayed by both the TCL and ED is a strong asymmetry with respect to the sign of the detuning. For large detuning, $|\Delta| \gg g$, the polariton dispersion becomes $\omega_{\mathrm{u/l}} \approx (\Delta \pm |\Delta|)/2$, where the cavity-like branch has the energy ≈ 0 and the QD-like branch has the energy $\approx \Delta$. Thus, to make real transitions between the two polariton branches, the phonons need to provide an energy $\pm\hbar|\Delta|$, through emission $(-)$ or absorption $(+)$ of a phonon, see fig. 4.8. At zero temperature, only phonon emission is possible, illustrated by the effective phonon density infig. 4.9(b) being zero for $\omega < 0$. Only positive detuning will thus lead to decoherence in the long-time limit, and a larger indistinguishability is expected for negative detuning. Indeed, both the TCL and ED display such an asymmetry, except for the QD emission where the TCL breaks down, supposedly because the neglected short-time dynamics is very important in this case.

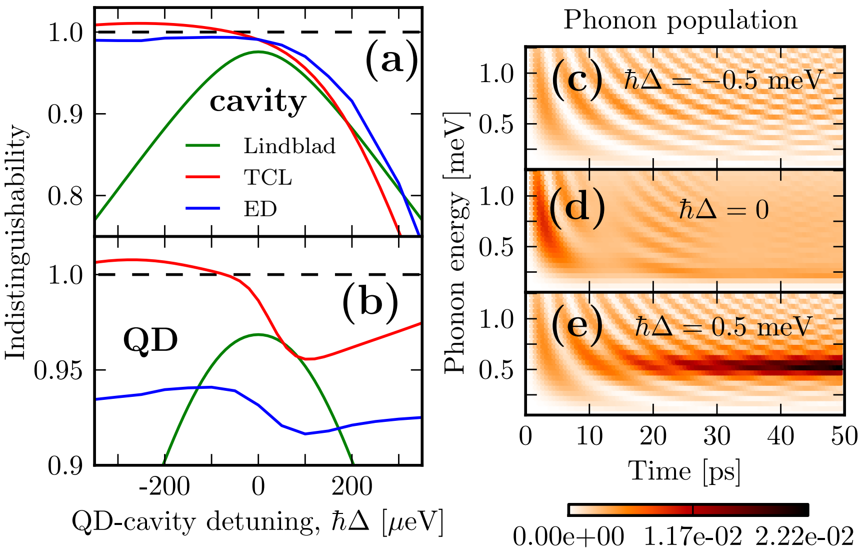

Figure 4.11: ***(a)****,* ***(b)*** *Indistinguishability as a function of QD-cavity detuning for QD and cavity emission.* ***(c)****,* ***(d)****, and* ***(e)*** *Phonon population distribution function for different QD-cavity detuning. For $\Delta = 0$ the population has been scaled by a factor of 2. Parameters: $\hbar\Gamma = 1$ μeV, $\hbar\kappa = 100$ μeV, $\hbar g = 100$ μeV, and $\hbar\gamma = 1.1$ μeV.*

For negative detuning, the effect of virtual processes in the short-time regime is clearly seen in the ED result. Despite the absence of phonon emission in the long-time limit, the indistinguishability still attains values significantly below unity. This is not the case for the TCL, which only describes the long-time limit. The effect of detuning on the phonon population distribution functions is shown in fig. 4.11(c), (d), and (e). We observe that for a detuning of $\hbar\Delta = 0.5$ meV, a significant phonon population is observed at the same phonon energy, consistent with the energy compensation needed for the QD to become resonant with the cavity.

It is interesting to compare the situations where the polariton splitting is mainly determined the QD-cavity detuning, as in fig. 4.11(e), to the case where it is determined by the coherent QD-cavity coupling, as in fig. 4.9(d). In the detuning dominated situation, the phonon dynamics is quite similar to the case of negative detuning, fig. 4.11(c), where the presence of the cavity is insignificant, except that a sharp increase in phonon population near $\hbar\Delta$ is clearly visible [fig. 4.11(e)]. This is in stark contrast to the situation dominated by the coherent coupling. Here a sharp increase is also observed at the polariton transition energy ($2\hbar g$), but, the phonon population is strongly affected at other energies as well. This comparison suggests the following physical picture: For large detuning, where one polariton branch is very QD-like, i.e. basically decoupled from the cavity, both the cavity and phonons act as reservoirs for the

QD and the dynamics is relatively simple. However, once the coherent coupling dominates the polariton splitting, the quasi-particle nature of the QD-cavity system becomes essential in interpreting the dynamics of the system.

4.4 Summary

In this chapter we investigated the influence of the phonon interaction on the indistinguishability of single photons emitted from semiconductor cQED structures.

We discussed the important relation between coherence and two-photon interference experiments, which can be used to quantify the degree of indistinguishability. More specifically, the Hong-Ou-Mandel (HOM) experiment was discussed in detail and an expression for the second order HOM correlation function, describing the number of coincidence events in the beam-splitter output arms, was derived. Using the HOM correlation function, the degree of indistinguishability was defined as the total number of coincidence events normalized by the number of events in the absence of interference.

This definition requires knowledge of the two-time correlation function of the photon field. It was discussed how two-time functions in general can be expected to much more sensitive to the presence of a non-Markovian reservoir, compared to the corresponding one-time functions. The determination of two-time functions in the presence of non-Markovian reservoirs is beyond the commonly used Quantum Regression Theorem (QRT), hence we developed an alternative method based on an exact diagonalization (ED) procedure to rigorously include non-Markovian effects. The ED approach is based on employing a set of effective phonon modes. We gave a detailed account of the derivation of these modes and of the ensuing cut-off scheme used for selecting the most important phonon states.

The dependence of indistinguishability on important cQED parameters was investigated using the ED approach and compared to two standard approaches for including phonon effects in cQED. These include a microscopic second order treatment based on the long-time limit of the time-convolutionless (TCL) method and a purely phenomenological approach including pure dephasing processes in the Markovian Lindblad formalism. We calculated the indistinguishability as a function of the QD-cavity coupling strength and found a surprising maximum, situated in between the weak and strong coupling regimes. Importantly, the maximum was not predicted by either the TCL or the Lindblad based methods, indicating the importance of including memory effects in the short-time non-Markovian regime as provided by the ED approach. This result was interpreted using a polariton (dressed) based representation, where the energy splitting between the two polariton branches was found to play an essential role in understanding the physics.

The dependence on QD-cavity detuning was also investigated and a strong asymmetry with respect to the sign of the detuning was found. This is in agreement with the results of the previous chapter, and was in analogy explained as arising from the absence of thermal phonons available for absorption processes.

Chapter 5

Highlights and outlook

In this thesis we have investigated the influence of the electron-phonon interaction on QD decay dynamics and the indistinguishability of single photons. These subjects were treated in individual chapters, which themselves have a summary and conclusion section, so rather than repeating these, we will present a few highlights and provide an outlook for future work.

Highligths

The main result obtained in relation to QD decay dynamics was the derivation of an approximate analytical expression for the total QD decay rate in the presence of the phonon interaction, see eq. (3.58), which predicts what might be coined a phonon-assisted Purcell effect. It illustrates how the availability of a cavity resonance may enhance the usually very weak phonon sidebands and give rise to a surprisingly strong effect on the far-detuned QD decay rate. The expression separates the effect of phonons from the physics of the standard coupled QD-cavity cQED system in a clear way and emphasizes the important role played by the effective phonon density. The density is shown to be probed at the spectral position given by the QD-cavity detuning, which yields a pronounced asymmetry with respect to detuning in the low temperature regime. Furthermore, the expression explains the apparent absence of phonon effects in certain cavity structures, as caused by a sensitive dependence on the background decay rate of the QD, where a large value may mask the effect of phonons.

One of the main results in relation to single-photon indistinguishability was the prediction of a maximum degree of indistinguishability as a function of QD-cavity coupling strength. The maximum is surprising as it is not predicted by either the Markovian Lindblad theory or the microscopic non-Markovian time-convolutionless (TCL) theory, taken in the long-time limit. This shows that in order to model indistinguishability one must account for the full non-Markovian nature of the phonon interaction, including dynamics in the short-time regime which is not included in standard open system approaches. This prediction was made possible by the development of a model that treats the electron-phonon coupling to all orders and hence provides a numerically exact solution of the coupled electron-photon-phonon system.

An important conclusion to be drawn from this thesis relates to the special situation arising in semiconductor cQED, where one may simultaneously have highly structured reservoirs, e.g. phonons, and strong internal coupling mechanisms, leading to the formation of quasi-particles, e.g. polaritons. In this unique setting, the influence of the reservoir can no longer be considered as something fixed. Rather, it becomes imperative to include both the memory of the reservoir and the internal structure of the system interacting with the reservoir, when describing the reduced dynamics of the small system.

Outlook

Most endeavors in science end up raising more questions than they answer. The work presented in this thesis is no exception. Especially the work on indistinguishability turned out to be more challenging and yielded more surprises than originally expected. As this work was carried out in the last part of the project, naturally it left more unanswered questions and loose ends than the work on QD decay dynamics. Below we present a list of items that would be interesting to pursue in future work on single-photon indistinguishability.

- While we employed the all-numerical ED approach for investigating indistinguishability, the non-Markovian corrections to the QRT derived in section 2.3.2 would be expected to yield accurate results for the weak electron-phonon coupling found InGaAs systems. As demonstrated in the chapter on QD decay dynamics, it is sometimes possible to obtain approximate results that yield much more physical insight than any numerical experiment, like the ED approach, ever could. Motivated by this, investigating indistinguishability using the results of section 2.3.2 could prove valuable, while using the ED approach as a guideline when performing approximations.

- In this work we have mostly covered the physics of single-photon indistinguishability, however, for real applications a very high degree of indistinguishability is needed. Achieving this would probably require an optimization of the indistinguishability through an a minimization of the detrimental effects of the phonon interaction. This kind of optimization could be pursued using the tools presented in this thesis.

- While we were able to systematically avoid the unphysical solutions emerging from the ED for certain parameters values, it would be preferable to obtain a better understanding of the phenomena, to possibly devise a way to avoid it completely.

- As shown in chapter 4 the degree of indistinguishability of photons emitted from the QD and the cavity decay channels varied strongly. In a theoretical treatment this poses no particular problem, however in experiment one would measure a mix of the two decay channels and presumably the measured indistinguishability would depend strongly on the spatial position of the detector. To perform an accurate quantitative comparison between theory and experiment, a better understanding of the far-field emission pattern of from cQED structures is expected to be needed. This, especially, holds true in the strong coupling regime where individual spectral features can no longer be assigned to either QD or cavity.

- An important assumption for obtaining a simple description of the reduced dynamics is an initial density matrix factorized into a system and reservoir part. While relaxing this assumption would be cumbersome for the reduced density matrix (RDM), it would be straight-forward in ED approach as one deals with the total density matrix anyway and could lead to important effects.

- In this thesis we investigated single-photon indistinguishability at zero temperature, expected to yield the fundamental limit of phonon effects. However, all experiments are carried out at finite temperatures, hence it would be interesting to study this situation. Finite temperatures could easily be investigated in an implementation of the non-Markovian QRT or an optimized version of the ED approach.

Appendix A

Acronyms

BS beam-splitter 61

CF correlation function 66

cQED cavity quantum electrodynamics 2

ED exact diagonalization 67

EOM equation(s) of motion 5

HOM Hong-Ou-Mandel 61

QRT Quantum Regression Theorem 4

RDM reduced density matrix 4

RHS right hand side 19

SPS single-photon source 2

td time-dependent

TCL time-convolutionless 4

te time-evolution

TEO time-evolution operator 6

tid time-independent

Appendix B

The simplified Hamiltonian

In this appendix we will describe the steps needed to obtain the Hamiltonian used in the main text, starting from a more fundamental Hamiltonian. The fundamental Hamiltonian is given by

$$H = H_{\mathrm{s}} + H_{0,\mathrm{ph}} + H_{\mathrm{e-ph}} + H_{\gamma} + H_{\kappa} + H_{\Gamma}. \tag{B.1}$$

The part governing the QD-cavity system is

$$H_{\mathrm{s}} = \hbar\omega_{\mathrm{g}} c_{\mathrm{g}}^{\dagger} c_{\mathrm{g}} + \hbar\omega_{\mathrm{e}} c_{\mathrm{e}}^{\dagger} c_{\mathrm{e}} + \hbar\omega_{\mathrm{cav}} a^{\dagger} a + \hbar g (a^{\dagger} c_{\mathrm{g}}^{\dagger} c_{\mathrm{e}} + c_{\mathrm{e}}^{\dagger} c_{\mathrm{g}} a). \tag{B.2}$$

The free phonon Hamiltonian is

$$H_{0,\mathrm{ph}} = \sum_{\boldsymbol{k}} \hbar\omega_{\boldsymbol{k}} b_{\boldsymbol{k}}^{\dagger} b_{\boldsymbol{k}}. \tag{B.3}$$

The interaction between the electrons and the phonons is

$$H_{\mathrm{e-ph}} = \sum_{\boldsymbol{k}} \left(M_{\mathrm{gg}}^{\boldsymbol{k}} c_{\mathrm{g}}^{\dagger} c_{\mathrm{g}} + M_{\mathrm{ee}}^{\boldsymbol{k}} c_{\mathrm{e}}^{\dagger} c_{\mathrm{e}} \right) (b_{-\boldsymbol{k}}^{\dagger} + b_{\boldsymbol{k}}). \tag{B.4}$$

The last three contributions H_{γ}, H_{κ}, and H_{Γ} refer to different reservoirs and their interaction with the system, giving rise to various forms of Markovian decay, which are introduced in the main paper. Their explicit forms are not needed and will therefore not be discussed further in this appendix. For an elaboration on the above Hamiltonians see the main text section 3.1.1.

We only consider a single electron in the system, hence the following relation holds

$$c_{\mathrm{g}}^{\dagger} c_{\mathrm{g}} + c_{\mathrm{e}}^{\dagger} c_{\mathrm{e}} = 1, \tag{B.5}$$

which may be used to eliminate the ground state operator $c_{\mathrm{g}}^{\dagger} c_{\mathrm{g}}$ from the Hamiltonian. Physically, this elimination can be motivated by the fact that we only have one electron in two levels, implying a perfect correlation between the two electronic states and hence it is sufficient to treat one of the levels explicitly. For reasons to be elaborated below we choose the excited state.

The elimination results in the following changes

$$H_\mathrm{s} = \hbar\omega_\mathrm{eg} c_\mathrm{e}^\dagger c_\mathrm{e} + \hbar\omega_\mathrm{cav} a^\dagger a + \hbar g (a^\dagger c_\mathrm{g}^\dagger c_\mathrm{e} + c_\mathrm{e}^\dagger c_\mathrm{g} a), \tag{B.6}$$

where a constant energy term has been removed and we introduced the transition frequency of the QD defined as $\omega_\mathrm{eg} = \omega_\mathrm{e} - \omega_\mathrm{g}$. Furthermore we get

$$H_\mathrm{e-ph} = \sum_{\boldsymbol{k}} M^{\boldsymbol{k}} (b_{-\boldsymbol{k}}^\dagger + b_{\boldsymbol{k}}) c_\mathrm{e}^\dagger c_\mathrm{e} + \sum_{\boldsymbol{k}} M_\mathrm{gg}^{\boldsymbol{k}} (b_{-\boldsymbol{k}}^\dagger + b_{\boldsymbol{k}}), \tag{B.7}$$

where we have introduced an effective interaction matrix element as $M^{\boldsymbol{k}} = M_\mathrm{ee}^{\boldsymbol{k}} - M_\mathrm{gg}^{\boldsymbol{k}}$ and the last term without any electron operators corresponds to the phonon interaction with the fully occupied ground state. In thermal equilibrium, before any excitation of the system, the QD is in its ground state and the phonon system is in an equilibrium state that takes into account the presence of the electron in the ground state. We wish to describe a situation that deviates from this thermal equilibrium and therefore it would be advantageous to take into account the phonon interaction with the fully occupied ground state from from very beginning. This may be achieved by shifting the phonon operators [107] through a unitary transformation defined as

$$b_{\boldsymbol{k}} \to e^S b_{\boldsymbol{k}} e^{-S}, \quad S = \sum_{\boldsymbol{k}} \frac{M_\mathrm{gg}^{\boldsymbol{k}}}{\hbar\omega_{\boldsymbol{k}}} (b_{-\boldsymbol{k}}^\dagger - b_{\boldsymbol{k}}). \tag{B.8}$$

This transformation only affects the phonon operators and leads to the substitution in the total Hamiltonian

$$b_{\boldsymbol{k}} \to b_{\boldsymbol{k}} - \frac{M_\mathrm{gg}^{-\boldsymbol{k}}}{\hbar\omega_{\boldsymbol{k}}}. \tag{B.9}$$

This removes the last term in eq. (B.7) and introduces a new term given by

$$-\sum_{\boldsymbol{k}} \left[2M^{\boldsymbol{k}} M_\mathrm{gg}^{-\boldsymbol{k}}\right] / \left[\hbar\omega_{\boldsymbol{k}}\right] c_\mathrm{e}^\dagger c_\mathrm{e}, \tag{B.10}$$

which yields a simple energy renormalization that can be absorbed into the bare excited state energy $\hbar\omega_\mathrm{e}$.

For describing single photon emission it is sufficient to operate in a one-excitation subspace of the QD-cavity Hilbert space. As a specific basis for this we choose the following: $\{|1\rangle = |\mathrm{e}, n=0\rangle, |2\rangle = |\mathrm{g}, n=1\rangle, |3\rangle = |\mathrm{g}, n=0\rangle\}$. Along with the reformulations introduced above, projecting the second quantized Hamiltonian on to this subspace changes the following parts of the total Hamiltonian defined in eq. (B.1)

$$H_\mathrm{s} = \hbar\omega_\mathrm{eg}\sigma_{11} + \hbar\omega_\mathrm{cav}\sigma_{22} + \hbar g(\sigma_{12} + \sigma_{21}), \tag{B.11}$$

$$H_\mathrm{e-ph} = B\sigma_{11}, \tag{B.12}$$

where $B = \sum_{\boldsymbol{k}} M^{\boldsymbol{k}} (b_{-\boldsymbol{k}}^\dagger + b_{\boldsymbol{k}})$ and $\sigma_{pq} = |p\rangle\langle q|$.

To simplify the equations, the QD-cavity detuning $\Delta = \omega_\mathrm{eg} - \omega_\mathrm{cav}$ can be introduced into eq. (B.11). This can be achieved by moving into a rotating frame described by the unitary operator $T(t) = \exp(-i\omega_{\mathrm{cav}}[\sigma_{11} + \sigma_{22}]t)$, using this in conjunction with eqs. (2.18) and (2.19) we obtain

$$H_{\mathrm{s}} = \hbar\Delta\sigma_{11} + \hbar g(\sigma_{12} + \sigma_{21}). \tag{B.13}$$

Appendix C

The polaron transformed Hamiltonian

In this appendix we will apply the polaron transformation to the total Hamiltonian.

The total Hamiltonian presented in appendix B contains contributions from reservoirs needed to include the Markovian decays. For the final equations the decay terms arising from these Hamiltonians will, however, not be affected by the polaron transformation we perform in this appendix and they will be omitted in the following. We explicitly demonstrate this in appendix D. The Hamiltonian is

$$H = \hbar\Delta\sigma_{11} + \hbar g(\sigma_{12} + \sigma_{21}) + \sigma_{11}\sum_{\boldsymbol{k}} M^{\boldsymbol{k}}(b^\dagger_{-\boldsymbol{k}} + b_{\boldsymbol{k}}) + \sum_{\boldsymbol{k}} \hbar\omega_{\boldsymbol{k}} b^\dagger_{\boldsymbol{k}} b_{\boldsymbol{k}}. \tag{C.1}$$

The transformation we apply is known as the polaron transformation [52, 53, 54, 56] and is defined in the following way

$$\bar{O} = e^S O e^{-S} \tag{C.2}$$

where

$$S = \sigma_{11} C, \tag{C.3}$$

$$C = \sum_{\boldsymbol{k}} \lambda_{\boldsymbol{k}}(b^\dagger_{-\boldsymbol{k}} - b_{\boldsymbol{k}}), \quad \lambda_{\boldsymbol{k}} = \frac{M^{\boldsymbol{k}}}{\hbar\omega_{\boldsymbol{k}}}. \tag{C.4}$$

For performing the transformation we employ the Baker-Campbell-Hausdorff formula which states

$$\bar{O} = e^S O e^{-S} = O + [S, O] + \frac{1}{2!}[S, [S, O]] + \frac{1}{3!}[S, [S, [S, O]]] + \cdots \tag{C.5}$$

The transformed operators are:

$$\bar{\sigma}_{11} = \sigma_{11}, \quad \bar{\sigma}_{12} = \sigma_{12} e^C, \quad \bar{b}_{\boldsymbol{k}} = b_{\boldsymbol{k}} - \lambda_{-\boldsymbol{k}}\sigma_{11}. \tag{C.6}$$

Inserting these expressions and simplifying the resulting Hamiltonian yields

$$\bar{H} = \hbar\Delta\sigma_{11} + \hbar g(\sigma_{12}X_+ + \sigma_{21}X_-) + \sum_{\boldsymbol{k}} \hbar\omega_{\boldsymbol{k}} b_{\boldsymbol{k}}^\dagger b_{\boldsymbol{k}}, \tag{C.7}$$

where the detuning has been redefined as

$$\Delta \to \Delta - \sum_{\boldsymbol{k}} |M^{\boldsymbol{k}}|^2/(\hbar^2\omega_{\boldsymbol{k}}) \tag{C.8}$$

to take into account the so-called polaron shift of the $|1\rangle$ state and further we introduced the phonon operators

$$X_\pm = e^{\pm C}. \tag{C.9}$$

While eq. (C.7) is still an exact representation of the original Hamiltonian, the electron-photon and electron-phonon interactions have been mixed into a single term where one might say that the photons now interact with a polaron, the electron-phonon quasi-particle, instead of the bare electron. It would be advantageous to more clearly separate the electron-photon and the electron-phonon interaction. To achieve this separation [52, 53] we replace $X_\pm$ with $X_\pm + \langle X\rangle - \langle X\rangle$ in eq. (C.7) to obtain

$$\bar{H} = \bar{H}_{\mathrm{s}'} + \bar{H}_{\mathrm{s}'-\mathrm{ph}'} + H_{0,\mathrm{ph}}, \tag{C.10}$$

with

$$\begin{aligned}
\bar{H}_{\mathrm{s}'} &= \hbar\Delta\sigma_{11} + \hbar g\,\langle X\rangle\,(\sigma_{12} + \sigma_{21}), && \text{(C.11a)}\\
\bar{H}_{\mathrm{s}'-\mathrm{ph}'} &= \hbar g(\sigma_{12}\delta X_+ + \sigma_{21}\delta X_-), && \text{(C.11b)}\\
H_{0,\mathrm{ph}} &= \sum_{\boldsymbol{k}} \hbar\omega_{\boldsymbol{k}} b_{\boldsymbol{k}}^\dagger b_{\boldsymbol{k}}. && \text{(C.11c)}
\end{aligned}$$

where $\langle X\rangle$ is defined in eq. (E.14) and $\delta X_\pm$ in eq. (E.16). Now $\bar{H}_{\mathrm{s}'}$ contains what might be referred to as a system Hamiltonian, however, it is not the original system consisting of only the electron and photon, as the phonon quantity $\langle X\rangle$ has entered. It is, however, of great advantage to include this term in the new system Hamiltonian, since then photon processes are treated to all order as well as preserving the detailed balance condition [58]. This would not be case if the system Hamiltonian were defined as the first term in eq. (C.7), thereby ending up treating the photons only to second order [69, 56]. The quantity $\langle X\rangle$ has the effect of renormalizing the light-matter coupling strength g. From its definition, eq. (E.14), it is clear that $0 < \langle X\rangle \leq 1$, and hence the presence of the phonons will always decrease the effective light-matter coupling. The Hamiltonian $\bar{H}_{\mathrm{s}'-\mathrm{r}'}$ contains the interaction between the system and reservoir, which has been made weaker by the introduction of the difference operators $\delta X_\pm$, making it more suitable for a treatment using perturbation theory.

Appendix D

Lindblad decay rates under the polaron transformation

In this appendix we will calculate the effect of the polaron transformation on a typical Lindblad decay rate. We consider the radiative contribution to the background QD decay rate, which has complicated non-radiative contributions as well, which can not be treated in a simple manner. Our starting point is the Hamiltonian

$$\begin{aligned} H = \hbar\omega_{\mathrm{eg}}\sigma_{\mathrm{ee}} + \sum_l \hbar\Omega_l a_l^\dagger a_l + \sum_{\boldsymbol{k}} \hbar\omega_{\boldsymbol{k}} b_{\boldsymbol{k}}^\dagger b_{\boldsymbol{k}} \\ + \sigma_{\mathrm{ee}} \sum_{\boldsymbol{k}} M^{\boldsymbol{k}}(b_{-\boldsymbol{k}}^\dagger + b_{\boldsymbol{k}}) + \sum_l \hbar g_l (a_l^\dagger \sigma_{\mathrm{ge}} + a_l \sigma_{\mathrm{eg}}), \end{aligned} \tag{D.1}$$

describing a two-level QD with ground and excited states, $\{|g\rangle, |e\rangle\}$, coupled to a phonon bath given by the b_{k} operators and a photon bath given by the a_l operators. Applying the polaron transformation as described in appendix C, we obtain

$$H' = \hbar\omega'_{\mathrm{eg}}\sigma_{\mathrm{ee}} + \sum_l \hbar\Omega_l a_l^\dagger a_l + \sum_{\boldsymbol{k}} \hbar\omega_{\boldsymbol{k}} b_{\boldsymbol{k}}^\dagger b_{\boldsymbol{k}} + \sum_l \hbar g_l (a_l^\dagger X_+ \sigma_{\mathrm{ge}} + a_l X_- \sigma_{\mathrm{eg}}) \tag{D.2}$$

where ω'_{eg} includes the polaron shift and $X_\pm$ is defined in eq. (C.9). We now divide the transformed Hamiltonian as follows

$$H' = H'_0 + H'_{\mathrm{I}}, \tag{D.3}$$

where the free part is

$$H'_0 = \hbar\omega'_{\mathrm{eg}}\sigma_{\mathrm{ee}} + \sum_l \hbar\Omega_l a_l^\dagger a_l + \sum_{\boldsymbol{k}} \hbar\omega_{\boldsymbol{k}} b_{\boldsymbol{k}}^\dagger b_{\boldsymbol{k}}, \tag{D.4}$$

and the interaction part is

$$H_{\mathrm{I}}' = \sum_l \hbar g_l (a_l^\dagger X_+ \sigma_{\mathrm{ge}} + a_l X_- \sigma_{\mathrm{eg}}) \tag{D.5}$$

$$= B\sigma_{\mathrm{ge}} + B^\dagger \sigma_{\mathrm{eg}}, \tag{D.6}$$

where we have defined the combined photon-phonon operator B as

$$B = \sum_l \hbar g_l a_l^\dagger X_+ = AX_+. \tag{D.7}$$

In the original frame the initial condition is assumed to be a fully factorized state

$$\chi(0) = \rho_{\mathrm{QD}}(0) \otimes R_{\mathrm{phonon}} \otimes R_{\mathrm{photon}}, \tag{D.8}$$

where $\chi(t)$ is the density matrix of the total system. Performing the polaron transformation on the initial density matrix entangles the QD and phonon operators, so that the initial state no longer remains fully factorized. This complicates the further application of the Reduced Density Matrix formalism and is often neglected under the assumption that it is small [54]. Employing this approximation we proceed with the following density matrix in the polaron frame

$$\chi'(0) \approx \rho_{\mathrm{QD}}(0) \otimes R_{\mathrm{phonon}} \otimes R_{\mathrm{photon}}. \tag{D.9}$$

We now follow the standard procedure and can write down the EOM for the excited state population of the QD using eq. (2.40)

$$\partial_t n(t) = -\hbar^{-2} \int_0^t dt' \left[e^{i\omega_{\mathrm{eg}}'(t-t')} \langle \tilde{B}(t-t')B^\dagger \rangle + \text{c.c.} \right] n(t). \tag{D.10}$$

From the assumption of a factorized density matrix we obtain

$$e^{i\omega_{\mathrm{eg}}(t-t')} \langle \tilde{B}(t-t')B^\dagger \rangle = \langle \tilde{X}_+(t-t')X_- \rangle \, G(t-t'), \tag{D.11}$$

where the polaron correlation function $\langle \tilde{X}_+(t-t')X_- \rangle$ is given in eq. (E.24) and the photon correlation function is

$$G(t-t') = \sum_l [\hbar g_l]^2 e^{-i(\Omega_l - \omega_{\mathrm{eg}}')(t-t')}. \tag{D.12}$$

If g_l is approximately constant near $\Omega_l = \omega_{\mathrm{eg}}'$ then

$$G(t-t') = \hbar^2 \Gamma \delta(t-t'), \tag{D.13}$$

where Γ is the photon-induced decay rate of the QD, while we neglect the photon Lamb shift. The equation for the QD decay now becomes

$$\partial_t n(t) = -\Gamma \int_0^t dt' \left[\delta(t-t') \langle \tilde{X}_+(t-t')X_- \rangle + \text{c.c.} \right] n(t), \tag{D.14}$$

where, due to the appearance of the delta function in the integrand we may use for the phonon correlation function

$$\langle \tilde{X}_+(t-t')X_-\rangle\,|_{t=t'} = \langle \tilde{X}_+(0)X_-\rangle = 1. \tag{D.15}$$

Therefore, within the stated approximations the polaron transformation does not influence Lindblad decay rates.

Appendix E

Properties of the phonon operators

In this appendix we give various results relating to the phonon operator arising from the polaron transformation

$$X_{\pm} = e^{\pm C}, \quad C = \sum_{\boldsymbol{k}} \lambda_{\boldsymbol{k}} (b^{\dagger}_{-\boldsymbol{k}} - b_{\boldsymbol{k}}), \quad \lambda_{\boldsymbol{k}} = \frac{M^{\boldsymbol{k}}}{\hbar\omega_{\boldsymbol{k}}}. \tag{E.1}$$

The operators $X_{\pm}$ may be written in terms of so-called displacement operators [32]

$$D_{\boldsymbol{k}}(\alpha) = \exp\left(\alpha b^{\dagger}_{\boldsymbol{k}} - \alpha^* b_{\boldsymbol{k}}\right). \tag{E.2}$$

If we rewrite the operator C in the following way

$$C = \sum_{\boldsymbol{k}} \lambda_{\boldsymbol{k}} (b^{\dagger}_{-\boldsymbol{k}} - b_{\boldsymbol{k}}) = \sum_{\boldsymbol{k}} (\lambda_{-\boldsymbol{k}} b^{\dagger}_{\boldsymbol{k}} - \lambda^{*}_{-\boldsymbol{k}} b_{\boldsymbol{k}}), \tag{E.3}$$

we can write

$$X_{\pm} = \prod_{\boldsymbol{k}} \exp\left[\pm(\lambda_{-\boldsymbol{k}} b^{\dagger}_{\boldsymbol{k}} - \lambda^{*}_{-\boldsymbol{k}} b_{\boldsymbol{k}})\right] = \prod_{\boldsymbol{k}} D_{\boldsymbol{k}}(\pm\lambda_{-\boldsymbol{k}}). \tag{E.4}$$

We will need the following useful properties [32, 108] of the displacement operators

$$D^{\dagger}_{\boldsymbol{k}}(\alpha) = D^{-1}_{\boldsymbol{k}}(\alpha) = D_{\boldsymbol{k}}(-\alpha), \tag{E.5}$$

$$D_{\boldsymbol{k}}(\alpha) D_{\boldsymbol{k}}(\beta) = D_{\boldsymbol{k}}(\alpha + \beta) \exp\left(i \mathrm{Im}\left[\alpha\beta^*\right]\right), \tag{E.6}$$

$$\langle D_{\boldsymbol{k}}(\alpha)\rangle = \exp\left(-|\alpha|^2 \left[n_{\boldsymbol{k}} + 1/2\right]\right). \tag{E.7}$$

In the last expression

$$n_{\boldsymbol{k}} = \langle b^{\dagger}_{\boldsymbol{k}} b_{\boldsymbol{k}}\rangle = \frac{1}{\exp\left(\beta\hbar\omega_{\boldsymbol{k}}\right) - 1} \tag{E.8}$$

is the average thermal occupation of phonons in mode $\boldsymbol{k}$ and $\beta = (k_{\mathrm{B}}T)^{-1}$ is the inverse temperature. The brackets $\langle\cdots\rangle = \mathrm{Tr}_{\mathrm{ph}}\{\rho_{\mathrm{ph},0}\cdots\}$ denote the expectation value with respect to the thermal density operator for the phonons

$$\rho_{\mathrm{ph},0} = \frac{\exp(-\beta H_{\mathrm{ph},0})}{\mathrm{Tr}_{\mathrm{ph}}\{\exp(-\beta H_{\mathrm{ph},0})\}}, \tag{E.9}$$

which can be written as a product of the density matrices for the individual $\boldsymbol{k}$ modes as $\rho_{\mathrm{ph},0} = \prod_{\boldsymbol{k}} \rho^{\boldsymbol{k}}_{\mathrm{ph},0}$, where

$$\rho^{\boldsymbol{k}}_{\mathrm{ph},0} = \frac{\exp(-\beta\hbar\omega_{\boldsymbol{k}} b^\dagger_{\boldsymbol{k}} b_{\boldsymbol{k}})}{\mathrm{Tr}_{\mathrm{ph,k}}\left\{\exp(-\beta\hbar\omega_{\boldsymbol{k}} b^\dagger_{\boldsymbol{k}} b_{\boldsymbol{k}})\right\}}, \tag{E.10}$$

is the density matrix for the $\boldsymbol{k}$th phonon mode.

The first property we will show is

$$\langle X_\pm(t)\rangle = \langle X_\pm\rangle = \langle X\rangle\,, \tag{E.11}$$

where the time-evolution is with respect to $H_{\mathrm{ph},0}$, resulting in the standard expression for free evolution

$$b_{\boldsymbol{k}}(t) = e^{-i\omega_{\boldsymbol{k}}t} b_{\boldsymbol{k}}. \tag{E.12}$$

Combining eqs. (E.4) and (E.12) and taking the thermal expectation value using eqs. (E.9) and (E.10) we get [109]

$$\langle X_\pm(t)\rangle = \prod_{\boldsymbol{k}} \langle D_{\boldsymbol{k}}(\pm e^{i\omega_{\boldsymbol{k}}t}\lambda_{-\boldsymbol{k}})\rangle\,, \tag{E.13}$$

where the individual terms in the product may be evaluated using eq. (E.7) yielding

$$\begin{aligned}\langle X_\pm(t)\rangle &= \prod_{\boldsymbol{k}} \exp\left(-|\lambda_{\boldsymbol{k}}|^2\left[n_{\boldsymbol{k}} + 1/2\right]\right)\\ &= \exp\left(-\sum_{\boldsymbol{k}}|\lambda_{\boldsymbol{k}}|^2\left[n_{\boldsymbol{k}} + 1/2\right]\right)\\ &= \langle X\rangle\,,\end{aligned} \tag{E.14}$$

being independent of time.

Next we will evaluate the polaron correlation functions defined as

$$B_+(t,t') = \langle\delta X_\pm(t)\delta X_\pm(t')\rangle\,, \tag{E.15a}$$
$$B_-(t,t') = \langle\delta X_\pm(t)\delta X_\mp(t')\rangle\,, \tag{E.15b}$$

where

$$\delta X_\pm(t) = X_\pm(t) - \langle X\rangle\,. \tag{E.16}$$

Inserting this into the definitions of $B_\pm(t-t')$ we easily find

$$\begin{aligned}\langle \delta X_a(t)\delta X_b(t')\rangle &= \langle (X_a(t)-\langle X\rangle)(X_b(t)-\langle X\rangle)\rangle \\ &= \langle X_a(t)X_b(t')\rangle - \langle X\rangle^2 \,, \end{aligned} \tag{E.17}$$

indicating that we only need to evaluate $\langle X_a(t)X_b(t')\rangle$, where $a, b = \pm$. From the above we get

$$X_a(t)X_b(t') = \prod_{\boldsymbol{k}} D_{\boldsymbol{k}}(ae^{i\omega_{\boldsymbol{k}}t}\lambda_{-\boldsymbol{k}})D_{\boldsymbol{k}}(be^{i\omega_{\boldsymbol{k}}t'}\lambda_{-\boldsymbol{k}}), \tag{E.18}$$

while using eq. (E.6) allows us to write

$$X_a(t)X_b(t') = \prod_{\boldsymbol{k}} D_{\boldsymbol{k}}(\lambda_{-\boldsymbol{k}}[ae^{i\omega_{\boldsymbol{k}}t} + be^{i\omega_{\boldsymbol{k}}t'}]) \tag{E.19}$$

$$\times \exp\left[abi|\lambda_{\boldsymbol{k}}|^2\sin(\omega_{\boldsymbol{k}}(t-t'))\right]. \tag{E.20}$$

Taking the thermal average and employing eq. (E.7) yields

$$\langle X_a(t)X_b(t')\rangle = \exp\left\{-\sum_{\boldsymbol{k}}|\lambda_{\boldsymbol{k}}|^2(2n_{\boldsymbol{k}}+1)\right\}\exp\left\{-ab\varphi(t-t')\right\}, \tag{E.21}$$

where we have defined the function

$$\varphi(t-t') = \sum_{\boldsymbol{k}}|\lambda_{\boldsymbol{k}}|^2\left\{[2n_{\boldsymbol{k}}+1]\cos(\omega_{\boldsymbol{k}}[t-t']) - i\sin(\omega_{\boldsymbol{k}}[t-t'])\right\} \tag{E.22}$$

$$= \sum_{\boldsymbol{k}}|\lambda_{\boldsymbol{k}}|^2\left\{n_{\boldsymbol{k}}e^{i\omega_{\boldsymbol{k}}[t-t']} + [n_{\boldsymbol{k}}+1]e^{-i\omega_{\boldsymbol{k}}[t-t']}\right\} \tag{E.23}$$

Comparing eqs. (E.14), (E.21) and (E.22) we see that

$$\langle X_a(t)X_b(t')\rangle = \langle X\rangle^2 e^{-ab\varphi(t-t')}, \tag{E.24}$$

$$\langle X\rangle = e^{-\varphi(0)/2}. \tag{E.25}$$

Going back to eq. (E.15) and using eq. (E.24) we obtain the final result

$$B_\pm(t,t') = B_\pm(t-t') = \langle X\rangle^2\left(e^{\mp\varphi(t-t')}-1\right), \tag{E.26}$$

where, as expected, the equilibrium phonon correlation functions turn out to depend only on the time-difference and not the absolute time. We will also be needing $B_\pm(t',t)$, i.e., with the time arguments interchanged. These functions are available through complex conjugation

$$\langle \delta X_a(t)\delta X_b(t')\rangle^* = \tag{E.27}$$

$$\left[\mathrm{Tr}_{\mathrm{ph}}\left\{\rho_{\mathrm{ph},0}\delta X_a(t)\delta X_b(t')\right\}\right]^* = \tag{E.28}$$

$$\mathrm{Tr}_{\mathrm{ph}}\left\{\left[\rho_{\mathrm{ph},0}\delta X_a(t)\delta X_b(t')\right]^\dagger\right\} = \tag{E.29}$$

$$\mathrm{Tr}_{\mathrm{ph}}\left\{\delta X_{\bar b}(t')\delta X_{\bar a}(t)\rho_{\mathrm{ph},0}\right\} = \tag{E.30}$$

$$\langle \delta X_{\bar b}(t')\delta X_{\bar a}(t)\rangle, \tag{E.31}$$

where the bar signifies multiplication by -1 and further we used $(X_+)^\dagger = X_-$. In the end we obtain the following relation

$$B_\pm(t', t) = \left[B_\pm(t, t')\right]^* . \tag{E.32}$$

Appendix F

Scattering rates in the polaron frame

In this appendix we explicitly define the scattering rates in the polaron frame entering in eq. (3.52). The building blocks are the integrals $K^{\pm}_{nmkl}(t)$ defined in eq. (3.54). Viz the discussion in section 3.2.6 we take the long-time limit in the integrals, hence we define

$$K^{\pm}_{nmkl} \equiv K^{\pm}_{nmkl}(\infty). \tag{F.1}$$

The rates are

$$\begin{aligned}
\Gamma_1 &= 2\mathrm{Re}\left[K^{-}_{2211} + K^{+}_{2112}\right], && \text{(F.2)}\\
\Gamma_2 &= 2\mathrm{Re}\left[K^{-}_{1122} + K^{+}_{1221}\right], && \text{(F.3)}\\
\gamma_1 &= K^{-}_{1122} + \left[K^{-}_{2211}\right]^* + K^{+}_{1221} + \left[K^{+}_{2112}\right]^*, && \text{(F.4)}\\
\gamma_2 &= \left[K^{-}_{1122}\right]^* + \left[K^{+}_{1221}\right]^*, && \text{(F.5)}\\
\gamma_3 &= \left[K^{-}_{2211}\right]^* + \left[K^{+}_{2112}\right]^*, && \text{(F.6)}\\
iG_1 &= K^{-}_{2122} - \left[K^{-}_{2221}\right]^* + K^{+}_{2221} - \left[K^{+}_{2122}\right]^*, && \text{(F.7)}\\
iG_2 &= K^{-}_{1112} - \left[K^{-}_{2221}\right]^* + K^{+}_{1211} - \left[K^{+}_{2122}\right]^*, && \text{(F.8)}\\
iG_3 &= K^{-}_{1221} + \left[K^{-}_{2112}\right]^* + K^{+}_{1122} + \left[K^{+}_{2211}\right]^*, && \text{(F.9)}\\
iG_4 &= -\left[K^{-}_{2221}\right]^* - \left[K^{+}_{2122}\right]^*, && \text{(F.10)}\\
iG_5 &= -\left[K^{-}_{1112}\right]^* - \left[K^{+}_{1211}\right]^*. && \text{(F.11)}
\end{aligned}$$

Appendix G

Analytical expression for QD decay rates

In this appendix we derive the analytical expressions for the QD decay rates discussed in section 3.3.2. We proceed in two steps; Firstly, an expression is derived that is valid whenever the cavity can be adiabatically eliminated, and secondly, we take the large detuning limit, which simplifies the phonon induced rates to the expression presented in the main text. We only perform the explicit derivation for the QD decay rate in the original frame, eq. (3.58), but the derivation for the same quantity in the polaron frame, eq. (3.59), follows a similar procedure.

From section 3.2.4 we get the EOM for the excited QD population

$$\partial_t \langle \sigma_{11}(t) \rangle = -\Gamma \langle \sigma_{11}(t) \rangle + 2g\mathrm{Im}\left[\langle \sigma_{12}(t) \rangle\right], \tag{G.1}$$

and the photon-assisted polarization

$$\begin{aligned}\partial_t \langle \sigma_{12}(t) \rangle = &- \left[-i\Delta + \tilde{\gamma}_{12}\right] \langle \sigma_{12}(t) \rangle \\ &- i\left[g + \mathcal{G}^{>}\right] \langle \sigma_{11}(t) \rangle + i\left[g + \mathcal{G}^{<}\right] \langle \sigma_{22}(t) \rangle, \end{aligned}\tag{G.2}$$

with $\tilde{\gamma}_{12} = \gamma + \mathrm{Re}[\gamma_{12}] + (\kappa + \Gamma)/2$ and where the long-time limit has been taken in all phonon-induced rates, wherefor we omit the time argument. For the cavity to be adiabatically eliminated it can not perform any back-action on the QD, hence it can not enter in the above EOM for the photon-assisted polarization and we put the cavity population, $\langle \sigma_{22}(t) \rangle$, equal to zero. This is valid in the regime where the cavity decay rate, κ, is much larger than all other parameters. Furthermore, when the total dephasing time $1/|\tilde{\gamma}_{12}|$ is much shorter than the characteristic timescale for $\langle \sigma_{11}(t) \rangle$, we may put $\partial_t \langle \sigma_{12}(t) \rangle = 0$. From this we get

$$\langle \sigma_{12}(t) \rangle = -i\frac{g + \mathcal{G}^{>}}{-i\Delta + \tilde{\gamma}_{12}} \langle \sigma_{11}(t) \rangle, \tag{G.3}$$

which when inserted in eq. (G.1) yields

$$\partial_t \langle \sigma_{11}(t) \rangle = -\Gamma_{\mathrm{tot}} \langle \sigma_{11}(t) \rangle \tag{G.4}$$

where the total QD decay rate is defined as

$$\Gamma_{\text{tot}} = \Gamma + 2g\frac{\tilde{\gamma}_{12}}{\tilde{\gamma}_{12}^2 + \Delta^2}\left[g + \text{Re}[\mathcal{G}^>] - \frac{\Delta}{\tilde{\gamma}_{12}}\text{Im}[\mathcal{G}^>]\right]. \tag{G.5}$$

We are interested in the spontaneous emission rate from the QD due to the coupling to the cavity field, hence we expect the final result to scale with g^2. For this reason we expand the QD-cavity evolution operator $U(t)$ up to first order in g/Δ

$$U(t) \; = \; e^{-i\Delta t}\sigma_{11} + \sigma_{22} + \frac{g}{\Delta}(e^{-i\Delta t} - 1)(\sigma_{12} + \sigma_{21}) + \mathcal{O}((g/\Delta)^2). \tag{G.6}$$

Using this expansion and eq. (3.29) we find

$$\text{Re}[\mathcal{G}^>] \propto \frac{\text{Im}[D^>(\omega = 0) - D^>(\omega = \Delta)]}{\Delta}, \tag{G.7}$$

which is small compared to the remaining terms and will be neglected. From the expansion of the time evolution operator we also find that $\text{Re}[\gamma_{12}]$ scales as g^2, which makes it a higher order effect that can be neglected. We finally arrive at eq. (3.58)

$$\Gamma_{\text{tot}} = \Gamma + 2g^2\frac{\gamma_{\text{tot}}}{\gamma_{\text{tot}}^2 + \Delta^2}\left[1 + \frac{\hbar^{-2}}{\gamma_{\text{tot}}}\text{Re}[D^>(\omega = \Delta)]\right], \tag{G.8}$$

where $\gamma_{\text{tot}} = \gamma + (\kappa + \Gamma)/2$ is the total dephasing rate.

Bibliography

[1] Knill, E., Laflamme, R. & Milburn, G. J. *A scheme for efficient quantum computation with linear optics.* Nature **409**, 46–52 (2001). URL `http://dx.doi.org/10.1038/35051009`.

[2] Winger, M., Volz, T., Tarel, G., Portolan, S., Badolato, A., Hennessy, K., Hu, E., Beveratos, A., Finley, J., Savona, V. & Imamoglu, A. *Explanation of Photon Correlations in the Far-Off-Resonance Optical Emission from a Quantum-Dot - Cavity System.* Phys. Rev. Lett. **103**, 207403 (2009). URL `http://link.aps.org/doi/10.1103/PhysRevLett.103.207403`.

[3] Madsen, K. H., Kaer, P., Kreiner-Mø ller, A., Stobbe, S., Nysteen, A., Mø rk, J. & Lodahl, P. *Measuring the effective phonon density of states of a quantum dot.* arXiv (2012). URL `http://arxiv.org/abs/1205.5623`. `1205.5623`.

[4] Fricke, J. *Transport Equations Including Many-Particle Correlations for an Arbitrary Quantum System: A General Formalism.* Annals of Physics **252**, 479–498 (1996). URL `http://linkinghub.elsevier.com/retrieve/pii/S0003491696901426`.

[5] Haug, H. & Jauho, A.-P. *Quantum Kinetics in Transport and Optics of Semiconductors* (Springer, 2008), second edn.

[6] Goan, H.-S., Jian, C.-C. & Chen, P.-W. *Non-Markovian finite-temperature two-time correlation functions of system operators of a pure-dephasing model.* Phys. Rev. A **82**, 012111 (2010). URL `http://link.aps.org/doi/10.1103/PhysRevA.82.012111`.

[7] Goan, H.-S., Chen, P.-W. & Jian, C.-C. *Non-Markovian finite-temperature two-time correlation functions of system operators: beyond the quantum regression theorem.* J. Chem. Phys. **134**, 124112 (2011). URL `http://iopscience.iop.org/1402-4896/84/6/065010/`.

[8] Carmichael, H. J. *Statistical Methods in Quantum Optics 1 - Master Equations and Fokker-Planck Equations* (Springer, 1999), 1st edn.

[9] Breuer, H.-P. & Petruccione, F. *The Theory of Open Quantum Systems* (Oxford University Press, 2006).

[10] Mahan, G. D. *Many-particle physics* (Plenum Press, 1993), 2nd edn.

[11] Breuer, H.-P., Kappler, B. & Petruccione, F. *Stochastic wave-function method for non-Markovian quantum master equations.* Phys. Rev. A **59**, 1633–1643 (1999). URL `http://pra.aps.org/abstract/PRA/v59/i2/p1633_1`.

[12] Kaer, P., Nielsen, T. R., Lodahl, P., Jauho, A.-P. & Mork, J. *Non-Markovian Model of Photon-Assisted Dephasing by Electron-Phonon Interactions in a Coupled Quantum - Dot - Cavity System.* Phys. Rev. Lett. **104**, 157401 (2010). URL `http://link.aps.org/doi/10.1103/PhysRevLett.104.157401`.

[13] Nazir, A. *Photon statistics from a resonantly driven quantum dot.* Phys. Rev. B **78**, 153309 (2008). URL `http://link.aps.org/doi/10.1103/PhysRevB.78.153309`.

[14] Brandes, T. Quantum Dissipation - UMIST-Bradford Lectures on Background to Quantum Information Theory (2004). URL `http://wwwitp.physik.tu-berlin.de/brandes/public_html/publications/notes.pdf`.

[15] Lindblad, G. *On the generators of quantum dynamical semigroups.* Communications in Mathematical Physics **48**, 119–130 (1976). URL `http://www.springerlink.com/index/10.1007/BF01608499`.

[16] Swain, S. *Master equation derivation of quantum regression theorem.* J. Phys. A: Math. Gen. **14**, 2577 (1981). URL `http://iopscience.iop.org/0305-4470/14/10/013/`.

[17] Meystre, P. & Sargent, M. *Elements of Quantum Optics* (Springer, 2007), 4th edn.

[18] Yamamoto, Y. & Imamoglu, A. *Mesoscopic Quantum Optics* (Wiley, 1999), 1st edn.

[19] Moler, C. & Van Loan, C. *Nineteen Dubious Ways to Compute the Exponential of a Matrix, Twenty-Five Years Later.* SIAM Review **45**, 3 (2003). URL `http://link.aip.org/link/SIREAD/v45/i1/p3/s1&Agg=doi`.

[20] Alonso, D. & de Vega, I. *Multiple-Time Correlation Functions for Non-Markovian Interaction: Beyond the Quantum Regression Theorem.* Phys. Rev. Lett. **94**, 200403 (2005). URL `http://link.aps.org/doi/10.1103/PhysRevLett.94.200403`.

[21] de Vega, I. & Alonso, D. *Non-Markovian reduced propagator, multiple-time correlation functions, and master equations with general initial conditions in the weak-coupling limit.* Phys. Rev. A **73**, 022102 (2006). URL `http://link.aps.org/doi/10.1103/PhysRevA.73.022102`.

[22] de Vega, I. & Alonso, D. *Emission spectra of atoms with non-Markovian interaction: Fluorescence in a photonic crystal.* Phys. Rev. A **77**, 043836 (2008). URL `http://link.aps.org/doi/10.1103/PhysRevA.77.043836`.

[23] Seifert, W., Carlsson, N., Miller, M., Pistol, M.-E., Samuelson, L. & Wallenberg, L. R. *In-situ growth of quantum dot structures by the Stranski-Krastanow growth mode.* Progress in Crystal Growth and Characterization of Materials **33**, 423–471 (1996). URL `http://linkinghub.elsevier.com/retrieve/pii/S0960897496000903`.

[24] Wojs, A., Hawrylak, P., Fafard, S. & Jacak, L. *Electronic structure and magneto-optics of self-assembled quantum dots.* Phys. Rev. B **54**, 5604–5608 (1996). URL `http://prb.aps.org/abstract/PRB/v54/i8/p5604_1`.

[25] Barnett, S. M. & Radmore, P. M. *Quantum theory of cavity quasi-modes.* Optics Communications **68**, 364–368 (1988). URL `http://www.sciencedirect.com/science/article/B6TVF-46JGWMJ-1KS/2/6dd9c5d85802f655bd5c9e18be0a8e02`.

[26] Vahala, K. J. *Optical microcavities.* Nature **424**, 839–46 (2003). URL `http://www.nature.com/nature/journal/v424/n6950/full/nature01939.html`.

[27] Singh, J. *Electronic and Optoelectronic Properties of Semiconductor Structures* (Cambridge University Press, 2003).

[28] Grosse, F. & Zimmermann, R. *Electron-phonon interaction in embedded semiconductor nanostructures.* Phys. Rev. B **75**, 235320 (2007). URL `http://link.aps.org/abstract/PRB/v75/e235320`.

[29] Grosse, F., Muljarov, E. A. & Zimmermann, R. *Semiconductor Nanostructures*, chap. Phonons in, 165–187 (Springer Berlin Heidelberg, 2008).

[30] Nysteen, A. *Cavity QED - Engineering the Phonon Interactions.* Master thesis, Technical University of Denmark (2011).

[31] Gavartin, E., Braive, R., Sagnes, I., Arcizet, O., Beveratos, A., Kippenberg, T. & Robert-Philip, I. *Optomechanical Coupling in a Two-Dimensional Photonic Crystal Defect Cavity.* Phys. Rev. Lett. **106**, 203902 (2011). URL `http://prl.aps.org/abstract/PRL/v106/i20/e203902`.

[32] Walls, D. & Milburn, G. J. *Quantum Optics* (Springer-Verlag Berlin Heidelberg, 2008), 2nd edn.

[33] Krummheuer, B., Axt, V. M. & Kuhn, T. *Theory of pure dephasing and the resulting absorption line shape in semiconductor quantum dots.* Phys. Rev. B **65**, 195313 (2002). URL `http://prb.aps.org/abstract/PRB/v65/i19/e195313`.

[34] Stroscio, M. A. & Dutta, M. *Phonons in Nanostructures* (Cambridge University Press, Cambridge, 2001).

[35] Kippenberg, T. J. & Vahala, K. J. *Cavity optomechanics: back-action at the mesoscale.* Science (New York, N.Y.) **321**, 1172–6 (2008). URL `http://www.sciencemag.org/content/321/5893/1172`.

[36] Yoshie, T., Scherer, A., Hendrickson, J., Khitrova, G., Gibbs, H. M., Rupper, G., Ell, C., Shchekin, O. B. & Deppe, D. G. *Vacuum Rabi splitting with a single quantum dot in a photonic crystal nanocavity.* Nature **432**, 200–203 (2004). URL `http://dx.doi.org/10.1038/nature03119`.

[37] Reithmaier, J. P., Sek, G., Loffler, A., Hofmann, C., Kuhn, S., Reitzenstein, S., Keldysh, L. V., Kulakovskii, V. D., Reinecke, T. L. & Forchel, A. *Strong coupling in a single quantum dot-semiconductor microcavity system.* Nature **432**, 197–200 (2004). URL `http://www.nature.com/nature/journal/v432/n7014/full/nature02969.html`.

[38] Hennessy, K., Badolato, A., Winger, M., Gerace, D., Atature, M., Gulde, S., Falt, S., Hu, E. L. & Imamoglu, A. *Quantum nature of a strongly coupled single quantum dot-cavity system.* Nature **445**, 896–899 (2007). URL `http://www.nature.com/nature/journal/v445/n7130/full/nature05586.html`.

[39] Naesby, A., Suhr, T., Kristensen, P. T. & Mork, J. *Influence of pure dephasing on emission spectra from single photon sources.* Phys. Rev. A **78**, 45802 (2008). URL `http://link.aps.org/abstract/PRA/v78/e045802`.

[40] Auffèves, A., Gérard, J.-M. & Poizat, J.-P. *Pure emitter dephasing: A resource for advanced solid-state single-photon sources.* Phys. Rev. A **79**, 53838 (2009). URL `http://link.aps.org/abstract/PRA/v79/e053838`.

[41] Yamaguchi, M., Asano, T. & Noda, S. *Photon emission by nanocavity-enhancedquantum anti-Zeno effect in solid-state cavityquantum-electrodynamics.* Opt. Express **16**, 18067–18081 (2008). URL `http://dx.doi.org/10.1364/OE.16.018067`.

[42] Winger, M., Volz, T., Tarel, G., Portolan, S., Badolato, A., Hennessy, K., Hu, E., Beveratos, A., Finley, J., Savona, V. & Imamoglu, A. Mesoscopic cavity-QED: the physics behind off-resonant cavity excitation by a single quantum dot (2009). URL `http://arxiv.org/abs/0907.1881`. `0907.1881`.

[43] Laucht, A., Kaniber, M., Mohtashami, A., Hauke, N., Bichler, M. & Finley, J. J. *Temporal monitoring of nonresonant feeding of semiconductor nanocavity modes by quantum dot multiexciton transitions.* Phys. Rev. B **81**, 241302 (2010). URL `http://link.aps.org/doi/10.1103/PhysRevB.81.241302`.

[44] Chauvin, N., Zinoni, C., Francardi, M., Gerardino, A., Balet, L., Alloing, B., Li, L. H. & Fiore, A. *Controlling the charge environment*

of single quantum dots in a photonic-crystal cavity. Phys. Rev. B **80**, 241306 (2009). URL `http://link.aps.org/doi/10.1103/PhysRevB.80.241306`.

[45] Milde, F., Knorr, A. & Hughes, S. *Role of electron-phonon scattering on the vacuum Rabi splitting of a single-quantum dot and a photonic crystal nanocavity.* Phys. Rev. B **78**, 35330 (2008). URL `http://link.aps.org/abstract/PRB/v78/e035330`.

[46] Tarel, G. & Savona, V. *Linear spectrum of a quantum dot coupled to a nanocavity.* Phys. Rev. B **81**, 075305 (2010). URL `http://link.aps.org/doi/10.1103/PhysRevB.81.075305`.

[47] Kaer, P., Nielsen, T., Lodahl, P., Jauho, A.-P. & Mø rk, J. *Microscopic theory of phonon-induced effects on semiconductor quantum dot decay dynamics in cavity QED.* Physical Review B **86**, 085302 (2012). URL `http://link.aps.org/doi/10.1103/PhysRevB.86.085302`.

[48] Roszak, K., Grodecka, A., Machnikowski, P. & Kuhn, T. *Phonon-induced decoherence for a quantum-dot spin qubit operated by Raman passage.* Phys. Rev. B **71**, 195333 (2005). URL `http://prb.aps.org/abstract/PRB/v71/i19/e195333`.

[49] Krugel, A., Axt, V. M., Kuhn, T., Machnikowski, P. & Vagov, A. *The role of acoustic phonons for Rabi oscillations in semiconductor quantum dots.* Applied Physics B: Lasers and Optics **81**, 897–904 (2005). URL `http://www.springerlink.com/content/l56558g365535003/?MUD=MP`.

[50] Stock, E., Dachner, M.-R., Warming, T., Schliwa, A., Lochmann, A., Hoffmann, A., Toropov, A., Bakarov, A., Derebezov, I., Richter, M., Haisler, V., Knorr, A. & Bimberg, D. *Acoustic and optical phonon scattering in a single In(Ga)As quantum dot.* Phys. Rev. B **83**, 041304 (2011). URL `http://prb.aps.org/abstract/PRB/v83/i4/e041304`.

[51] Nielsen, P. K., Thyrrestrup, H., Mø rk, J. & Tromborg, B. *Numerical investigation of electromagnetically induced transparency in a quantum dot structure.* Optics express **15**, 6396–408 (2007). URL `http://dx.doi.org/10.1364/OE.15.006396`.

[52] Würger, A. *Strong-coupling theory for the spin-phonon model.* Phys. Rev. B **57**, 347–361 (1998). URL `http://prb.aps.org/abstract/PRB/v57/i1/p347_1`.

[53] Wilson-Rae, I. & Imamoglu, A. *Quantum dot cavity-QED in the presence of strong electron-phonon interactions.* Phys. Rev. B **65**, 235311 (2002). URL `http://link.aps.org/doi/10.1103/PhysRevB.65.235311`.

[54] Brandes, T. *Coherent and collective quantum optical effects in mesoscopic systems.* Physics Reports **408**, 315–474 (2005). URL `http://www.sciencedirect.com/science/article/B6TVP-4FCSDMG-2/2/f74e72e3efc0ee8b22029719949f565f`.

[55] Ota, Y., Iwamoto, S., Kumagai, N. & Arakawa, Y. Impact of electron-phonon interactions on quantum-dot cavity quantum electrodynamics (2009). URL `http://arxiv.org/abs/0908.0788`.

[56] Hohenester, U. *Cavity quantum electrodynamics with semiconductor quantum dots: Role of phonon-assisted cavity feeding.* Phys. Rev. B **81**, 155303 (2010). URL `http://link.aps.org/doi/10.1103/PhysRevB.81.155303`.

[57] Roy, C. & Hughes, S. *Phonon-Dressed Mollow Triplet in the Regime of Cavity Quantum Electrodynamics: Excitation-Induced Dephasing and Nonperturbative Cavity Feeding Effects.* Physical Review Letters **106**, 247403 (2011). URL `http://link.aps.org/doi/10.1103/PhysRevLett.106.247403`.

[58] Carmichael, H. J. & Walls, D. F. *Master equation for strongly interacting systems.* Journal of Physics A: Mathematical, Nuclear and General **6**, 1552 (1973). URL `http://iopscience.iop.org/0301-0015/6/10/014`.

[59] Weber, C., Richter, M., Ritter, S. & Knorr, A. *Semiconductor Nanostructures: Theory of the Optical Response of Single and Coupled Semiconductor Quantum Dots*, chap. 9, 189–210. NanoScience and Technology (Springer Berlin Heidelberg, Berlin, Heidelberg, 2008). URL `http://www.springerlink.com/index/10.1007/978-3-540-77899-8`.

[60] Muljarov, E. A. & Zimmermann, R. *Dephasing in Quantum Dots: Quadratic Coupling to Acoustic Phonons.* Phys. Rev. Lett. **93**, 237401 (2004). URL `http://prl.aps.org/abstract/PRL/v93/i23/e237401`.

[61] Grange, T. *Decoherence in quantum dots due to real and virtual transitions: A nonperturbative calculation.* Phys. Rev. B **80**, 245310 (2009). URL `http://link.aps.org/abstract/PRB/v80/e245310`.

[62] Muljarov, E. A. & Zimmermann, R. *Exciton Dephasing in Quantum Dots due to LO-Phonon Coupling: An Exactly Solvable Model.* Phys. Rev. Lett. **98**, 187401 (2007). URL `http://link.aps.org/abstract/PRL/v98/e187401`.

[63] Jacak, L., Krasnyj, J., Jacak, D. & Machnikowski, P. *Anharmonicity-induced polaron relaxation in GaAs/InAs quantum dots.* Phys. Rev. B **65**, 113305 (2002). URL `http://prb.aps.org/abstract/PRB/v65/i11/e113305`.

[64] Zimmermann, R. & Runge, E. Dephasing in quantum dots via electron-phonon interaction. In *Proceedings of the 26th International Conference on the Physics of Semiconductors* (-, 2002). URL `http://www.mpipks-dresden.mpg.de/~runge/frame_dt_bunt_files/reprintsDt.html`.

[65] Laucht, A., Hauke, N., Villas-Bôas, J. M., Hofbauer, F., Böhm, G., Kaniber, M. & Finley, J. J. *Dephasing of Exciton Polaritons in Photoexcited InGaAs Quantum Dots in GaAs Nanocavities.* Phys. Rev. Lett. **103**, 87405 (2009). URL `http://link.aps.org/abstract/PRL/v103/e087405`.

[66] Gonzalez-Tudela, A., del Valle, E., Cancellieri, E., Tejedor, C., Sanvitto, D. & Laussy, F. P. *Effect of pure dephasing on the Jaynes-Cummings nonlinearities.* Optics Express **18**, 7002 (2010). URL `http://dx.doi.org/10.1364/OE.18.007002`.

[67] For a textbook reference to this point see, e.g., pp. 167 and 465 in [9].

[68] Harouni, M. B., Roknizadeh, R. & Naderi, M. H. *Influence of phonons on exciton-photon interaction and photon statistics of a quantum dot.* Phys. Rev. B **79**, 165304 (2009). URL `http://link.aps.org/abstract/PRB/v79/e165304`.

[69] Hohenester, U., Laucht, A., Kaniber, M., Hauke, N., Neumann, A., Mohtashami, A., Seliger, M., Bichler, M. & Finley, J. J. *Phonon-assisted transitions from quantum dot excitons to cavity photons.* Phys. Rev. B **80**, 201311 (2009). URL `http://link.aps.org/abstract/PRB/v80/e201311`.

[70] Madsen, K., Ates, S., Lund-Hansen, T., Löffler, A., Reitzenstein, S., Forchel, A. & Lodahl, P. *Observation of Non-Markovian Dynamics of a Single Quantum Dot in a Micropillar Cavity.* Phys. Rev. Lett. **106**, 233601 (2011). URL `http://link.aps.org/doi/10.1103/PhysRevLett.106.233601`.

[71] Ramsay, A., Godden, T., Boyle, S., Gauger, E., Nazir, A., Lovett, B., Fox, A. & Skolnick, M. *Phonon-Induced Rabi-Frequency Renormalization of Optically Driven Single InGaAs/GaAs Quantum Dots.* Physical Review Letters **105**, 177402 (2010). URL `http://link.aps.org/doi/10.1103/PhysRevLett.105.177402`.

[72] Purcell, E., Torrey, H. & Pound, R. *Resonance Absorption by Nuclear Magnetic Moments in a Solid.* Physical Review **69**, 37–38 (1946). URL `http://prola.aps.org/abstract/PR/v69/i1-2/p37_1`.

[73] Madsen, K., Ates, S., Lund-Hansen, T., Löffler, A., Reitzenstein, S., Forchel, A. & Lodahl, P. *Observation of Non-Markovian Dynamics of a Single Quantum Dot in a Micropillar Cavity.* Physical Review Letters **106**, 233601 (2011). URL `http://link.aps.org/doi/10.1103/PhysRevLett.106.233601`.

[74] Reinhard, A., Volz, T., Winger, M., Badolato, A., Hennessy, K. J., Hu, E. L. & Imamoglu, A. *Strongly correlated photons on a chip.* Nature Photonics **6**, 93–96 (2011). URL `http://www.nature.com/doifinder/10.1038/nphoton.2011.321`.

[75] McCutcheon, D. P. S. & Nazir, A. *Quantum dot Rabi rotations beyond the weak exciton - phonon coupling regime.* New Journal of Physics **12**, 113042 (2010). URL `http://iopscience.iop.org/1367-2630/12/11/113042/`.

[76] Auffèves, A., Gerace, D., Gérard, J.-M., Santos, M., Andreani, L. & Poizat, J.-P. *Controlling the dynamics of a coupled atom-cavity system by pure dephasing.* Phys. Rev. B **81**, 245419 (2010). URL `http://link.aps.org/doi/10.1103/PhysRevB.81.245419`.

[77] Sapienza, L., Thyrrestrup, H., Stobbe, S., Garcia, P.-D., Smolka, S. & Lodahl, P. *Cavity quantum electrodynamics with Anderson-localized modes.* Science **327**, 1352–5 (2010). URL `http://www.sciencemag.org/content/327/5971/1352`.

[78] Hughes, S., Yao, P., Milde, F., Knorr, A., Dalacu, D., Mnaymneh, K., Sazonova, V., Poole, P., Aers, G., Lapointe, J., Cheriton, R. & Williams, R. *Influence of electron-acoustic phonon scattering on off-resonant cavity feeding within a strongly coupled quantum-dot cavity system.* Phys. Rev. B **83**, 165313 (2011). URL `http://link.aps.org/doi/10.1103/PhysRevB.83.165313`.

[79] Borri, P., Langbein, W., Schneider, S., Woggon, U., Sellin, R. L., Ouyang, D. & Bimberg, D. *Ultralong Dephasing Time in InGaAs Quantum Dots.* Phys. Rev. Lett. **87**, 157401 (2001). URL `http://prl.aps.org/abstract/PRL/v87/i15/e157401`.

[80] Besombes, L., Kheng, K., Marsal, L. & Mariette, H. *Acoustic phonon broadening mechanism in single quantum dot emission.* Phys. Rev. B **63**, 155307 (2001). URL `http://prb.aps.org/abstract/PRB/v63/i15/e155307`.

[81] Santori, C., Fattal, D., Vučković, J., Solomon, G. S. & Yamamoto, Y. *Indistinguishable photons from a single-photon device.* Nature **419**, 594–597 (2002). URL `http://www.nature.com/doifinder/10.1038/nature01086`.

[82] Varoutsis, S., Laurent, S., Kramper, P., Lemaître, A., Sagnes, I., Robert-Philip, I. & Abram, I. *Restoration of photon indistinguishability in the emission of a semiconductor quantum dot.* Phys. Rev. B **72**, 041303 (2005). URL `http://link.aps.org/doi/10.1103/PhysRevB.72.041303`.

[83] Bylander, J. & Abram, I. *Interference and correlation of two independent photons.* Eur. Phys. J. D **22**, 295–301 (2003). URL `http://www.springerlink.com/content/5tjybnhnn8rdvmyr/`.

[84] Kiraz, A., Atatüre, M. & Imamoglu, A. *Quantum-dot single-photon sources: Prospects for applications in linear optics quantum-information processing.* Phys. Rev. A **69**, 032305 (2004). URL `http://link.aps.org/doi/10.1103/PhysRevA.69.032305`.

[85] Ben, Y., Hao, Z., Sun, C., Ren, F. & Luo, Y. *Photon-emission properties of quantum-dot-based single-photon sources under different excitations.* App. Phys. B **81**, 39–42 (2005). URL `http://www.springerlink.com/index/10.1007/s00340-005-1869-3`.

[86] Yao-Yi, L., Mu-Tian, C., Hui-Jun, Z., Shao-Ding, L. & Qu-Quan, W. *Second-Order Correlation Function of the Photon Emission from a Single Quantum Dot.* Chin. Phys. Lett. **22**, 2960–2962 (2005). URL `http://iopscience.iop.org/0256-307X/22/11/065/`.

[87] Troiani, F., Perea, J. & Tejedor, C. *Analysis of the photon indistinguishability in incoherently excited quantum dots.* Phys. Rev. B **73**, 035316 (2006). URL `http://link.aps.org/doi/10.1103/PhysRevB.73.035316`.

[88] Sun, F. & Wong, C. *Indistinguishability of independent single photons.* Phys. Rev. A **79**, 013824 (2009). URL `http://link.aps.org/doi/10.1103/PhysRevA.79.013824`.

[89] Cancellieri, E., Troiani, F. & Goldoni, G. *Optimal generation of indistinguishable photons from non-identical artificial molecules.* Opt. Express **17**, 17156 (2009). URL `http://dx.doi.org/10.1364/OE.17.017156`.

[90] Pathak, P. & Hughes, S. *Coherently triggered single photons from a quantum-dot cavity system.* Phys. Rev. B **82**, 045308 (2010). URL `http://link.aps.org/doi/10.1103/PhysRevB.82.045308`.

[91] Santori, C., Fattal, D., Fu, K.-M. C., Barclay, P. E. & Beausoleil, R. G. *On the indistinguishability of Raman photons.* New J. Phys. **11**, 123009 (2009). URL `http://iopscience.iop.org/1367-2630/11/12/123009/`.

[92] Kaer, P., Lodahl, P., Jauho, A. P. & Mork, J. *Microscopic theory of indistinguishable single-photon emission from a quantum dot coupled to a cavity: The role of non-Markovian phonon-induced decoherence.* arXiv 1–6 (2012). URL `http://arxiv.org/abs/1203.6268`. `1203.6268`.

[93] Hong, C. K., Ou, Z. Y. & Mandel, L. *Measurement of subpicosecond time intervals between two photons by interference.* Phys. Rev. Lett. **59**, 2044–2046 (1987). URL `http://link.aps.org/doi/10.1103/PhysRevLett.59.2044`.

[94] Hanbury-Brown, R. & Twiss, R. Q. *A Test of a New Type of Stellar Interferometer on Sirius.* Nature **178**, 1046–1048 (1956). URL `http://www.nature.com/nature/journal/v178/n4541/abs/1781046a0.html`.

[95] Lounis, B. & Orrit, M. *Single-photon sources.* Reports on Progress in Physics **68**, 1129–1179 (2005). URL `http://iopscience.iop.org/0034-4885/68/5/R04/`.

[96] Ballentine, L. E. *Quantum Mechanics - A Modern Development* (World Scientific, 1998).

[97] Hughes, S. & Yao, P. *Theory of quantum light emission from astrongly-coupled single quantum dotphotonic-crystal cavity system.* Opt. Express **17**, 3322–3330 (2009). URL `http://dx.doi.org/10.1364/OE.17.003322`.

[98] Hohenester, U. *Quantum control of polaron states in semiconductor quantum dots.* J. Phys. B **40**, 315–330 (2007). URL `http://iopscience.iop.org/0953-4075/40/11/S06/`.

[99] Guido. Python documentation (2012). URL `http://docs.python.org/library/itertools.html#itertools.combinations_with_replacement`.

[100] Knap, M., Arrigoni, E., von der Linden, W. & Cole, J. *Emission characteristics of laser-driven dissipative coupled-cavity systems.* Phys. Rev. A **83**, 023821 (2011). URL `http://link.aps.org/doi/10.1103/PhysRevA.83.023821`.

[101] Cuthill, E. & McKee, J. Reducing the bandwidth of sparse symmetric matrices. In *Proceedings of the 1969 24th national conference on -*, 157–172 (ACM Press, New York, New York, USA, 1969). URL `http://dl.acm.org/citation.cfm?doid=800195.805928`.

[102] Magnus, W. *On the exponential solution of differential equations for a linear operator.* Communications on Pure and Applied Mathematics **7**, 649–673 (1954). URL `http://doi.wiley.com/10.1002/cpa.3160070404`.

[103] Blanes, S., Casas, F., Oteo, J. & Ros, J. *The Magnus expansion and some of its applications.* Physics Reports **470**, 151–238 (2009). URL `http://linkinghub.elsevier.com/retrieve/pii/S0370157308004092`.

[104] Roy, C. & Hughes, S. *Phonon-Dressed Mollow Triplet in the Regime of Cavity Quantum Electrodynamics: Excitation-Induced Dephasing and Nonperturbative Cavity Feeding Effects.* Phys. Rev. Lett. **106**, 247403 (2011). URL `http://link.aps.org/doi/10.1103/PhysRevLett.106.247403`.

[105] Roy, C. & Hughes, S. *Polaron master equation theory of the quantum-dot Mollow triplet in a semiconductor cavity-QED system.* Phys. Rev. B **85**, 115309 (2012). URL `http://link.aps.org/doi/10.1103/PhysRevB.85.115309`.

[106] Hohenester, U. *Optimal quantum gates for semiconductor qubits.* Phys. Rev. B **74**, 161307 (2006). URL `http://link.aps.org/doi/10.1103/PhysRevB.74.161307`.

[107] Grodecka, A., Weber, C., Machnikowski, P. & Knorr, A. *Interplay and optimization of decoherence mechanisms in the optical control of spin quantum bits implemented on a semiconductor quantum dot.* Phys. Rev. B **76**, 205305 (2007). URL `http://prb.aps.org/abstract/PRB/v76/i20/e205305`.

[108] Glauber, R. J. *Coherent and Incoherent States of the Radiation Field.* Phys. Rev. **131**, 2766–2788 (1963). URL `http://prola.aps.org/abstract/PR/v131/i6/p2766_1`.

[109] As both $X_\pm(t)$ and $\rho_{\mathrm{ph},0}$ factor into individual $\boldsymbol{k}$ contributions, the averaging may be performed for one $\boldsymbol{k}$ at a time and no crossterms in e.g. $\boldsymbol{k}$ and $\boldsymbol{k}'$ occur.